UC San Diego
UC San Diego Electronic Theses and Dissertations

Title
Spin injection and transport in semiconductor and metal nanostructures

Permalink
https://escholarship.org/uc/item/9t24x7n8

Author
Zhu, Lei

Publication Date
2009

Peer reviewed|Thesis/dissertation

eScholarship.org Powered by the California Digital Library
University of California

UNIVERSITY OF CALIFORNIA, SAN DIEGO

Spin injection and transport in semiconductor and metal nanostructures

A dissertation submitted in partial satisfaction of the
requirements for the degree Doctor of Philosophy

in

Physics

by

Lei Zhu

Committee in charge:

Professor Edward T. Yu, Chair
Professor Lu J. Sham, Co-Chair
Professor Dimitri N. Basov
Professor Eric. E. Fullerton
Professor Sunil K. Sinha

2009

Copyright

Lei Zhu, 2009

All rights reserved.

The dissertation of Lei Zhu is approved, and it is acceptable in quality and form for publication on microfilm and electronically:

____

____

____

____
Chair

____
Co-Chair

University of California, San Diego

2009

To my family

TABLE OF CONTENTS

Signature Page ... iii

Dedication ... iv

Table of Contents ... v

List of Figures ... ix

List of Tables ... xiv

Acknowledgements ... xv

Vita ... xvii

Abstract ... xviii

Chapter 1 Introduction ... 1

1.1 Introduction to spintronics: fundamentals and applications ... 1

1.2 Outline of work presented in this dissertation ... 9

Reference ... 12

Chapter 2 Spin transport in semiconductors and metals: a diffusive picture vs. a ballistic picture ... 15

2.1 Spin-dependent drift-diffusion equations: derivation and application ... 16

2.2 Spin-dependent ballistic model ... 21

2.3 Spin transport in metallic hybrid devices ... 30

2.4 Lateral spin valve based on ferromagnet/semiconductor hybrid system…………32

2.5 Multi-terminal spintronic devices and spintronic circuits………………………...34

2.6 Conclusions…………………………………………………………………....35

Reference………………………………………………………………………..37

Chapter 3 Electrical transport and spin diffusion in InAs: a study by weak localization and antilocalization measurement……………………….…………………………40

3.1 InAs-based devices for spintronic application…………………………………...41

3.2 Influence of surface passivation on electrical properties of InAs surface electron layers……………………………………………………………..…..…....42

3.3 Weak localization and antilocalization measurements on InAs surface inversion layers……………..………………………………………………..……………5

3.4 Conclusions……………………………………………………………………….54

Reference…………………………………………………………………..…56

Chapter 4 Electrical spin injection and detection in InAs surface electron layers……58

4.1 Spin valve and spin transistor based on ferromagnet/semiconductor hybrid structures……………..…………………………………………………………….61

4.2 Characterization of spin injection barrier into InAs………………….. ………....61

4.2.1 Preparation of InAs surface for spin injection……………………………….....61

4.2.2 Conductive atomic force microscopy of tunnel barriers on treated InAs surfaces……………………………………………………………………………..62

4.3 Micromagnetic behavior of magnetic contacts for spin injection into semiconductor…………………………………………………………………...66

4.4 Magnetoresistance measurements in the local spin-valve geometry…………….....68

4.5 Conclusions……………………………………………………………………....72

Reference……………………………………………………………………….….74

Chapter 5 Ballistic transport and electrical spin signal amplification in a three-terminal spintronic device……………………………………………………….……….75

5.1 Amplification of a spin-polarized current…………………………………………76

5.2 Multi-terminal spin transistor based on InAs…………………………………..…...79

5.3 Magnetic configuration of multi-stripe nanomagnet structure………………..….83

5.4 Magnetoresistance amplification in multi-terminal spin transistor……………...86

5.4.1 Measurement scheme of magnetoresistance in a spin transistor………………..86

5.4.2 Magnetoreistance amplification mechanism: a spin-diffusion analysis……….89

5.4.3 Magnetoreistance amplification mechanism: a spin-polarized ballistic analysis…………………………………………………………………….…………92

5.4.4 Comparison of the spin diffusive analysis and the spin-polarized ballistic analysis…………………..……………………………………………………….….98

5.5 Conclusions…………………………………………………………………....103

Reference………………………………………………………………………….105

Chapter 6 Geometry influence on spin diffusion and reexamination of spin injection model in a metallic spin valve…………………….…………………………………...107

6.1 Spin injection and diffusion in mesoscopic spintronic devices…………………107

6.2 Numerical simulation of spin injection and diffusion in mesoscopic spintronic devices by finite element method……………………………………..……….109

6.2.1 Numerical simulation of spin injection and diffusion in a metallic spin valve by finite element method…………………………………………………………110

6.2.2 Comparison of numerical simulation results of spin splitting in a thin-channel spin valve and cross section images of spin polarization in an n-GaAs spin valve………………………………………………………………………………116

6.2.3 Reexamination of one dimensional spin valve model……………………….118

6.3 Semi-analytical method for evaluation of spin diffusion in mesoscopic spintronic devices…………………..……………………………………………..………..119

6.4 Experimental examination of spin injection and diffusion in metallic mesoscopic spin valves………………………………………………………….……..121

6.5 Conclusions……………………………………..…………………......124

Reference……………………………………………………………………126

LIST OF FIGURES

Figure 3.1: (a) Schematic of InAs surface before sulfuration treatments. The amorphous surface layer consists of native In-O_x and As-O_x components. (b) schematic of $(NH_4)_2S_x$ passivated InAs surface. This idealized structural model only involves In-S bonding……………………………………………………………44

Figure 3.2: Schematic diagram of Corbino disk device structure, measurement configuration, and InAs electronic structure.. ……….. . …………………………....46

Figure 3.3: Magnetoconductance measured in Corbino disk structure. The classic Drude parabolas appear in the magnetoconductance characteristics at high magnetic fields and the quantum corrections become dominant at low magnetic fields………47

Figure 3.4: Magnetoconductance measured in Corbino disk device structure, along with fitted curves from which elastic, inelastic, and spin-orbit scattering lengths are determined. (a) Corbino disk device with native oxide on InAs surface, and (b) Corbino disk device with sulfur-passivated InAs surface.. . . . . . . ………. …. ……..48

Figure 3.5: Magnetoconductance measured in Corbino disk device structure, along with fitted curves from ILP theory, for (a) Corbino disk device with native oxide on InAs surface, and (b) Corbino disk device with sulfur-passivated InAs surface……53

Figure 4.1: (a) Schematic of a spin valve, with two contacts magnetized perpendicular to the transport direction of the spin-polarized electrons. (b) Schematic of a spin transistor, with a gate contact and two ferromagnet contacts parallel to the transport direction of the spin-polarized electrons… . . .. ………..………… . ..60

Figure 4.2: Topographic and conductive atomic force microscope images, obtained simultaneously in each case with 1V bias applied to the sample, of (a) p-type InAs with native oxide layer, and (b) p-type InAs on which a 3nm Al_2O_3 layer has been deposited by sputtering. All scale bars are 200nm. Grey scales correspond to 5nm for topography, 1nA for current……………………………………………………………65

Figure 4.3: (a) Schematic diagram of measurement process for atomic and magnetic force microscopy of Co ferromagnetic contacts for spin-valve device. (b) Topographic image of Co contacts, and (c)-(e) magnetic force images of Co contacts after application of external magnetic fields of 300Oe, 600Oe, and 1200Oe, respectively. The magnetic force images show the transition from parallel magnetization, in (c), to antiparallel magnetization, in (d), and back to parallel magnetization, in (e), in the opposite direction to that in (c). All scale bars are 500nm. Grey scale corresponds to 300nm in topographic image…..……………………. 67

Figure 4.4: Schematic diagram of spin-valve device structure as fabricated on p-type InAs, magnetoresistance measurement configuration, and InAs electronic structure………………………………………………………………. . …. . ….. . 69

Figure 4.5: Magnetoresistance measured for spin-valve device structure shown in Figure 4.4, for field sweep directions from – to + (open circles) and + to – (solid squares)……………………………………………………………………………...70

Figure 4.6: Maximum measured magnetoresistance as a function of spin-valve channel length (filled squares), along with line fitted according to Eqn. (4.2) from which the spin injection efficiency and spin diffusion length are determined………………......72

Figure 5.1: (a) spin amplifier with $g_s^{(1)} < 1$ and $g_s^{(2)} > 1$. (b) spin amplifier with $g_s^{(1)} > 1$ and $g_s^{(2)} < 1$. (c) spin amplifier with $g_s^{(1)} > 1$ and $g_s^{(2)} > 1$. (d) a conceptual spin amplifier with three components.. . . . . ………………………………..….. .. ….. . 78

Figure 5.2: (a) Schematic diagram of three-terminal device geometry and measurement configuration. (b) SEM image of device with Co contacts and Au leads on p-InAs; magnified view shows geometry and dimensions of the three Co contacts. Scale bars are 2µm (left) and 500nm (right).. . . . . ………………………………….82

Figure 5.3: (a) Schematic diagram of MFM measurement process: an external magnetic field is applied to control the magnetization of the Co contacts, and subsequently MFM measurements are performed to assess directly the contact magnetization as a function of external field. (b) AFM topographic and (c)-(f) MFM images of the Co contacts following application of successively larger external fields, showing the transition from an all-parallel magnetization configuration (c)-(d) to an antiparallel configuration (e) and back to an all-parallel configuration (f). All scale bars are 1µ…………………………………………………………………….85

Figure 5.4: (a) Plot of current I_L as a function of voltages V_R and V_L, with $V_C = 0$. A locus of points in the (V_R,V_L)-plane corresponding to I_L=0 is clearly evident. (b) Shift in I_L due to alterations in spin injection and transport upon application of an external magnetic field that changes the magnetization configuration of the Co contacts. For operation near a point at which $I_L(\downarrow\uparrow\uparrow)$=0, a large on/off current switching ratio can be attained...……………………..…………………87

Figure 5.5: Current flow I_L as a function of external applied magnetic field, for field sweep directions – to + (red diamonds) and + to – (black squares). A clear shift in current for antiparallel magnetization configurations (↓↑↑ at ~+1500Oe and ↑↓↓ at ~-2000Oe) is evident. Adjustment of voltages V_L and V_R allows the current in the antiparallel configuration to approach zero (to within the noise floor of the device), leading to a large on/off current switching ratio……………………..…………..99

Figure 5.6: Abrupt current dip increased slowly with initial current without external magnetic field applied; correspondingly, MR will decrease dramatically………......101

Figure 6.1: Chemical potential splitting ($\mu_+ - \mu_-$) in local spin valve geometry (a) in the antiparallel magnetization configuration (b) in the parallel magnetization configuration………………..…………………………………………………...113

Figure 6.2: Chemical potential splitting ($\mu_+ - \mu_-$) in the parallel magnetization configuration (a) in a 500-nm-thick channel spin valve, and (b) in a 65-nm-thick channel spin valve…………………………………………….………………114

Figure 6.3: Chemical potential splitting ($\mu_+ - \mu_-$) in the antiparallel magnetization configuration (a) in a 500-nm-thick channel spin valve, and (b) in a 65-nm-thick channel spin valve……….……………….…………………………….....................115

Figure 6.4: (a) Kerr microscope image of spin polarization in n-GaAs channel (after P. Kotissek, et al, *Nat. Phys.* **3**, 872 (2007).). (b) Simulation results of chemical potential splitting ($\mu_+ - \mu_-$) in a shallow-channel metallic spin valve……...........................…117

Figure 6.5: Fitted spin injection efficiency as a function of Ag channel thickness, based on one dimensional spin diffusion model…………………………….……119

Figure 6.6: Magnetoresistance as a function of channel thickness in a lateral spin valve. The square dots and the solid curve represent the estimate from the 2D numerical simulation and the calculation by the multi-layer semi-analytical model, respectively…………………………………………………………..………...120
Figure 6.7: Scanning electron microscope (SEM) image of a spin valve composed of two Py contacts and Al channel……………………….……………………….….123

LIST OF TABLES

Table 4.1: Details of surface treatments implemented on InAs……………………62

Table 6.1: Boundary conditions for the numerical simulations presented in Figure 6.1…………………………………………………………………………….....111

Table 6.2: Estimated spin injection efficiency in Py/Al/Py spin valves with different channel thickness……………………………..………………………………124

ACKNOWLEDGEMENTS

First and foremost I would like to thank my advisor Professor Edward Yu. I am incredibly fortunate to be able to work closely with him. His support and encouragement has made the completion of my research possible. His guidance has and will benefit me throughout my graduate study and my whole life.

I would like to thank all my collaborators for their numerous help to my work and this dissertation. It has been a valuable experience and great pleasure working with them. I appreciate all the help from the former and current members of the ETY group, and all my friends for their kindness, wisdom, and inspiration, including Hongtao, Xiaotian, Daniel, Mo, Sourobh, Bin, Shadi, Swee Hoe, Daniel, Jeremy, Peter, Clay, Keun Woo, Zhiqiang, Hao, Haijiang, Kai, Steve, Yaoming, Ting, Seng, Liang, and Sifang.

I am indebted to many people for their inspiration. Professor Sham not only has been an inexhaustible source of ideas on spintronics, but also left me ten pounds quantum mechanics notes from his three quarter's in-depth lectures. Professor Fullerton opens me the door to the magnetism and its cutting-edge application. All the comments from Professor Sinha, Professor Basov and Prof. Wang turn out to be deep and fruitful.

Finally, I would like to thank my parents, my sisters and my girlfriend. The support of my loving family takes me all the way to here.

Chapter 3 and Chapter 4 contains materials in L. Zhu and E. T. Yu, "*Influence of surface treatment and interface layers on electrical spin injection efficiency and transport in InAs*", which is submitted to Journal of Applied Physics and posted online. Chapter 5 contains materials in L. Zhu and E. T. Yu, "*Ballistic transport and electrical spin signal amplification in a three-terminal spintronic device*", which is ready for submission to Nature Physics. Chapter 6 contains materials in L. Zhu and E. T. Yu, "*Geometry influence on spin diffusion and reexamination of spin injection model in a metallic spin valve*", which is ready for submission to Applied Physics Letters. The dissertation author was the primary investigator and author of all these papers.

VITA

2002	B.S. Physics, Peking University, P.R. China
2002-2003	Teaching assistant, University of California, San Diego
2003-2009	Graduate student researcher, University of California, San Diego
2004	M.S. Physics, University of California, San Diego
2009	Ph.D. Physics, University of California, San Diego

ABSTRACT OF THE DISSERTATION

Spin injection and transport in semiconductor and metal nanostructures

by

Lei Zhu

Doctor of Philosophy in Physics
University of California, San Diego, 2009
Professor Edward T. Yu, Chair
Professor Lu J. Sham, Co-Chair

In this thesis we investigate spin injection and transport in semiconductor and metal nanostructures. To overcome the limitation imposed by the low efficiency of spin injection and extraction and strict requirements for retention of spin polarization within the semiconductor, novel device structures with additional logic functionality and optimized device performance have been developed. Weak localization/antilocalization measurements and analysis are used to assess the influence of surface treatments on elastic, inelastic and spin-orbit scatterings during the electron transport within the two-dimensional electron layer at the InAs surface. Furthermore, we have used spin-valve and scanned probe microscopy measurements to investigate the influence of sulfur-based surface treatments and electrically insulating barrier layers on spin injection into, and spin transport within, the two-

dimensional electron layer at the surface of p-type InAs. We also demonstrate and analyze a three-terminal, all-electrical spintronic switching device, combining charge current cancellation by appropriate device biasing and ballistic electron transport. The device yields a robust, electrically amplified spin-dependent current signal despite modest efficiency in electrical injection of spin-polarized electrons. Detailed analyses provide insight into the advantages of ballistic, as opposed to diffusive, transport in device operation, as well as scalability to smaller dimensions, and allow us to eliminate the possibility of phenomena unrelated to spin transport contributing to the observed device functionality. The influence of the device geometry on magnetoresistance of nanoscale spin-valve structures is also demonstrated and discussed. Shortcomings of the simplified one-dimensional spin diffusion model for spin valve are elucidated, with comparison of the thickness and the spin diffusion length in the nonmagnetic channel as the criterion for validity of the 1D model. Our work contributes directly to the realization of spin valve and spin transistor devices based on III-V semiconductors, and offers new opportunities to engineer the behavior of spintronic devices at the nanoscale.

Chapter 1

Introduction

1.1 Introduction to Spintronics: fundamentals and applications

Semiconductor devices for information processing, storage, and transmission are among the most sophisticated, rapidly evolving structures.[1] In the last three decades, Moore's law has successfully predicted the persistent miniaturization of semiconductor devices, such as the unit cell in magnetic storage disks and the transistor in microprocessors and random access memories.[2] Despite the series of successful stories in this area, the fundamental challenges will abound in the near future. The dimension of semiconductor devices, with exponentially scaling-down trends will be knocking on the quantum physics' door. Alternate methods, either associating the conventional semiconductor devices with novel functionalities, or replacing the current information technologies with entirely distinct logical designs, have been proposed in a number of ambitious interdisciplinary programs, involving engineers, physicists, and even economists.

Among these proposals, spintronics, i.e., electronics focused on understanding spin and its related phenomena, and harness them into novel functionalities in realistic usages, mainly in solid-state circuits. The significant impact of spintronics on electronics has lasted for decades. The different types of magnetic order have inspired theoretical physicists to develop many-body theory. And emerging magnetism effects, such as anisotropic magnetoresistance (AMR) trigger experimental physicists to explore profound thin-film magnetism. However, spintronics wasn't made a technological reality until the discovery of giant magnetoresistance (GMR) in 1988. In the initial experiments based on MBE-grown epitaxial Fe/Cr multilayers, done by Fert's group[3] and Grünberg's group[4], the conditions like epitaxial growth, low temperature and high magnetic fields are required to achieve GMR effects, and thus, prevent the integration of GMR devices into commercialized computer technology. But fortunately, the spin valve structures based on sputtered polycrystalline multilayer thin film show large GMR in very small fields,[5] which exhibits great technological significance. The GMR effect can be explained by the so-called two-current model, and furthermore by a quantum-mechanical picture.[6] The two-current model originating from Mott,[7] developed by Fert and Campbell,[8] is based on a picture of separated spin up and spin down channels coupled with spin mixing by electron-magnon collisions. As the most successful commercialization of spintronics, read heads utilizing GMR effect have been widely used in hard drives in computers and custom electronics products such as iPods.

The magnetic random access memory (MRAM) device is another practical spintronic device. The initial MRAM devices, produced by Honeywell in 1997 are based on GMR effects. Currently MRAM devices switch to tunneling magnetoresistance (TMR) based structures,[9] as produced by Freescale Semiconductor and IBM. TMR device, consisting of ferromagnet/tunneling-barrier/ferromagnet sandwich structure, provides a universal memory structure with non-volatility and scalability. The spin-momentum-transfer effect (SMT), which was theoretically predicted in 1996[10] and experimentally achieved in 2000,[11] illustrates a new direction for MRAM. Conventional MRAM utilize magnetic fields generated by the word lines and bit lines to flip the relative magnetization direction between two magnetic layers. The switch fields required become extremely large as the size of the unit MRAM cell shrinks. Therefore, for a unit cell less than 100 nm, the program energy for a MRAM cell is as high as 120 pJ,[2] more than 20 times of program energy for a dynamical random access memory (DRAM). SMT utilizes the momentum transfer from a spin-polarized current to a magnetic free layer, and offers a different switching methodology to magnetize a unit cell. This SMT effect becomes prominent when the cell size is less than 100 nm. With additional layers involved for employing SMT effect, the new design eventually circumvents the complicated and energy-consuming circuit for generating program current in MRAM, which lowers the program energy from 120 pJ to 0.02 pJ, and program time from 5-20 ns to 1 ns,[2] as theoretically estimated. Spin momentum transfer can also be used to control the generation or movement of domain walls, and thus, provide another possibility for data storage aside

from the conventional scheme in hard drives.[12] Furthermore, SMT effect inspired logic devices based on ferromagnetic loops.[13] The spin wave generated by SMT can radiate rf or microwave signals with the frequency range from a few to tens of GHz, and potentially hundreds of GHz bandwidth.[14] Therefore, a nanoscale electromagnetic oscillator based on SMT shows great potential for applications, such as high-speed chip-to-chip communication, local wideband radio.

Except for the application in data storage, another ambitious goal in spintronics is to develop spin-based logic devices to replace charge-based logic devices, in which the amount of charges encodes '0' and '1'. A spin transistor is an obvious counterpart of a conventional transistor as the basic unit for spintronic circuit. It is noted that 'spin-charge hybrid devices' and 'spin monolithic devices' are distinguished by the role of carrier spins in active spin devices.[15] The modulation of spin status in a spin-charge hybrid device is still delegated by charge with influence from spin polarization. The first spin field effect transistor (SpinFET), inspired by an optoelectronic modulator, is proposed by Datta and Das,[16] which is composed of two ferromagnetic terminals separated by non-magnetic material. It has a similar geometry with a conventional metal-insulator- semiconductor field effect transistor (MISFET) with ferromagnetic terminals instead. The spin polarized current in non-magnetic channel preserves its direction at the injection interface and can be modulated by the gate voltage via spin precession. The electric conductivity depends on the relative direction of the magnetization of the drain contact and the polarization direction of current before reaching the drain contact. Therefore, a transistor action is achieved. It stands

for reason that there are several important prerequisites to realize a SpinFET, such as high efficient spin injection at the source end and spin filtering at the drain end, gate manipulation on spin precession, and long spin relaxation length in the non-magnetic channel.

Compared with optical spins injection,[17] electrical spin injection from ferromagnet into paramagnet or non-magnetic semiconductors is a more versatile and flexible method to generate spin accumulation in non-magnetic channels. The early exploration on spin injection through ferromagnet/paramagnet interface and spin accumulation in paramagnet was made by Johnson and Silsbee in 1985.[18, 19, 20] Spin injection into semiconductors had attracted great attention, but achieved limited success in solid state systems before late nineties. The lateral spin-valve device fabricated on III-V semiconductor quantum well reveals possible spin polarization inside semiconductor channels, as shown by Hammar et al.,[21] but this type of device also exhibits inconsistency in most cases, as shown by Monzon and Roukes.[22] The inefficient spin injection into a semiconductor was explained in 2000 by Schmidt et al,[23] referred to as the conductivity mismatch problem at the ferromagnet/semiconductor interface. Following studies provide sufficient understanding on this problem, from a diffusive transport picture[24] or a ballistic transport picture.[25] Either a spin-selective resistive contact in between ferromagnet and semiconductor or a magnetic semiconductor as magnetic contact is needed to achieve spin injection into non-magnetic semiconductor. In fact, before the existence of the theoretical guideline, in 1992, Alvarado and Renaud already demonstrated spin

injection into GaAs using vacuum tunneling from Ni STM tip,[26] which implies the importance of tunneling barriers for efficient spin injection. Variable Schottky barriers[27] and an oxide insulation layers[28] have been used to implement spin injection to semiconductors. Remarkably, the crystalline MgO shows unexpected supreme properties for high efficient injection efficiency.[29] As an alternate method, injection into a nonmagnetic semiconductor at zero fields using a ferromagnetic semiconductor has also been achieved,[30] despite the requirements for low temperature and high magnetic fields. The low Cuie temperature is the fundamental obstacle for the application of ferromagnetic semiconductors, such as (Ga,Mn)As.[31]

Spin manipulation, i.e., spin precession introduced by gate voltage or external magnetic fields in non-magnetic channel is another prerequisite for applications of semiconductor spintronics. Rashba spin-orbit interaction, whose strength can be controlled by gate voltage, is initially used to rotate spin polarization in III-V semiconductors or heterostructures.[32] This interaction acts as effective magnetic fields and so does the Dresselhaus spin-orbit interaction.[33] In fact, the SpinFET with a split-gate can modulate the channel width of nonmagnetic material, and thus, the pseudo magnetic fields from the Dresselhaus interaction.[34] The final remark about the SpinFET is its realization on Silicon. Due to the weak spin-orbit interaction, the gate voltage modulation fails to implement transistor action in Silicon based SpinFET, but spin-polarized hot electrons can be controlled by longitudinal electric fields via the modulation of the electron transit time for spin precession in perpendicular magnetic fields.[35]

The spin polarization of either a single charge carrier or an ensemble of carriers is supposed to be preserved during the information transmission in spintronic devices. Since the carrier spin is used to store, transmit, or even process information in spintronic devices, the reliability and fidelity of spin polarization are of great importance. Several major spin relaxation mechanisms, including the D'yakonov-Perel' mechanism,[36] Elliott-Yafet mechanism,[37] Bir-Aronov-Pikus mechanism, and hyperfine interaction with nuclear spins have exhibits clear physical origins and mathematical expressions. In most cases, the spin relaxation inside spintronic devices is determined by experiments due to its sensitivity to thin film quality and interface engineering. Thanks to state-of-the-art growth technologies, electron spin relaxation times vary from less than 1 ns to the order of 100 ns in bulk GaAs,[38] and even higher in GaAs quantum dots,[39] where T_1 exceeds 1 s. Bulk silicon, as a dominate semiconductor material, is demonstrated to have 100 ns spin lifetime and more than 100 μm spin relaxation length.[40] Compared with the nanoscale device geometry of modern semiconductor devices, spin relaxation time/length in semiconductors should be enough for not only implementing functionality in a single spintronic device, but also fulfilling the needs for an assembled logic circuit.

As the SpinFET is regarded as the counterpart of MOSFET, the spin bipolar junction transistor (SBJT) is identical to the conventional bipolar transistor, with a magnetic base, instead of an initial nonmagnetic base.[41] This transistor provides spin-dependent voltage or current gain for majority and minority spin channels, due to the spin-splitting band of the magnetic material in the transistor base. Furthermore, this

nonlinearity in a bipolar transistor operation can introduce novel functions into SBJTs such as wave mixers. GMR-based transistor, with a superlattice base layer composed of ferromagnet and paramagnet, is another type of spintronic transistor, in which the semiconductor emitter and collector, and the GMR base show high efficient modulation for hot electrons, with limitation imposed by the poor current transfer ratio into the semiconductor drain.[42]

Other novel spintronic devices have also been investigated. For example, Dery, Cywiński and Sham[43] proposed spin information transference inside a semiconductor channel with multiple magnetic contacts. And furthermore, an extended design with more magnetic contacts offers fast and programmable logic operations,[44] which preserves the logic functionality in noisy environments. A logic cascading scheme is also developed, with great potential for future 'spin computer'.

In the spin logic devices discussed above, the digital information is eventually expressed by charge. When spintronics meets quantum dots, i.e., the spin polarization of a single electron in a quantum dot represents '0' or '1',[45] quantum-computing-ready fast spintronic devices with long spin relaxation time and less energy dissipation can be finally achieved.

All of the above is a brief review in the fields of spintronics, which have made tremendous impact in physics and industry. It reveals a host of new phenomena in unforeseen experiments, better understanding of microscopic physics, and fruitful commercialization of scientific findings.

1.2 Outline of work presented in this dissertation

The application-oriented research in spintronics roughly includes several levels: (1) physics of magnetic and non-magnetic materials for spintronics, such as spin polarization in ferromagnet and ferromagnetic semiconductors, spin relaxation and manipulation mechanisms in nonmagnetic semiconductors, etc.; (2) spintronic devices that offer novel applications or reveal new phenomena, such as spin amplifier and spin transfer torque; (3) systematic integration of spintronic circuits to provide a variety of logic functionalities. In this dissertation, we have explored the first two levels, focusing on the enhancement of electronic properties of III-V semiconductors by surface chemical treatment, the realization of a lateral spin valve based on a ferromagnet/semiconductor hybrid system, and the magnetoresistance amplification of spin-related signals in a spin transistor. This dissertation is organized as follows.

In Chapter 2, the general physical picture of spin-polarized transport in metal and semiconductor has been discussed, including the spin diffusive analysis and spin-polarized ballistic analysis. A variety of spintronic devices, such as spin valve, spin transistor devices, are also introduced and analyzed.

Chapter 3 includes weak localization/antilocalization measurements and analysis to assess the influence surface treatments on elastic, inelastic and spin-orbit scattering during the electron transport within the two-dimensional electron layer at the InAs surface.

In Chapter 4, we have used spin-valve electrical measurements and analysis, and scanned probe microscopy to assess the influence of interfacial layers and surface treatments on spin-polarized current injection from Co contacts into p-type InAs, and spin-polarized electron transport within the two-dimensional electron layer at the InAs surface. The presence of a tunnel barrier at the interface between the Co contact and InAs surface was found to be essential to achieve nonzero spin injection efficiency. These measurements provide both insight into spin injection and transport processes for the surface electron layer in InAs, and guidance in the design of electronic and spintronic devices based on spin-dependent transport in InAs.

In Chapter 5, to overcome the limitation imposed by the low efficiency of spin injection and extraction and strict requirements for retention of spin polarization within the semiconductor, novel device structures with additional logic functionality and optimized device performance have been developed. We demonstrate and analyze a three-terminal, all-electrical spintronic switching device, combining charge current cancellation by appropriate device biasing and ballistic electron transport. The device yields a robust, electrically amplified spin-dependent current signal despite modest efficiency in electrical injection of spin-polarized electrons. Detailed analyses provide insight into the advantages of ballistic, as opposed to diffusive, transport in device operation, as well as scalability to smaller dimensions, and allow us to eliminate the possibility of phenomena unrelated to spin transport contributing to the observed device functionality. The magnetoresistance amplification scheme and the spin-

dependent ballistic analysis shown in this chapter may inspire a novel design for spintronic devices.

Chapter 6 demonstrates and analyzes the influence of the device geometry on magnetoresistance of nanoscale spin valve structures. Shortcomings of the simplified one-dimensional spin diffusion model for spin valve are elucidated, in comparison with results from two-dimensional numerical simulation and measurements in spin valves.

The work presented in this dissertation, as summarized previously, contributes directly to the realization of spin valve and spin transistor devices in III-V semiconductors, provides a better understanding of spin-polarized transport in nanostructures, and offers new opportunities to engineer the behavior of spintronic devices at the nanoscale.

Reference

[1] International Technology Roadmap for Semiconductors, 2008 Edition.

[2] S. A. Wolf, A. Y. Chtchelkanova, and D. M. Treger, *IBM J. Res. Dev.* **50**, 101 (2006).

[3] M. N. Baibich, J. M. Broto, A. Fert, F. Nguyen Van Dau, F. Petroff, P. Eitenne, G. Creuzet, A. Friederich, and J. Chazelas, *Phys. Rev. Lett*. **61**, 2472 (1988).

[4] G. Binasch, P. Grünberg, F. Saurenbach, and W. Zinn, *Phys. Rev. B* **39**, 4828 (1989).

[5] B. Dieny, V. S. Speriosu, S. S. P. Parkin, B. A. Gurney, D. R. Wilhoit, and D. Maur, *Phys. Rev. B* **43**, 1297 (1991).

[6] P. Bruno, *Phys. Rev. B* **52**, 411 (1995).

[7] F. Mott, *Proc. R. Soc. London, Ser. A* **153**, 699 (1936).

[8] A. Fert, and I. A. Campbell, *Phys. Rev. Lett.* **21**, 1190 (1968); A. Fert, and I. A. Campbell, *J. Phys.* **32**, C1-46 (1971); A. Fert, and I. A. Campbell, *J. Phys. F: Met. Phys.* **6**, 849 (1976).

[9] J. Mathon, and A. Umerski, *Phys. Rev. B* **60**, 1117 (1999).

[10] J. C. Slonczewski, *J. Magn. Magn. Mater.* **159**, L1 (1996).

[11] J. A. Katine, F. J. Albert, R. A. Buhrman, E. B. Myers, and D. C. Ralph, *Phys. Rev. Lett.* **84**, 3149 (2000).

[12] S. S. Parkin, *U. S. Patent* 6,834,005, 2004; *U.S. Patent* 6,898,132, 2005.

[13] D. A. Allwood, Gang Xiong, M. D. Cooke, C. C. Faulkner, D. Atkinson, N. Vernier, R. P. Cowburn**,** *Science* **296**, 2003 (2002).

[14] W. H. Rippard, M. R. Pufall, S. Kaka, S. E. Russek, and T. J. Silva, *Phys. Rev. Lett.* **92**, 027201 (2004).

[15] S. Bandyopadhyay and M. Cahay, *Introduction to spintronics* (CRC Press, Boca Raton, 2008).

[16] S. Datta and B. Das, *Appl. Phys. Lett*. **56**, 665 (1990).

[17] B. I. Zakharchenya, V. G. Fleisher, R. I. Dzhioev, Y. P. Veshchunov, and I. B. Rusanov, *JETP Lett.* **13**, 137 (1971).

[18] M. Johnson and R. H. Silsbee, *Phys. Rev. Lett.* **55**, 1790 (1985).

[19] M. Johnson and R. H. Silsbee, Phys. Rev. B **35**, 4959 (1987).

[20] M. Johnson and R. H. Silsbee, *J. Appl. Phys.* **63**, 3934 (1988).

[21] P. R. Hammar, B. R. Bennett, M. J. Yang, and M. Johnson, *Phys. Rev. Lett.* **83**, 203 (1999).

[22] F. G. Monzon, and M. L. Roukes, *J. Magn. Magn. Mater.* **199**, 632–635 (1999).

[23] G. Schmidt, D. Ferrand, L. W. Molenkamp, A. T. Filip, and B. J. van Wees, *Phys. Rev. B* **62**, R4790 (2000).

[24] A. Fert, and H. Jaffres, *Phys. Rev. B* **64**, 184420 (2001).

[25] V. Ya. Kravchenko, and E. I. Rashba, *Phys. Rev. B* **67**, 121310 (2003).

[26] S. F. Alvarado and P. Renaud, *Phys. Rev. Lett.* **68**, 1387 (1992).

[27] H. J. Zhu, M. Ramsteiner, H. Kostial, M. Wassermeier, H.-P. Schönherr, and K. H. Ploog, *Phys. Rev. Lett.* **87**, 016601 (2001).

[28] A. T. Hanbicki, B. T. Jonker, G. Itskos, G. Kioseoglou, and A. Petrou, *Appl. Phys. Lett*. **80**, 1240 (2002).

[29] X. Jiang, X., R. Shelby, R. Wang, R. M. Macfarlane, S. Bank, J. Harris, and S. S. P. Parkin, *Phys. Rev. Lett.* **90**, 256603 (2003) .

[30] E. Johnston-Halperin, D. Lofgreen, R. K. Kawakami, D. K. Young, L. Coldren, A. C. Gossard, and D. D. Awschalom, Phys. Rev. B **65**, 041306 (2002).

[31] H. Ohno, A. Shen, F. Matsukura, A. Oiwa, A. End, S. Katsumoto, and Y. Iye, Appl. Phys. Lett. **69**, 363 (1996).

[32] T. P. Pareek and P. Bruno, *Phys. Rev. B* **65**, 241305 (2002).

[33] G. Dresselhaus, *Phys. Rev.* **100**, 580 (1955).

[34] S. Bandyopadhyay and M. Cahay, *Appl. Phys. Lett.* 85, 1814 (2004).

[35] B. Huang, D. J. Monsma, and I. Appelbaum, *Appl. Phys. Lett.* **91**, 072501 (2007).

[36] M. I. D'yakonov and V. I. Perel, *Sov. Phys. Solid State* **13**, 3023 (1971).

[37] R. J. Elliott, *Phys. Rev.* **96**, 266 (1954).

[38] J. M. Kikkawa and D. D. Awschalom, *Phys. Rev. Lett.* **80**, 4313 (1998).

[39] S. Amasha, K. MacLean, I. P. Radu, D. M. Zumbühl, M. A. Kastner, M. P. Hanson, and A. C. Gossard, *Phys. Rev. Lett.* **100**, 046803 (2008).

[40] I. Appelbaum1, B. Huang, and D. J. Monsma, *Nature* **447**, 295 (2007).

[41] J. Fabian, I. Zutic, and S. D. Sarma, *Appl. Phys. Lett.* **84**, 85 (2004).

[42] R. Jansen, *J. Phys. D: Appl. Phys.* **36**, R289 (2003).

[43] H. Dery, L. Cywiński, and L. J. Sham, *Phys. Rev. B* **73**, 161307 (2006).

[44] H. Dery, P. Dalal, Ł. Cywiński, L. J. Sham, *Nature* **447**, 573 (2007).

[45] P. Seneor, A. Bernand-Mantel and F. Petroff, *J. Phys.: Condens. Matter* **19,** 165222 (2007).

Chapter 2

Spin transport in semiconductors and metals: a diffusive picture vs. a ballistic picture

In this chapter we analyze and compare diffusive and ballistic electron transport in semiconductor/ferromagnet and paramagnet/ferromagnet hybrid systems. For diffusive transport, the drift and diffusion equations originating from Boltzmann equation explain and predict the behavior of novel spin-dependent devices. Ongoing evolution in spin electronics, motivated by integrating spin-dependent functionality into conventional semiconductor devices, requires not only robust spin injection into semiconductor,[46] but also innovative design with embedded magnetic contacts. Therefore, in addition to non-local spin valve,[47] Datta-Das spin transistor,[48]et al, a variety of spin devices with multiple terminals and modified terminals have been introduced to provide unique performance by manipulating spin-polarized transport.[49]

For nanostructures with spin-polarized electron transport, a diffusive model may not describe the transport behavior appropriately when the critical scale of the nanostructures is within the ballistic transport regime.[50] Thus, we have also adopted the Landauer-Büttiker ballistic electron transport analysis to describe the spin – dependent electron transport in the ballistic regime. The analysis is then employed in Chapter 5 to explain the behavior of a three-terminal all-electrical spintronic device operating in the ballistic regime.

2.1 Spin-dependent drift-diffusion equations: derivation and application

In this section we will derive the spin-dependent drift-diffusion equations from basic thermodynamics expression.[51] Given a grand canonical potential Ω, the electrochemical potential is $\mu = \frac{\partial \Omega}{\partial N}$. If Ω is varying slowly with position, μ is the functional derivative of Ω, i.e., $\mu = \frac{\partial \Omega}{\partial n(\boldsymbol{r})}$, and includes two components,

$$\mu(\boldsymbol{r}) = qV(\boldsymbol{r}) + \zeta(\boldsymbol{r}). \tag{2.1}$$

Thus, the current density, given by the derivative of μ, is

$$\boldsymbol{j} = -\frac{\sigma}{q}\nabla\mu = -\sigma\nabla\mu - \frac{\sigma}{qN(\xi_0)}\nabla n. \tag{2.2}$$

In steady state, $\nabla \cdot \boldsymbol{j} = 0$. Thus,

$$\nabla^2 \mu = 0. \tag{2.3}$$

When spin-up and spin-down channels are separated, the spin-dependent chemical potential is given by

$$\mu_\pm(\boldsymbol{r}) = qV(\boldsymbol{r}) + \frac{1}{N_\pm(\zeta_0)} n_\pm, \tag{2.4}$$

and the current of each channel is then

$$\boldsymbol{j}_\pm = -\frac{\sigma_\pm}{q} \nabla n_\pm. \tag{2.5}$$

The equations due to continuity of the total current and spin flipping between up/down channels then yield two equations to describe spin transport in solids.[52] The continuity equation requires

$$\nabla \cdot \boldsymbol{j} = \nabla \cdot (\boldsymbol{j}_+ + \boldsymbol{j}_-) = 0. \tag{2.6}$$

Consistency between spin-flip process and spin dependent current densities then requires that

$$\nabla \cdot \boldsymbol{j}_\pm = \pm\left(\frac{n_-}{\tau_{-\to+}} - \frac{n_+}{\tau_{+\to-}}\right). \tag{2.7}$$

Substituting the spin-dependent current with the spin-split electrochemical potential, the system of differential equations describing the ECP distribution is then

$$\sigma_+ \nabla^2 \mu_+ + \sigma_- \nabla^2 \mu_- = 0, \tag{2.8a}$$

$$\nabla^2 (\mu_+ - \mu_-) = \frac{\mu_+ - \mu_-}{L^2}, \tag{2.8b}$$

where L is the spin diffusion length, and related to spin scattering time by

$$L = 1 \Big/ \sqrt{\frac{1}{D_- \tau_{-+}} + \frac{1}{D_+ \tau_{+-}}} \;. \tag{2.9}$$

A rigorous derivation of the drift-diffusion equation enables a detailed description of spin transport in semiconductors or metals. These equations also allow one to account for the variable spin relaxation mechanism for different materials. For example in one typical spin transport material, a two-dimensional electron gas,[53]

$$\frac{\partial n_\pm}{\partial t} = \boldsymbol{D}_\pm \frac{\partial^2 n_\pm}{\partial x^2} - \boldsymbol{A} \frac{\partial n_\pm}{\partial x} + \boldsymbol{B} n_\pm, \tag{2.10}$$

where

$$D_\pm = \begin{pmatrix} D_\pm & 0 & 0 \\ 0 & D_\pm & 0 \\ 0 & 0 & D_\pm \end{pmatrix}, \tag{2.11}$$

$$A = \begin{pmatrix} \mu_\pm E & 2\beta_{xz} D_\pm & 0 \\ -2\beta_{xz} D_\pm & \mu_\pm E & 0 \\ 0 & 0 & \mu_\pm E \end{pmatrix}, \tag{2.12}$$

$$B = \begin{pmatrix} D_{\pm}(\beta_{xz}^{2} + \beta_{yz}^{2}) & -\mu_{\pm}E\beta_{xz}D_{\pm} & -\beta_{yx}\beta_{yz}D_{\pm} \\ \mu_{\pm}E\beta_{xz} & D_{\pm}(\beta_{xz}^{2} + \beta_{yz}^{2} + \beta_{yx}^{2}) & 0 \\ -\beta_{yx}\beta_{yz}D_{\pm} & 0 & D_{\pm}\beta_{yz}^{2} \end{pmatrix}. \qquad (2.13)$$

D, ***A*** and ***B*** are tensors for anisotropy of spin transport, containing parameters describing spin diffusive coefficient, spin mobility, spin-orbit interaction strengths and spin relaxation time.

Compared with the simpler scalar spin drift-diffusion equations, these equations account for superposition of spin-up state and spin-down state, caused by either the precession about an external magnetic field, or the spin relaxation due to spin-orbit coupling, i.e., through D'yakonov-Perel' mechanism.[54,55] One should note that the simplification to scalar spin drift-diffusion equations is appropriate for the nanoscale spintronic devices discussed in Chapter 4 and Chapter 5 since the short channel lengths (less than 500 nm for III-V semiconductors, such as InAs) in these devices reduce spin precession about the external magnetic field and the pseudo magnetic fields[56] due to Rashba and Dresselhaus spin-orbit interactions. Following this assumption, the steady state version of the general formula Eqn. (2.10) can be written as

$$\nabla^{2}(n_{+} - n_{-}) + \frac{\mu}{eD} e\vec{E} \cdot \nabla(n_{+} - n_{-}) - \frac{n_{+} - n_{-}}{L^{2}} = 0, \qquad (2.14)$$

where the effective mobility μ and the effective diffusion constant D for spin polarization are given by

$$v = \frac{\sigma_+ v_- + \sigma_- v_+}{\sigma_+ + \sigma_-}, \tag{2.15a}$$

$$D = \frac{\sigma_+ D_- + \sigma_- D_+}{\sigma_+ + \sigma_-}. \tag{2.15b}$$

When $\mu_+ - \mu_+ \ll k_B T$, the linear differential equations for the densities of up-spin and down-spin electrons in a semiconductor can be replaced by the equation for $\mu_+ - \mu_+$,

$$\nabla^2(\mu_+ - \mu_-) + \frac{e\vec{E}}{k_B T} \cdot \nabla(\mu_+ - \mu_-) - \frac{\mu_+ - \mu_-}{L^2} = 0. \tag{2.16}$$

Yu and Flatté point out that the general solutions to Eqn. (2.16) are of a form corresponding to exponential decay in space,[57] with the downstream and upstream spin diffusion lengths, respectively,

$$L_d = \left[-\frac{|eE|}{2} \frac{v}{eD} + \sqrt{(\frac{|eE|}{2} \frac{v}{eD})^2 + \frac{1}{L^2}} \right]^{-1}, \tag{2.17a}$$

$$L_u = \left[\frac{|eE|}{2} \frac{v}{eD} + \sqrt{(\frac{|eE|}{2} \frac{v}{eD})^2 + \frac{1}{L^2}} \right]^{-1}. \tag{2.17b}$$

Furthermore, we can see that

$$L_u L_d = L^2. \tag{2.18}$$

In most spintronic devices, realistic fields are normally small and limited by injection barriers. The spin diffusion behavior is only slightly different from that in the absence of the electric fields. Therefore, the down-stream and up-stream diffusion lengths, L_d and L_u, can be replaced by the intrinsic spin diffusion length L, as shown in Eqn.(2.8). In the case of the spintronic devices based on the low mobility InAs surface electrons, as in Chapter 4 and Chapter 5, the critical field is around 2,000 V/cm, which is beyond the field produced by applied voltage at the semiconductor channel. Thus, Eqn. (2.8) shall provide an appropriate description for the InAs surface electrons. The transport behaviors of all metallic spintronic devices in Chap.6 can also be described satisfactorily by this equation.

2.2 Spin-dependent ballistic model

In nanoscale semiconductor spintronic devices, the mean free path of the nonmagnetic semiconductor channel is normally comparable to the device dimension. Thus, unlike in the diffusive transport regime, in the ballistic regime, a local chemical potential between nearby contacts can't be well defined. The original spin transistor by Datta and Das[58] and other devices[59, 60, 61, 62, 63] with quantum calculation functionalities are based on manipulation of spin states in the ballistic regime. Therefore, the theoretical work on a coherent ballistic transport in a hybrid ferromagnet/semiconductor has been performed[64, 65, 66, 67] and furthermore, a set of spintronic devices with novel effects have been predicted.

The Landauer formula has been established as an appropriate theory for ballistic transport in semiconductor nanostructures.[68] For the spin-dependent transport, the transmission probability is spin-resolved, [69] which counts in the transport trajectories from one channel of spin-splitting injection terminal to the other channel at the extracting terminal. Calculation of magnetoresistance via a quantum mechanical picture, which includes propagating and reflected waves with the Fresnel-type relations[66] explains realistic device behaviors.[70] In Schrodinger's equation, additional terms can integrate spin-orbit interaction and spin relaxation during transport with the original simplified situation. Semiclassical calculation incorporated into the Monte Carlo method[50] offer another possible procedure to estimate the spin-dependent transport behavior by accumulating lots of transport trajectories. While the phase coherence at the spin injection interfaces is broken, i.e., the phase breaking but spin preserving barriers introduce diffusive scattering, the Boltzmann equations with the distribution functions[71] are solved separately in both ferromagnet and semiconductor parts. To describe the spin-splitting transport in a ballistic semiconductor channel, the original electrical potential is replaced by a new function $\zeta_\alpha(x, v_x)$ with the spin index α and an additional term related to Fermi velocity. The boundary condition at the interface between ferromagnetic and semiconductor regions relates the antisymmetric parts of the distribution function in the ferromagnet region to the spin splitting of $\zeta_\alpha(x, v_x)$ in the semiconductor region. It is concluded that the injection coefficient γ is suppressed in the absence of contact barriers, and Sharvin resistance,[72] emerging at the

diffusive interface, serves as indispensable contact resistance for efficient spin injection between ferromagnetic and semiconductor regions.

In the following discussion, the Landauer formulism is applied to a spintronic device in the ballistic regime. Similar to the calculation for the Datta-Das spin transistor, we apply the single subband effective-mass approximation to a hybrid FM/SC/FM device. Thus, Schrodinger equation has the form[64]

$$H = \left[-\frac{\hbar^2}{2} \nabla \frac{1}{m^*(x)} \nabla + V(x,y,z) \right] I + H_{ex}(x) + H_R(x) \ , \qquad (2.19)$$

where $m^*(x)$ is a position-dependent effective mass and $V(\mathrm{x,y,z})$ is the spin-independent electrostatic potential. H_{ex} , H_R are additional spin-dependent terms in the Hamiltonian. The exchange interaction H_{ex} arises from spin-splitting in the ferromagnet, and the Rashba spin-orbit interaction $H_R(x)$ is caused by internal electric fields due to bulk induced asymmetry in the semiconductor. The tunneling barriers cause elastic scattering at the interface, which can be represented by a δ-function potential Uδ(x). The total potential is then modeled by the expression

$$V(x,y,z) = V_0(x,y,z) + U[\delta(x) + \delta(x-L)]. \qquad (2.20)$$

The general Hamiltonian for the ferromagnet can be approximated by[73]

$$H_{ex}(x) = h(x)\vec{m} \cdot \overline{\sigma} \, , \qquad (2.21)$$

where $\vec{m}$ the unit vector in the direction of the magnetization of the ferromagnetic contacts and $\bar{\sigma}$ is the vector of the Pauli spin matrices. In the spin valve geometry, with in-plane $\vec{m}$, this Hamiltonian implies an exchange energy $\Delta = 2h_0$.

The Hermitian Rashba Hamiltonian[74] with a tunable Rashba coefficient[75] has the form

$$H_R(x) = -\frac{i}{2}[\alpha(x)(\sigma \times \nabla) + (\sigma \times \nabla)\alpha(x)]\hat{z}. \tag{2.22}$$

The Rashba parameter α(x) inside a semiconductor channel caused by electric fields near interfaces[76] can be tuned via gate voltages or carrier densities.[77] The kinetic momentum operator in $\hat{x}$ direction with the Rashba Hamiltonian included is given by $\frac{\hbar}{i}\left(\frac{\partial}{\partial x}\right) - \left(\frac{\alpha\, m^*}{\hbar}\right)\sigma_y$. The velocity operator and the current are defined as $\frac{\hat{\mathbf{P}}}{m^*}$ and $\frac{1}{m(x)^*}\mathrm{Re}[\Psi^\dagger \hat{\mathbf{P}}\Psi]$.

In general, the spin-orbit coupling Hamiltonian in a semiconductor can occur by a variety of mechanisms. For simplification, we ignore spin-orbit coupling items in the Schrodinger equation. Thus, the equation for the isolated spin up/down channels is

$$H_\sigma \Psi_\sigma(r) = E_\sigma \Psi_\sigma(r) , \tag{2.23}$$

where the subscript σ denotes spin up/down channels.

By solving for the eigenstates in the ferromagnetic region, the eigenfunction for the FM part $\Psi_{\sigma}^{fm}(r)$ can be written as

$$\Psi_{\sigma}^{fm}(r) = e^{ik_{\sigma}^{fm}\cdot r} + r_{\sigma}e^{-ik_{\sigma}^{fm}\cdot r}, \quad (2.24)$$

And the corresponding energy eigenvalues are given by

$$E_{+}^{fm} = \frac{(\hbar k_{+}^{fm})^2}{2m_e}, \quad (2.25a)$$

$$E_{+}^{fm} = \frac{(\hbar k_{+}^{fm})^2}{2m_e}. \quad (2.25b)$$

The eigenfunction for the semiconductor channel can be written as

$$\Psi_{\sigma}^{sc}(r) = t_{\sigma}e^{ik_{\sigma}^{sc}\cdot r}, \quad (2.26)$$

with the corresponding energy eigenvalues

$$E_{\sigma}^{fm} = \frac{(\hbar k_{\sigma}^{sc})^2}{2m^*} + \Gamma, \quad (2.27)$$

where Γ is the conductance band edge difference between the FM and semiconductor. The reflection coefficient r_{σ} and the tunneling coefficient t_{σ} are deduced from the boundary condition for wave function, following from the quantum mechanical continuity equation.

Here, two boundary conditions are used to derive the spin injection coefficient. One is the continuity boundary condition for the wave function along current injection direction, with the assumption of elastic scattering upon tunneling and can be written as

$$k_\sigma^{fm}(r)\cdot\hat{x} = k_\sigma^{sc}(r)\cdot\hat{x}\,, \tag{2.28}$$

where $k_\sigma^{fm}(r)$ and $k_\sigma^{sc}(r)$ are wave vectors in the FM and semiconductor, determined by the Fermi energy. The other boundary condition is deduced from continuity of the Schrodinger equation with a δ-function potential Uδ(x), which can be written as

$$\Psi_\sigma^{fm}(r)\Big|_{x=0-} = \Psi_\sigma^{sc}(r)\Big|_{x=0+}\,, \tag{2.29.a}$$

$$\frac{\hbar^2}{2m_e}\frac{\partial\Psi_\sigma^{fm}(x)}{\partial x}\Bigg|_{x=0-} + U\Psi_\sigma^{fm}(x=0) = \frac{\hbar^2}{2m^*}\frac{\partial\Psi_\sigma^{sc}(x)}{\partial x}\Bigg|_{x=0+}\,. \tag{2.29.b}$$

Solving both boundary conditions, t_σ is a function of the tunneling potential Uδ(x), which is related to the barrier scattering strength. Thus, the spin-dependent transmission coefficient $T_\sigma = \frac{v_\sigma^{sc}\cdot\hat{x}}{v_\sigma^{fm}\cdot\hat{x}}\left|t_\sigma\right|^2$ can also be calculated. For low temperature $k_B T \ll E_F$, the transmission coefficient only contributes to the spin-dependent transport at the Fermi energy. Therefore, the conductance for each channel can be expressed as

$$G_{\sigma} = \frac{e^2 k_{\sigma}^{fm}}{h\pi} \int_{k_{\sigma}^{fm}} T_{\sigma}(k_{\sigma}^{fm}, U) \frac{k_{\sigma}^{fm} \cdot \hat{x}}{\left| k_{\sigma}^{fm} \right|} . \tag{2.30}$$

The calculation above can be incorporated into part of the procedure to apply the Landauer-Büttiker formalism to spin-polarized nanostructures, i.e., to evaluate the transmission and reflection coefficients. At low temperature and low voltage bias, the original Landauer formula with two spin-nondegenerate terminals is

$$I = \frac{e}{h}[T_{21}\mu_1 - T_{12}\mu_2] = G_{21}V_1 - G_{12}V_2, \tag{2.31}$$

where T_{ij} is representing the transmission probability from terminal i to terminal j.[50]

By modifying the Laudauer formula to account for spin-dependent transport and spin-selective reservoirs, we obtain

$$I_{i,\alpha} = \frac{e}{h}[(N_{ch} - R_{ii}^{\alpha\alpha})\mu_{i,\alpha} - \sum_{j,\beta} T_{ij}^{\alpha\beta} \mu_{j,\beta}] = G_{ij}^{\alpha} V_1 - G_{ji}^{\alpha} V_2, \tag{2.32}$$

where the reflection coefficients $R_{ii}^{\alpha\alpha}$ and the transmission coefficients $T_{ij}^{\alpha\beta}$ are spin-selective, and describe the transport from the channel α in terminal i to the channel β in terminal j. Compared with the semi-classical expression in Eqn. (2.30), for restricted quasi-1D expression with quantized modes, the spin-dependent conductance in the Landauer formula is

$$G_{\sigma} = \frac{e^2}{h} \sum_{n=0}^{N} \sum_{\sigma'=\pm} t^{*}_{\sigma,\sigma'} t_{\sigma,\sigma'} , \tag{2.33}$$

where N is the total number of the transmission modes.

Both the semi-classical treatment and the quantized treatment for spin-polarized ballistic injection reveal the similar fundamental obstacle for efficient spin injection into semiconductor nanostructures. A dimensionless parameter Z defined as $Z = (U / \hbar)\sqrt{2m_e / E_F^{fm}}$ is introduced to describe the scattering strength at the FM/SC interface.[66] For an ideal contact, Z→0, and the injection efficiency is only determined by mismatch of Fermi velocity. In this case, the difference of G_+ and G_- is due to the difference of Fermi velocities for spin up channel and spin down channel in the ferromagnet. For a strong scattering barrier, Z>>1, the ratio of the conductance for spin up/down channels G_+ / G_- is directly proportional to the ratio of Fermi velocities for spin up/down channels v_+^{fm} / v_-^{fm} , which is independent of the Fermi velocity in the semiconductor channel. Therefore, the low spin injection efficiency due to conductance mismatch can also be circumvented by introducing scattering barriers for ballistic spin injection.

Now, we can extend the spin-polarized ballistic model to a typical spintronic device. For a spin-valve configuration, we assume two ferromagnet terminals placed at both sides of a semiconductor channel with two identical elastic scattering barriers. Then, the efficiency of the spin valve is evaluated by comparing the transmission

probabilities of spin-polarized transport in the parallel magnetization configuration and the anti-parallel magnetization configuration. For the parallel configuration, the transmission probability from terminal 1 to terminal 2 is equal to that from terminal 2 to terminal 1, and

$$T_{\sigma}^{P} = T_{12,\sigma}^{P} = T_{21,\sigma}^{P} = \frac{T_{\sigma}}{2 - T_{\sigma}} . \tag{2.34}$$

For the anti-parallel configuration, the transmission probabilities become

$$T_{\sigma}^{AP} = T_{\bar{\sigma}}^{AP} = T_{12,\sigma}^{AP} = T_{12,\bar{\sigma}}^{AP} = T_{21,\sigma}^{AP} = T_{21,\bar{\sigma}}^{AP} = \frac{T_{\sigma} T_{\bar{\sigma}}}{T_{\sigma} + T_{\bar{\sigma}} - T_{\sigma} T_{\bar{\sigma}}} . \tag{2.35}$$

The predicted magnetoresistance can then be calculated from Eqns. (2.34) and (2.35).

Other treatments for spin injection into ballistic semiconductor microstructures have also been developed. Yravchenko and Rashba reveal the Sharvin resistance of the ballistic semiconductor microstructure as the dominant factor for spin injection across FM/SC interface in the Boltzmann regime.[71] A semiclassical calculation based on Monte Carlo simulation has also been developed, including Rashba effects, and predicts both spin valve and spin transistor behaviors in two terminal FM/SC/FM devices.[69]

In conclusion, different treatments for spin injection in ballistic regime can combine the spin precession, Rashba effects, or spin scattering during transport and be simplified to a Landauer formula with spin-preserving reservoirs. The efficiency of

ballistic spin injection is also limited by the difference in electrical transport properties across FM/SC interface and this problem can be overcome by introducing scattering barriers to optimize the injection efficiency.

2.3 Spin transport in metallic hybrid devices

Spin-dependent transport in hybrid microstructures with ferromagnetic and nonmagnetic metals is of interest due to their potential to offer additional practical functionality to present electronic devices.[78] A metal-based spintronic device can be used to analyze the fundamental nature of spin transport in magnetic or nonmagnetic metal. In addition, it also serves as an ideal candidate to evaluate the spin diffusion model. For instance, the "resistance mismatch" obstacle[79] for efficient spin injection has been challenged by a comparison of measurement results on a Py/Ag/Py spin valve and the prediction based on a simplified spin diffusion model. And a systematic study reveals the importance of a two-dimensional spin diffusion model, as shown in Chapter 6.

In the case of low bias voltage, Eqn. (2.16) can be simplified to its most commonly used form,[80]

$$\nabla^2(\mu_+ - \mu_-) = \frac{\mu_+ - \mu_-}{L^2}. \tag{2.36a}$$

Furthermore, for the one-dimensional case,

$$\frac{\partial^2(\mu_+ - \mu_-)}{\partial x^2} = \frac{\mu_+ - \mu_-}{L^2}. \tag{2.36b}$$

The general solution of Eqn. (2.36b) for a uniform metal wire is given by

$$\mu_\pm = a + bx \pm \frac{c}{\sigma_\pm}\exp(-x/L) \pm \frac{d}{\sigma_\pm}\exp(x/L), \tag{2.37}$$

where the coefficients a, b, c, and d are determined by the boundary conditions of continuity of $\mu_\pm$ and conservation of spin up/down current $j_\pm$.

The resistance change in the non-local measurement of spin valve configuration is written as[81]

$$\Delta R = \frac{\sigma_F{}^2 \frac{L}{\sigma_N}\exp(-l/2L)}{(M+1)[M\sinh(l/2L) + \cosh(l/2L)]}, \tag{2.38}$$

where $M = (\sigma_F L_F/\sigma_N L)(1-\sigma_F^2)$, l is the length of nonmagnetic channel between two magnet terminals, and σ_F , σ_N are the conductivities of the ferromagnetic and nonmagnetic wires, respectively. The resistance change measured in the conventional local configuration yields similar equations with an additional factor of two, $\Delta R^{Local} = 2\Delta R$.[82]

In a realistic mesoscopic spin valve, $\sigma_F L_F \ll \sigma_N L$, and thus, $M \ll 1$. The simplified Eqn. (2.38) reveal that ΔR decays exponentially with l. Johnson and Silsbee predict similar $\Delta R \sim l$ relationship using thermodynamic approach.[83] By describing the nonequilibrium population of spin polarized electrons in the nonmagnetic channel as

spin accumulation $\widetilde{M} = I_M T_2/Vol$, the spin-split electrochemical potential associated with $\widetilde{M}$ can be detected by anther FM contact, and the spin transresistance ΔR is

$$\Delta R = \frac{\eta^2 L}{2\sigma A}\exp(-l/L), \tag{2.39}$$

where η is the fractional spin injection efficiency. Therefore, from the comparison of the experimentally observed spin transresistance and the theoretical description above, both η and the spin relaxation length L can be obtained directly. Furthermore, the spin relaxation time τ, and the spin polarization in the ferromagnet can be extracted as well.

The models above clearly domenstrate the procedure of exploring spin diffusion properties in ferromagnet and nonmagnetic materials. The validity and limitation of simplification to one dimensional expression will be discussed in Chapter 6.

2.4 Lateral spin valve based on ferromagnet/semiconductor hybrid system

A lateral spin valve with a nonmagnetic semiconductor channel is regarded as an important type of spintronic device due to its potential for integration with large-scale semiconductor circuits. In a local spin valve, spin polarized electron transport from the terminal 1 to terminal 2 can be calculated for the parallel or antiparallel magnetization configuration, respectively. The magnetoresistance is estimated as

$$MR \approx \frac{\gamma^2/(1-\gamma^2)}{1+\tau_n/\tau_{sf}}, \tag{2.40}$$

where γ is the spin injection coefficient of the spin-selective contacts, τ_n and τ_{sf} are total 'transport time' through the spin valve and the spin scattering time, respectively. Further calculation[24] shows γ is given by

$$\gamma = \frac{J^+ - J^-}{J} = [\Delta r_c + r_F(\Delta\sigma/\sigma_F)]/[r_F + r_c + r_N^*], \tag{2.41}$$

where r_F, r_c and r_N are the characteristic resistances of the ferromagnetic, interface and semiconductor regions of the spin valve devices. The ratio of τ_n and τ_{sf} is given by[24]

$$\frac{\tau_n}{\tau_{sf}} = \frac{t_N \lambda}{\bar{t}_r L^2{}_{sf}}, \tag{2.42}$$

where $\bar{t}_r = h/2e^2(k_f W/\pi) r_C$.

Therefore, when $r_c \to 0$, normally, $\tau_n \ll \tau_{sf}$, and $MR = \gamma^2/(1-\gamma^2)$. In this case, from Eqn. (2.34), the spin asymmetry γ is dramatically reduced by the conductance mismatch. When $r_c >> r_N^*$, the current polarization γ within the semiconductor channel will mainly depend on the spin asymmetry of the contact resistances β. Thus, $\gamma = \Delta r_c/r_c$, and the magnetoresistance is written as

$$MR \approx 2\frac{\gamma^2}{1-\gamma^2}\frac{r_N}{r_c}\frac{L_{sf}}{t_N}, \tag{2.43}$$

which reveals that the MR will decrease with r_c in the case of high barrier resistance.

The discussion above implies that a spin-selective barrier r_c is necessary for efficient spin injection, but excessive r_c will eventually reduce MR. This provides a general the guideline for optimization of lateral spin valves based on ferromagnet and semiconductor.

2.5 Multi-terminal spintronic devices and spintronic circuits

Although the paradigm shift from new spintronic effect to electronic devices has been achieved by the discovery of giant magnetoresistance (GMR) effects,[84] spintronic circuits with additional information processing functionality with spin freedom remains to be realized. The initial spintronic devices are mainly two-terminal local spin valves based on vertical thin film structures. In this geometry, spin and charge currents coupled and the information are ultimately encoded by charge. The practical usage of vertical spin valves is limited by the spin-charge current coupling and the requirement of external magnetization during device switching. Therefore, spin valves with non-local geometry, pioneered by Johnson and Silsbee,[85] have been used to decouple spin-charge currents. An alternative method to decouple spin-charge currents relies on spin Hall effect, where an electric charge current gives rise to a

transverse spin imbalance due to asymmetric spin scattering caused by spin-orbit interaction. [86, 87]

While spin-transfer torque effects [88] can enable magnetization flipping by spin polarized current inside circuits, electric field control over the switch of spin polarization would still be preferred, and thus, Datta-Das type spin transistor and bipolar spin transistor, [89] in which a gate voltage is introduced to switch spin transistor instead of changing magnetization configuration of source/drain ferromagnet terminals, have generated extensive interest.

Two-terminal variants of the original spin valves have only limited logic functionalities. By introducing an additional ferromagnet terminal, the processing of digital information represented by spin up/down binary is expanded.[49] The demonstration of decoupling spin and charge current in Al strip with three Co terminals has been achieved, [90] And the spin amplifier with a third spin-selective contact can eventually solve the spin preservation issue inside the circuits based on operation in the diffusive regime of electron transport within the semiconductor.[91, 92] The similar magnetoresistance amplification operated in the ballistic regime will be discussed in Chapter 5.

2.6 Conclusions

In this chapter, the general analysis of spin transport and various fundamental spintronic devices have been discussed. Both the spin diffusive transport and the spin-polarized ballistic transport are discussed and applied to realistic spintronic devices. The low efficiency of spin injection and extraction and strict requirements for spin polarization preservation limit the performance of semiconductor spintroice devices. Therefore, novel device structures have also been proposed theoretically and investigated experimentally. It has been suggested, and Chapter 5 will show, that an extra spin-selective terminal in a spin-dependent device can play an important role to introduce additional logic functionality and optimize the device performance.[93]

Reference

[46] S. A. Wolf, D. D. Awschalom, R. A. Buhrman, J. M. Daughton, S. von Molnár, M. L. Roukes, A. Y. Chtchelkanova, D. M. Treger, *Science* **294**, 1488 (2001).

[47] F. J. Jedema, A. T. Filip, and B. J. van Wees, *Nature* **410**, 345 (2001).

[48] S. Datta and B. Das, *Appl. Phys. Lett*. **56**, 665 (1990).

[49] H. Dery, P. Dalal, Ł. Cywiński, L. J. Sham, *Nature* **447**, 573 (2007).

[50] H. X. Tang, F. G. Monzon, F. J. Jedema, A. T. Filip, B. J. van Wees, and M. L. Roukes, in *Semiconductor Spintronics and Quantum Computation*, edited by D. Awschalom, D. Loss, and N. Samarth (Springer, New York, 2002), pp. 31–92.

[51] L. J. Sham, *Spintronics* (U. C. San Diego lectures, San Diego, 2008).

[52] T. Valet, and A. Fert, *Phys. Rev. B* **48**, 7099 (1993).

[53] S. Saikin, *J. Phys.: Condens. Matter* **16**, 5071 (2004).

[54] M. I. D'yakonov, V. I. Perel, *Soviet Phys. JETP* **33**, 1053 (1971).

[55] M. I. D'yakonov, V. Yu. Kachorovskii, *Sov. Phys. Semicond.* **20**, 110 (1986).

[56] Z. G. Yu, and M. E. Flatté, *Phys. Rev. B* **66**, 201202 (2002).

[57] Z. G. Yu, and M. E. Flatté, *Phys. Rev. B* **66**, 235302 (2002).

[58] S. Datta, and B. Das, *Appl. Phys. Lett.* **56**, 665 (1990).

[59] M. Friesen, P. Rugheimer, D. E. Savage, M. G. Lagally, D. W. van der Weide, R. Joynt, and M. A. Eriksson, *Phys. Rev. B* **67**, 121301 (2003).

[60] R. Hanson, L. M. K. Vandersypen, L. H. W. van Beveren, J. M. Elzerman, I. T. Vink, and L. P. Kouwenhoven, *Phys. Rev. B* **70**, 241304 (2004).

[61] A. A. Kiselev, and K. W. Kim, *Appl. Phys. Lett.* **78**, 775 (2001).

[62] S. I. Kiselev, J. C. Sankey, I. N. Krivorotov, N. C. Emley, R. J. Schoelkopf, R. A. Buhrman, and D. C. Ralph, *Nature* **425**, 380 (2003).

[63] M. J. Stevens, A. L. Smirl, R. D. R. Bhat, A. Najmaie, J. E. Sipe, and H. M. van Driel, *Phys. Rev. Lett.* **90**, 136603 (2003).

[64] H. B. Heersche, Th. Schäpers, J. Nitta, and H. Takayanagi, *Phys. Rev. B* **64**, 161307(R) (2002).

[65] Th. Schäpers, J. Nitta, H. B. Heersche, and H. Takayanagi, *Phys. Rev. B* **64**, 125314 (2002).

[66] D. Grundler, *Phys. Rev. B* **63**, 161307(R) (2001).

[67] C.-M. Hu and T. Matsuyama, *Phys. Rev. Lett.* **87**, 066803 (2001).

[68] S. Datta, *Electronic Transport in Mesoscopic Systems* (University Press, Cambridge, 1995).

[69] X. L. Tang, F. G. Monzon, R. Lifshitz, M. C. Cross, and M. L. Roukes, *Phys. Rev. B* **61**, 4437 (2000).

[70] T. Matsuyama, C.-M. Hu, D. Grundler, G. Meier, and U. Merkt, *Phys. Rev. B* **65**, 155322 (2002).

[71] V. Y. Kravchenko and E. I. Rashba, *Phys. Rev. B* **67**, 121310 (2003).

[72] Yu.V. Sharvin*, Sov. Phys. JETP* **21**, 655 (1965).

[73] X. Zhang, B-Z. Li, G. Sun, and F-C. Pu, *Phys. Rev. B* **56**, 5484 (1999).

[74] U. Zülicke and C. Schroll, *Phys. Rev. Lett.* **88**, 029701 (2002).

[75] E. I. Rashba, *Sov. Phys. Solid State* **2**, 1109 (1960).

[76] E. A. de Andrada e Silva, G. C. La Rocca, and F. Bassani, *Phys. Rev. B* **55**, 16 293 (1997).

[77] T. Matsuyama, R. Kürsten, C. Meißner, and U. Merkt, *Phys. Rev. B* **61**, 15 588 (2000).

[78] M. Johnson, *Magnetoelectronics* (Elsevier, Oxford, 2004).

[79] G. Schmidt, D. Ferrand, L. W. Molenkamp, A. T. Filip, and B. J. van Wees, *Phys. Rev. B* **62**, 4790 (2000).

---

[80] F. J. Jedema, M. S. Nijboer, A. T. Filip, and B. J. van Wees, *Phys. Rev. B* **67**, 085319 (2003).

[81] M. Johnson, *IEEE Trans. Electron Devices* **54**, 1024 (2007).

[82] A. Fert, J. M. George, H. Jaffres, R. Mattana, *IEEE Trans. Electron Devices* **54**, 921 (2007).

[83] M. Johnson and R. H. Silsbee, *Phys. Rev. B* **35**, 4959 (1987).

[84] M. N. Baibich, J. M. Broto, A. Fert, F. Nguyen Van Dau, F. Petroff, P. Etienne, G. Creuzet, A. Friederich, and J. Chazelas, *Phys. Rev. Lett.* **61**, 2472 (1988).

[85] M. Johnson and R. H. Silsbee, *Phys. Rev. Lett.* **55**, 1790 (1985).

[86] Y. K. Kato, R. C. Myers, A. C. Gossard, D. D. Awschalom, *Phys. Rev. Lett.* **93**, 176601 (2004).

[87] T. Kimura, Y. Otani, T. Sato, S. Takahashi, and S. Maekawa, *Phys. Rev. Lett.* **98**, 156601 (2007).

[88] E. B. Meyers, D. C. Ralph, J. A. Katine, R. N. Louiie, and R. A. Buhrmann, *Science* **285**, 867 (1999).

[89] I. Žutić, J. Fabian, and S. C. Erwin, *J. Phys.: Condens. Matter* **19**, 165219 (2007)

[90] M. Urech, V. Korenivski, N. Poli, and D. B. Haviland, *Nano. Lett.* **6**, 871 (2006).

[91] H. Dery, L. Cywinski, and L. J. Sham, *Phys. Rev. B* **73**, 161307 (2006).

[92] D. Saha, M. Holub, and P. Bhattacharya, *Appl. Phys. Lett.* **91**, 072513 (2007).

[93] H. Dery, L. Cywinski and L. J. Sham, *Phys. Rev. B* **73**, 041306 (2006).

Chapter 3

Electrical transport and spin diffusion in InAs: a study by weak localization and antilocalization measurement

In this chapter, the magnetoconductivity measurement in Corbino disks on the InAs surface inversion layer at the surface of p-type InAs is presented. The quantum correction to classic Drude parabola is observed in the magnetoconductivity curve. Weak localization/antilocalization effect is used to explain the magnetoconductivity behavior and to investigate the electrical transport in InAs surface electron layer. The fitting results obtained from comparison of the experiment and theory reveal the details of relaxation mechanisms in the InAs surface electron layer. It is shown that sulfur-based surface treatments on the InAs surface prolong spin relaxation time, and

thus, enhance the performance of spintronic devices based on the surface electron layer. A spin scattering length of 220±20nm is measured on original p-type InAs, and a sulfur-based surface treatment is found to increase the spin scattering length to 250±20nm.

3.1 InAs-based devices for spintronic application

Spintronic devices based on ferromagnet/semiconductor hybrid structures offer the potential for realization of logic and switching performance with high speed and low power consumption, and the possibility to integrate additional functionalities such as nonvolatile information storage with more conventional semiconductor electronics.[94] Therefore, spintronic devices based on n-GaAs[95,96], III-V semiconductor based heterostructures[97,98], and Silicon[99,100,101,102] have been experimentally realized. Among these semiconductors, structures incorporating narrow-bandgap semiconductors offer potential advantages for spintronic device applications due to their combination of high electron mobility and strong spin-orbit coupling.[103] InAs offers the additional advantages including a strong Rashba effect[104] for coupling of spin-polarized transport to transverse electric fields, required for Datta-Das spin transistor device.[105] Furthermore, it is demonstrated that the tunable Rashba coefficient of the surface inversion layer on p-InAs bulk varies from 1×10^{-11} eVm to 3×10^{-11} eVm, with gate voltage modulation,[106] providing a large variation ratio compared with other III-V semiconductors, and thus, a great potential for future

spintronic application, such as realization of electric-field-controlled switching of spin polarization.

The inherent presence of a surface electron layer facilitates strong coupling of electrons in InAs to a ferromagnetic contact.[107,108] It is noted that for efficient spin injection into a semiconductor, δ-doping in the semiconductor region, or a low-work-function ferromagnet thin film at the ferromagnet/tunnel barrier interface[99] is need to reduce the thickness or height of the excessive tunnel barrier. In InAs, the excessive barrier problem would be also circumvented automatically, due to its surface inversion/accumulation layer.

3.2 Influence of surface passivation on electrical properties of InAs surface electron layers

Surface treatments of III-V compound semiconductors with ammonium sulfide ($(NH_4)_2S_x$) have been reported as an effective and reproducible method to improve both the electrical and optical properties.[109] Such treatments can decrease substantially the surface defect density, and thus, enhance characteristic features of devices based on treated materials. The treated surface is covered by an amorphous sulfide layer, mostly bonded with III group elements, which benefits the device performances, such as PL intensity, C-V characteristics of the metal-insulator-semiconductor (MIS) structure, and contact-dependent Schottky barrier. Here, in addition to improvements

of spin-independent effects, we focus on enhancing the spin-related performance by reducing spin-orbit scattering centers on the InAs surface.

The wet chemical treatment by $(NH_4)_2S_x$ is as follows: InAs wafers were first cleaned in acetone and isopropanol with ultrasonic agitation for 3 min each. This was supposed to leave the InAs surface with a native oxide layer.[110] After cleaning in organic solvents as above, the InAs wafers were then soaked for 15min at 25°C in 7% $(NH_4)_2S$ solution in which extra sulfur was dissolved to form a sulfur-saturated solution. This latter process has been demonstrated previously to result in removal of the native oxide and formation of In-S bonds at the InAs surface,[110] as shown in Figure 3.1(b).

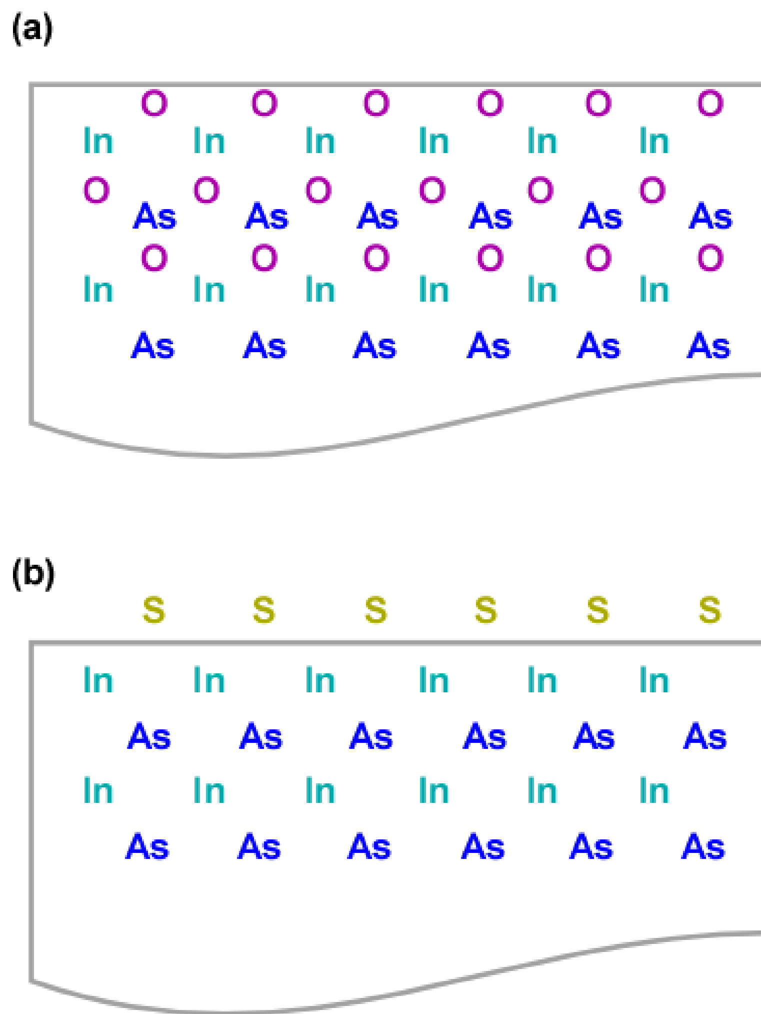

Figure 3.1: (a) Schematic of InAs surface before sulfuration treatments. The amorphous surface layer consists of native In-O_x and As-O_x components. (b) Schematic of $(NH_4)_2S_x$ passivated InAs surface. This idealized structural model only involves In-S bonding. (after D. Y. Petrovykh, J. M. Sullivan, and L. J. Whitman, *Surf. Interface Anal.* **37**, 989 (2005))

3.3 Weak localization and antilocalization measurements on InAs surface inversion layers

To obtain detailed information concerning transport scattering lengths, Corbino disk structure, as illustrated schematically in Figure 3.2, is used to examine weak localization/antilocalization (WL/WAL) effects in the InAs surface electron layer. After passivated by $(NH_4)_2S_x$ solution, approximately 40 nm of SiO_2 was deposited by electron beam evaporation system on the cleaned InAs surface to protect the transport channel from degrading in the following fabrication process for Corbino disk structures. Standard electron beam lithography is used to define circular contacts of Corbino disks. 50 nm Au layer is then deposited by electron beam evaporation system, immediately after removal of SiO_2 in the contact area on top of the InAs wafer. Finally, the external leads and pads were made for measurements in low-temperature cryostat system.

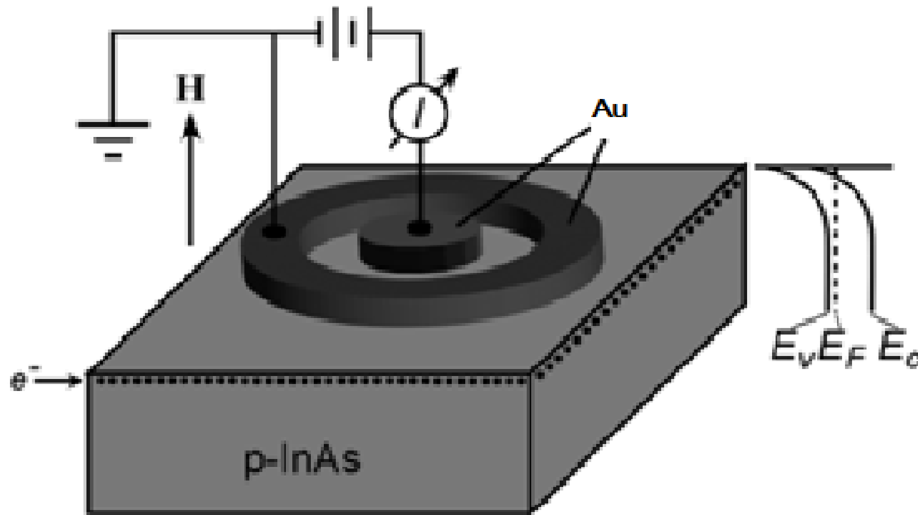

Figure 3.2: Schematic diagram of Corbino disk device structure, measurement configuration, and InAs electronic structure.

Figure 3.3 shows typical magnetoconductance characteristics for a Corbino disk device with the InAs native oxide present on the surface between the contacts. The classic Drude parabolas are observed in measured magnetoconductance characteristics at high magnetic fields and the quantum corrections appear at low magnetic fields. Subtracting Drude parabolas from the initial magnetoconductance characteristics, the remaining magnetoconductance curves are due to the weak localization/antilocalization quantum correction to classic Drude models, as shown in Figure 3.4.

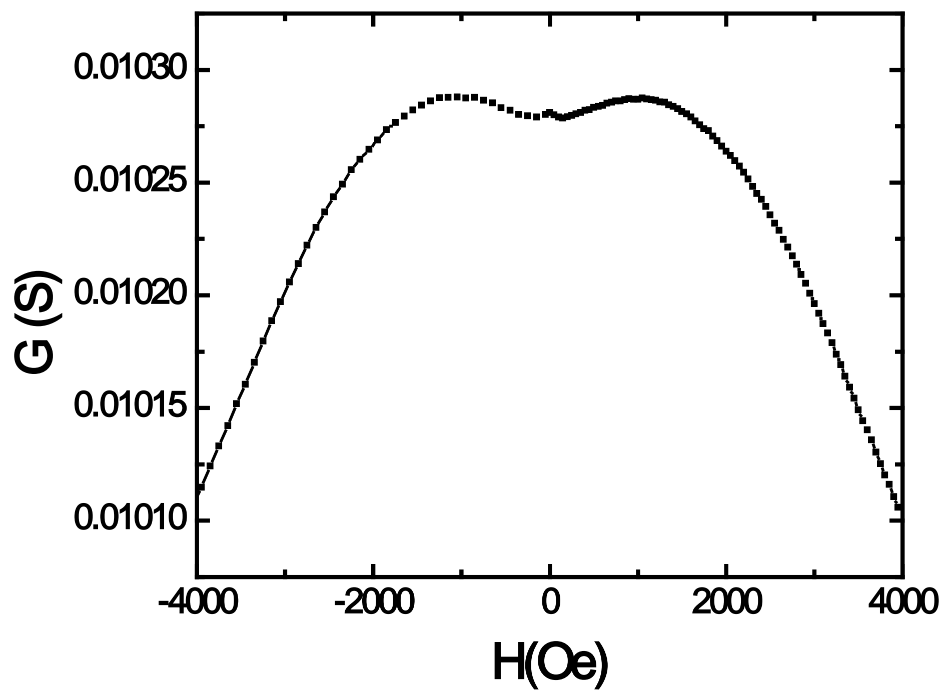

Figure 3.3: Magnetoconductance measured in Corbino disk structure. The classic Drude parabolas appear in the magnetoconductance characteristics at high magnetic fields and the quantum corrections become dominant at low magnetic fields.

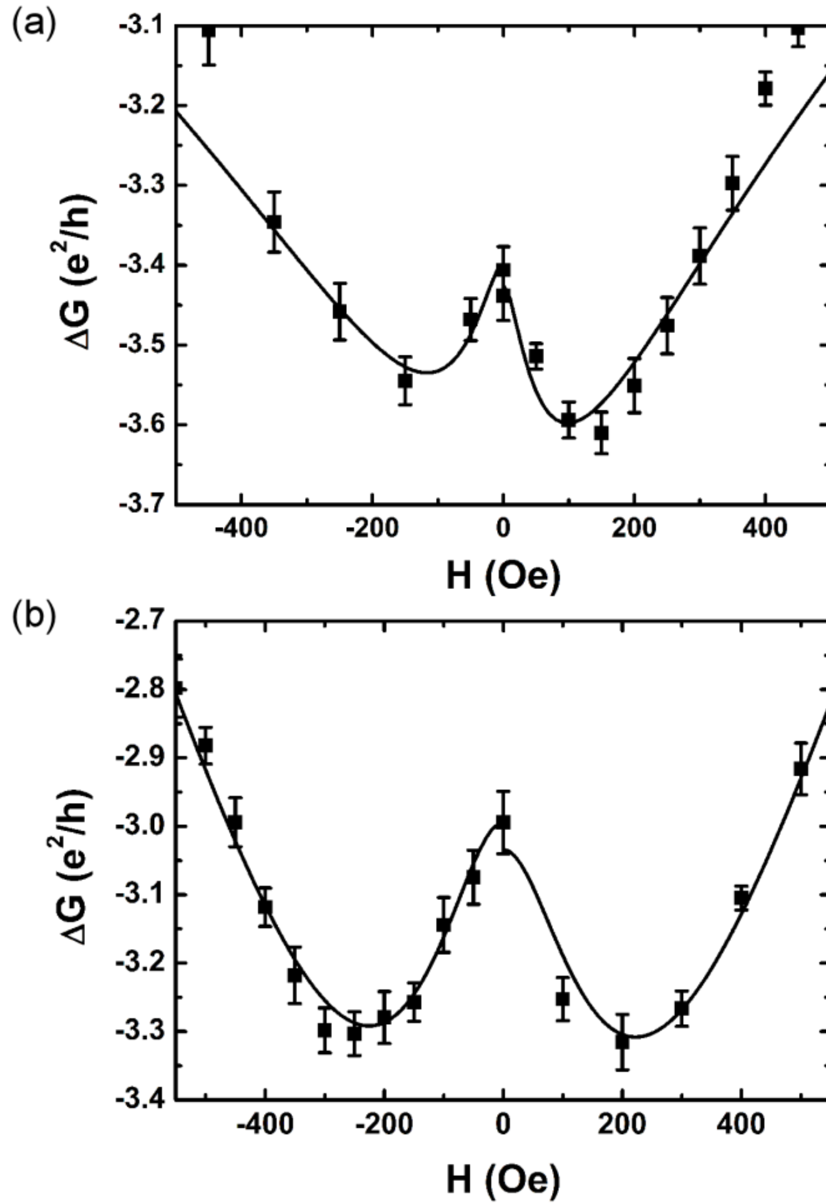

Figure 3.4: Magnetoconductance measured in Corbino disk device structure, along with fitted curves from which elastic, inelastic, and spin-orbit scattering lengths are determined. (a) Corbino disk device with native oxide on InAs surface, and (b) Corbino disk device with sulfur-passivated InAs surface.

These measurements provide information about elastic, inelastic, and spin scattering lengths and have also been used to analyze spin-orbit coupling in GaAs and in InAs inversion layers[111,112] According to the Hikami-Larkin-Nagaoka theory, [113] the magnetoconductance as a function of external magnetic field applied perpendicular to the InAs surface is given by

$$\Delta G = -\frac{e^2}{2\pi^2 h}\left\{\Psi\left(\frac{1}{2}+\frac{B_e}{B}\right)-\Psi\left(\frac{1}{2}+\frac{B_i+B_{so}}{B}\right)+\frac{1}{2}\left[\Psi\left(\frac{1}{2}+\frac{B_i}{B}\right)-\Psi\left(\frac{1}{2}+\frac{B_i+2B_{so}}{B}\right)\right]\right\}, \quad (3.1)$$

where B is the applied magnetic field, Ψ is the digamma function, and B_e, B_i, and B_{so} are characteristic magnetic fields for elastic, inelastic, and spin-orbit scattering. Each characteristic field, B_α, with $\alpha = e$, i, or so, can be related to a corresponding scattering time τ_α according to

$$B_\alpha = \frac{\hbar}{4De\tau_\alpha}, \quad (3.2)$$

where D is the electron diffusion constant, given by $D = (1/2)v_f^2\tau_e$, and v_f is the electron Fermi velocity, determined to be 1.0×10^8cm/s from the relationship[114]

$$v_f = \frac{\hbar\sqrt{2\pi n_s}}{m^*} \quad (3.3)$$

.

The characteristic fields and consequently the associated scattering times can be determined by fitting measured magnetoconductance characteristics.

Analysis of these characteristics based on Eqs. (3.1) and (3.2) yields elastic, inelastic, and spin-orbit scattering lengths l_e = 54±2nm, l_i = 540±70nm, and l_{so} = 350±20nm, respectively. Figure 3.4(b) shows magnetoconductance characteristics of a Corbino disk device for which the exposed InAs surface was treated with a sulfur-containing solution as described in Section 3.2. This surface treatment results in larger elastic, inelastic, and spin-orbit scattering lengths – l_e = 77±2nm, l_i = 720±40nm and l_{so} = 610±10nm. We speculate that the improvements in elastic and spin-orbit scattering lengths are due to the reduction in surface state density that arises from the sulfur-based chemical treatment.[115]

As we discussed above, Hikami-Larkin-Nagaoka [HLN] theory fitted to the corrected magnetoconductance characteristics provides information about elastic, inelastic, and spin scattering lengths[116], has been used to analyze spin-orbit coupling in GaAs and in InAs inversion layers. But it failed to achieve an appropriate fit in some cases, for example, the magnetoconductance curves measured in InAs inversion layers in Ref. 117, and the curves in Figure 3.4(b) at the fields larger than 400 Oe, since it only accounts for the Elliott-Yafet spin relaxation mechanism while ignoring the D'yakonov-Perel' mechanism, which is the dominant mechanism in the two dimensional electron system in III-V semiconductors with a cubic crystal structure. The Iordanskii-Lyanda-Geller-Pikus [ILP] theory incorporates both of these spin relaxation mechanisms [118, 119] and provides a much better fit to the magnetoconductance characteristics measured previously in III-V semiconductors.[120]

According to ILP theory, the weak localization/antilocalization correction to the magnetoconductance is given by[119]

$$\Delta\sigma(B) = -\frac{e^2}{4\pi^2\hbar}\left\{\frac{1}{a_0} + \frac{2a_0 + 1 + \frac{B_{SO}}{B}}{a_1\left(a_0 + \frac{B_{SO}}{B}\right) - 2\frac{B'_{SO}}{B}} - \sum_{n=0}^{\infty}\left(\frac{3}{n} - \frac{3a_n^2 + 2a_0\frac{B_{SO}}{B} - 1 - 2(n+1)\frac{B'_{SO}}{B}}{\left(a_n + \frac{B_{SO}}{B}\right)a_{n-1}a_{n+1} - 2\frac{B'_{SO}}{B}[(2n+1)a_n - 1]}\right) + 2\ln\frac{B_{tr}}{B} + \Psi\left(\frac{1}{2} + \frac{B_\varphi}{B}\right) - 3\Psi(1)\right\}, \tag{3.4}$$

where $a_n = n + \frac{1}{2} + \frac{B_\varphi}{B} + \frac{B_{So}}{B}$, $B_{tr} = \frac{c}{4e\hbar D\tau_1}$, $B_{t\varphi} = \frac{c}{4e\hbar D\tau_\varphi}$,

$B_{SO} = \frac{c}{4e\hbar D}(2\Omega_1^2\tau_1 + 2\Omega_3^2\tau_3)$, $B'_{SO} = B_{SO}^{(1)} = \frac{c}{2e\hbar D}\Omega_1^{(1)2}\tau_1$ or

$B'_{SO} = B_{SO}^{(2)} = \frac{c}{2e\hbar D}\Omega_1^{(2)2}\tau_1$.

Specifically, this model is highly appropriate for transport in the InAs surface inversion layer, since Rashba effects due to structural inversion asymmetry dominate the spin relaxation.[121] The ILP theory can be simplified by neglecting Elliott-Yafet spin relaxation and spin-orbit scattering from bulk inversion asymmetry. The characteristic fields for transport scattering and spin-orbit scattering are determined by

fitting measured magnetoconductance characteristics to the simplified ILP theory and can be related to the corresponding scattering times according to characteristic field, B_α, with $\alpha = e$, i, or so, can be related to a corresponding scattering time τ_α according to Eqn. (3.4).

Figure 3.5(a) shows measured magnetoconductance characteristics and fitted curves from ILP theory for a Corbino disk device with the InAs native oxide present on the surface between the contacts. Figure 3.5(b) shows magnetoconductance characteristics fitted curves from ILP theory of a Corbino disk device for which the InAs surface between terminals was treated with a sulfur-containing solution. The fitted curves by HLN and ILP theory are shown as the solid and dashed lines, respectively. ILP theory incorporates the dominant D'yakonov-Perel' spin relaxation mechanism in InAs surface electron layers and provides better descriptions for measured magnetoconductance characteristics than HLN theory, as shown in Figure 3.5(a) and Figure 3.5(b). The analysis based on ILP theory yields the transport and spin-orbit scattering lengths with the native oxide presence, to be l_e = 85±5nm and l_{so} = 220±20nm, respectively. Smaller elastic and larger spin-orbit scattering lengths l_e = 65±5nm, and l_{so} = 250±20nm, are measured after surface treatment.

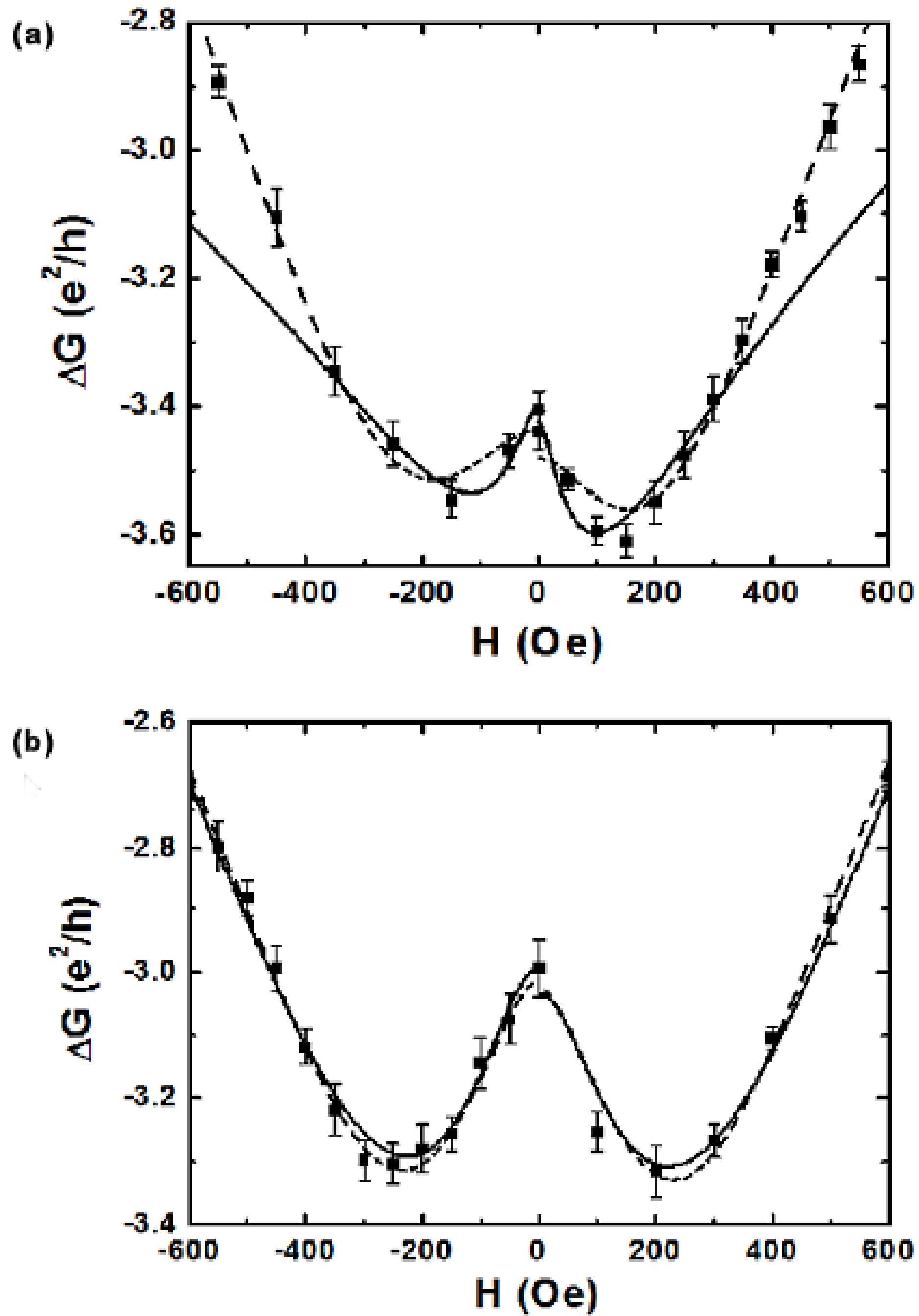

Figure 3.5: Magnetoconductance measured in Corbino disk device structure, along with fitted curves from ILP theory, for (a) Corbino disk device with native oxide on InAs surface, and (b) Corbino disk device with sulfur-passivated InAs surface.

We speculate that the sulfur-passivation removes the InAs native oxide layers, which are supposed to suppress spin-orbit relaxation,[122] and eliminates surface states to improve the electrical properties of InAs surface layers.[109] But it may also introduce a rougher surface and thus, reduce the scattering lengths.[123] The surface scattering lengths are determined by both the density of surface scatters and surface roughness. Therefore, there are no clear estimations for the effects of sulfur-passivation on the scattering lengths. Hall measurements show carrier densities increased after sulfur-passivation and indicate a stronger band bending at the surface.[110] Higher carrier densities result in more electron-electron scattering at lower temperature and eventually reduce the elastic scattering length. We also note that the Rashba coefficient decreases with higher carrier densities,[124] which implies less spin-orbit coupling through Rashba effects and thus, a longer spin-orbit scattering length. We speculate that the deterioration of the elastic scattering length and the improvements of the spin-orbit scattering lengths arise from a combination of these effects. In addition we note that the spin-orbit scattering lengths, l_{so}, obtained from these measurements are in reasonable agreement with the spin diffusion length l_{so} determined from spin-valve measurements, as described in the next chapter.

3.4 Conclusions

We have used weak localization/antilocalization measurements and analysis to assess the influence of surface treatments on elastic, inelastic and spin-orbit scattering

during the electron transport within the two-dimensional electron layer at the InAs surface. Weak localization/antilocalization measurements at 4.2K yielded spin scattering lengths in the range of ~250nm. These measurements provide both insights into ballistic and spin-polarized transport for the surface electron layer in InAs, and guidance in the design of electronic and spintronic devices based on spin-dependent and/or ballistic electron transport in InAs.

Acknowledgments: This chapter, in full, has been submitted for publication of the material as it may appear in the Journal of Applied Physics, 2009. Zhu, Lei; Yu, Edward T., “Influence of surface treatment and interface layers on electrical spin injection efficiency and transport in InAs”, AIP Publishing, 2009. The dissertation author was the primary investigator and author of this paper.

Reference

[94] I. Zutic, J. Fabian, and S. Das Sarma, *Rev. Mod. Phys.* **76**, 323 (2004).

[95] B.T. Jonker *et al*., *MRS Bulletin,* October (2003).

[96] T. Inokuchi *et al*., *Appl. Phys. Express* **2**, 023006 (2009).

[97] Y. D. Park, B. T. Jonker, B. R. Bennett, G. Itskos, M. Furis, G. Kioseoglou, and A. Petrou, *Appl. Phys. Lett*. **77**, 3989 (2000).

[98] H. C. Koo, H. Yi, J.-B. Ko, J. Chang, S.-H. Han, D. Jung, S.-G. Huh, and J. Eom, *Appl. Phys. Lett*. **90**, 022101 (2007).

[99] B. C. Min, K. Motohashi, C. Lodder, and R. Jansen, *Nat. Mater.* **5**, 817 (2006).

[100] I. Appelbaum, B. Huang, and D. J. Monsma, *Nature* **447**, 295 (2007).

[101] B. T. Jonker, G. Kioseoglou, A. T. Hanbicki, C. H. Li, and P. E. Thompson, *Nat. Phys.* **3**, 542 (2007).

[102] O. M. J. van't Erve, A. T. Hanbicki, M. Holub, C. H. Li, C. Awo-Affouda, P. E. Thompson, and B. T. Jonker, *Appl. Phys. Lett.* **91**, 212109 (2007).

[103] A. W. Cummings, R. Akis, and D. K. Ferry, *Appl. Phys. Lett.* **89**, 172115 (2006).

[104] D. Grundler, *Phys. Rev. Lett.* **84**, 6074 (2000).

[105] S. Datta and B. Das, *Appl. Phys. Lett.* **56**, 665 (1990).

[106] T. Matsuyama, R. Kürsten, C. Meissner, and U. Merkt, *Phys. Rev. B* **61**, 15588 (2000).

[107] J. P. McGuire, C. Ciuti, and L. J. Sham, *Phys. Rev. B* **69**, 115339 (2004)

[108] K. Yoh, H. Ohno, Y. Katano, K. Mukasa, and M. Ramsteiner, *J. Cryst. Growth* **251**, 337 (2003).

[109] V. N. Bessolov and M. V. Lebedev, *Semiconductors* **32**, 1281(1998).

[110] D. Y. Petrovykh, M. J. Yang and L. J. Whitman, *Surf. Sci.* **523**, 231 (2003).

---

[111] P.D. Dresselhaus, C.M.A. Papavassiliou, R.G. Wheeler, and R.N. Sacks, *Phys. Rev. Lett.* **68**, 106 (1992).

[112] C. Schierholz, T. Matsuyama, U. Merkt, and G. Meier, *Phys. Rev. B* **70**, 233311 (2004).

[113] S. Hikami, A.I. Larkin, and Y. Nagaoka, *Prog. Theor. Phys.* **63**, 707 (1980).

[114] S. Datta, *Electronic Transport in Mesoscopic Systems* (Cambridge University Press, Cambridge, 1995).

[115] S. Ichikawa, N. Sanada, N. Utsumi, and Y. Fukuda, *J. Appl. Phys.* **84**, 3658 (1998).

[116] S. Hikami, A.I. Larkin, and Y. Nagaoka, *Prog. Theor. Phys.* **63**, 707 (1980).

[117] Y. Kawaguchi, I. Takayanagi, and S. Kawaji, *J. Phys. Soc. Jpn.* **56**, 1293 (1987)

[118] S.V. Iordanskii, Yu. B. Lyanda-Geller, and G. E. Pikus, *JETP Lett.* **60**, 206(1994).

[119] W. Knap, C. Skierbiszewski, A. Zduniak, E. Litwin-Staszewska, D. Bertho, F. Kobbi, J. L. Robert, G. E. Pikus, F. G. Pikus, S. V. Iordanskii, V. Mosser, K. Zekentes, and Yu. B. Lyanda-Geller, *Phys. Rev. B* **53**, 3912 (1996).

[120] C. Schierholz, T. Matsuyama, U. Merkt, and G. Meier, *Phys. Rev. B* **70**, 233311 (2004).

[121] S. Lamari, *Phys. Rev. B* **64**, 245340 (2001).

[122] S. Gardelis, C. G. Smith, C. H. W. Barnes, E. H. Linfield, and D. A. Ritchie, *Phys. Rev. B* **60**, 7764 (1999).

[123] Q. Hang, F. Wang, P. D. Carpenter, D. Zemlyanov,D. Zakharov,E. A. Stach, W. E. Buhro, and D. B. Janes, *Nano. Lett.* **8**, 49 (2008).

[124] C. Schierholz, T. Matsuyama, U. Merkt, and G. Meier, *Phys. Rev. B* **70**, 233311 (2004).

Chapter 4

Electrical spin injection and detection in InAs surface electron layers

In this chapter, we demonstrate fully electrical spin injection and detection in the InAs surface electron layer. Spin-valve and scanned probe microscopy measurements are used to investigate the influence of sulfur-based surface treatments and electrically insulating barrier layers on spin injection into, and spin transport within, the two-dimensional electron layer at the surface of p-type InAs at 4.2K. Spin injection efficiencies and spin diffusion lengths are determined using magnetoresistance measurements on spin-valve structures with variable channel lengths, with spin diffusion lengths corroborated by analysis of weak localization/anti-localization behavior in Corbino disk structures, as discussed in Chapter 3. By applying a conventional spin valve model to the measured magnetoresistance, we

show that insertion of a thin insulating layer, in this case Al_2O_3, provides an injection coefficient around ~1.4%. InAs surface passivation is found to substantially increase the spin diffusion length to 380nm±130nm.

4.1 Spin valve and spin transistor based on ferromagnet/semiconductor hybrid structures

Spintronic devices based on ferromagnet/semiconductor hybrid structures offer great potential for integrating additional functionalities with conventional semiconductor electronics.[125] And spin injection, detection and manipulation are among the fundamental challenges for an all-spin logic realization.

In all-electrical spintronic devices, the spin valve and spin transistor are the most commonly used prototypes. The spin valve concept has been demonstrated most prominently in giant magnetoresistance devices, in which the spin valve superlattices work as sensors for reading local magnetic fields.[126] In addition to the practical application as a data storage unit, the spin valve and its extensions are also widely used to study the basic properties of spin diffusion inside metals[127, 128] and semiconductors.[129] In Section 4.4, we demonstrate a set of mesoscopic lateral spin valves, consisting of two ferromagnet contacts and InAs surface electron layers, as shown in Figure 4.1 (a). Another widely studied spintronic device is a spin field effect transistor, which has geometry similar to a metal-insulator-semiconductor field effect

transistor and can be modulated by the gate voltage via spin-orbit interaction, as shown in Figure 1. (b).

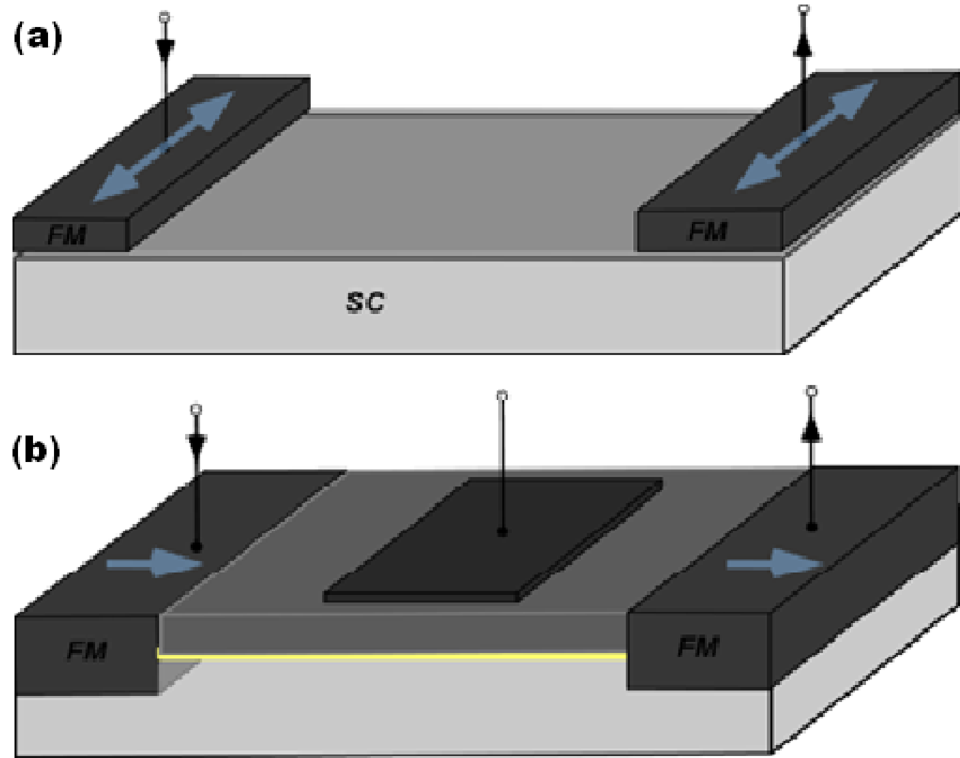

Figure 4.1: (a) Schematic of a spin valve, with two contacts magnetized perpendicular to the transport direction of the spin-polarized electrons. (b) Schematic of a spin transistor, with a gate contact and two ferromagnet contacts parallel to the transport direction of the spin-polarized electrons.

4.2 Characterization of spin injection barrier into InAs

4.2.1 Preparation of InAs surface for spin injection

Normal semiconductors do not have an intrinsic spin polarization. To break the equilibrium of spin up/down electron population, electrical spin injection from a ferromagnetic contact or spin injection via optical pumping are widely used to generate a net spin polarization. Spin injection is the first prerequisite of successful realization of many spintronic devices discussed in Section 4.1. To overcome the conductivity mismatch issue between ferromanget and semiconductor,[130] a tunneling or Schottky barrier between the two materials is introduced. In addition, abrupt and clean interfaces, preserving spin polarization through them, are essential to efficient spin injection. Therefore, most spin injection investigations require molecular beam grown structures and in situ treatments on interfaces.[131]

In this chapter, to prepare InAs surface for spin injection, several types of surface treatments are investigated. An ex situ sulfur-based chemical treatment is employed before Al_2O_3 deposition. For the first type, InAs wafer is cleaned with acetone and isopropanol with ultrasonic agitation for 3 min each. This was assumed to result in an interface with the Co and InAs layers separated by the native oxide formed on the InAs surface.[132] This is included as type (a) InAs surface in Table 4.1. For the second type, the InAs surface was first cleaned in organic solvents as above and then soaked for 15min at 25°C in 7% $(NH_4)_2S$ in which extra sulfur was dissolved to form a sulfur-saturated solution. This latter process has been shown previously to result in

removal of the native oxide and formation of In-S bonds at the InAs surface.[132] Approximately 3nm of Al_2O_3 was then deposited by rf sputtering on the cleaned InAs surface. This three-step process forms the type (b) treatment in Table 4.1. For type (c) surface treatment, after degreasing and sulfuration process as described in type (b) treatment, the Al_2O_3 layer is developed by oxidizing thin Al layer instead of direct rf sputtering. For type (d) surface treatment, after degreasing and sulfuration process as described in type (b) treatment, the treated InAs is loaded in vacuum chamber and reoxided with flowing pure O_2.

Table 4.1: Details of surface treatments implemented on InAs

Surface treatment type	Details
Type (a)	Degreased with acetone and isopropanol, original oxide.
Type (b)	Degreased, sulfurated, and covered with sputtered Al_2O_3.
Type (c)	Degreased, sulfurated, and covered with oxidized Al.
Type (d)	Degreased, sulfurated, and reoxided in flowing O_2.

4.2.2 Conductive atomic force microscopy of tunnel barriers on treated InAs surfaces

Conductive atomic force microscopy (CAFM) was used to characterize the electrical conductivity through the native oxide and Al_2O_3 layers, which is relevant to the discussion and analysis of spin injection efficiency through the InAs native oxide

and that through the deposited Al2O3 layer. Figure shows AFM topographs and conductive AFM images of local current flow through the InAs native oxide present after cleaning in acetone and isopropanol, i.e., InAs treated by type (a) surface treatment in Table 4.1, and through a 3nm Al_2O_3 layer sputtered onto a sulfur-treated InAs surface as described above, i.e., type (b) surface treatment in Table 4.1. Tunnel barriers after type (c) and type (d) surface treatment show higher surface roughness in topography.

The topographic and conductive AFM images were obtained simultaneously in each case, with a bias voltage of 1V applied to the sample relative to a conductive probe tip. The grey scale in each conductive AFM image corresponds to a range of 0 to 1nA. We see in Figure (a) that the native oxide suffers from highly localized current leakage through the oxide at several points. In contrast, no current leakage is observed through the 3nm Al_2O_3 film into the underlying InAs layer, for bias voltages as high as 5V. Given the established significance of a tunnel barrier in enabling injection of spin-polarized current from a ferromagnetic contact into a semiconductor,[130] the prominent spin polarization in a semiconductor can't be achieved through low-resitance interfaces, while for a nanoscale spin valve with the InAs native oxide, the current density exponentially increases at the pinhole-like leakage centers in the native oxide, as shown in Figure 4.2 (a). The ferromagnet-semiconductor spin injection efficiency depends strongly on the presence of an electrically insulating barrier to mitigate the effects of conductivity mismatch between a metal and semiconductor in suppressing spin-polarized electron injection. The

conductive AFM measurements clearly reveal the imperfect nature of the InAs native oxide, compared to the Al_2O_3 deposited layer, as a barrier to electrical conduction, and are thus relevant to the observation of negligible spin polarized current injection through the native oxide, and easily observed spin polarized current injection through the Al_2O_3 layer. Furthermore, the localized nature of conduction observed by conductive AFM across the InAs native oxide layer makes this interpretation very sensible, as the pinhole-like leakage observed through the InAs native oxide will dominate electrical conduction, making the electrical contact across that oxide look similar to a low-resistivity contact with reduced area, through which spin-polarized current injection efficiency would be expected to be very low with the spin-polarized current through the tunneling barrier overwhelmed by the unpolarized current. The spin-dependent signal of the spin valve device is then largely suppressed. The presence of the Al_2O_3 layer at the Co-InAs interface avoids the leakage problem in the native oxide and contributes to the measurable spin-dependent signals in the spin valve device. We also note the tunnel barriers after type (c) surface treatment exhibits local electrical properties similar to the barriers after type (b) treatment, with higher surface roughness in topography. The reoxidized layer after type (d) surface treatment exhibits pinhole-like features similar to type (a) InAs, which proves that gradual oxidation in flowing pure oxygen is not effective in providing uniform spin injection barriers, or avoiding pinhole induced leakage current.

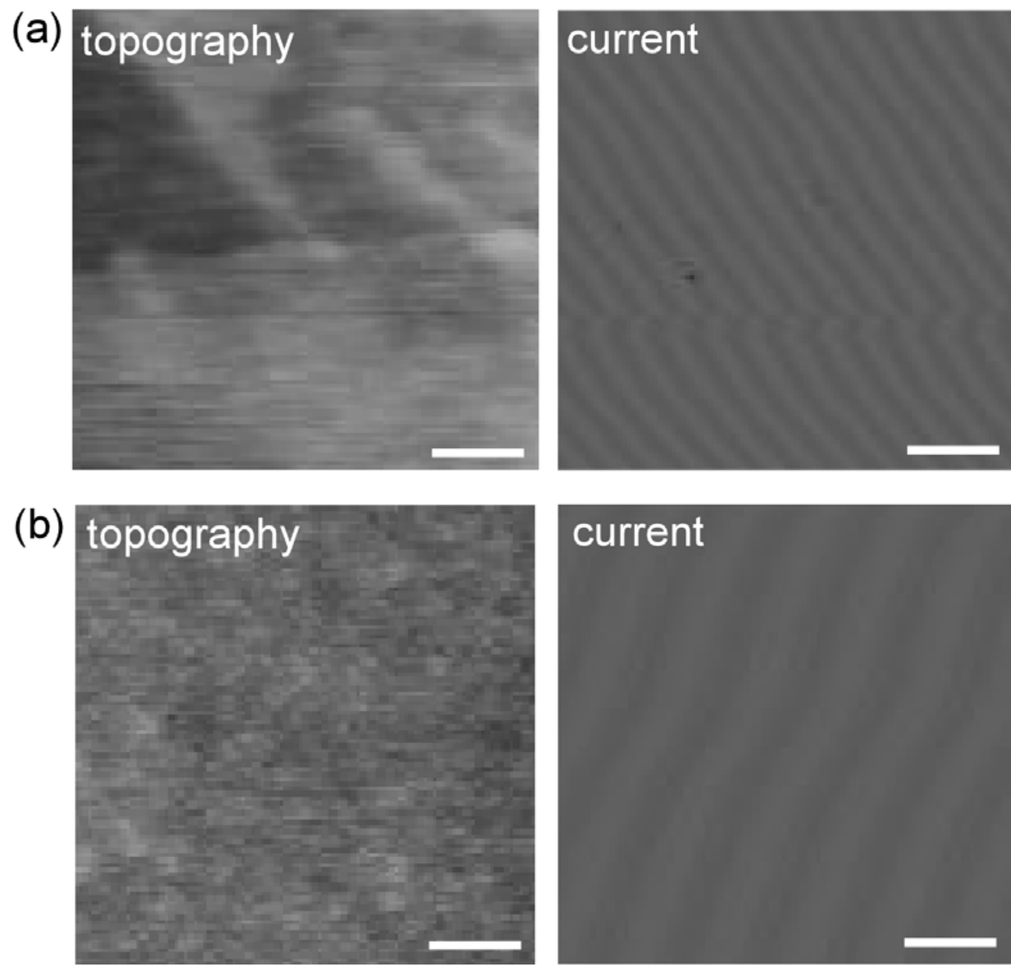

Figure 4.2: Topographic and conductive atomic force microscope images, obtained simultaneously in each case with 1V bias applied to the sample, of (a) p-type InAs with native oxide layer, and (b) p-type InAs on which a 3nm Al_2O_3 layer has been deposited by sputtering. All scale bars are 200nm. Grey scales correspond to 5nm for topography, 1nA for current.

4.3 Micromagnetic behavior of magnetic contacts for spin injection into semiconductor

Although both theoretical and experimental approaches have been developed to estimate the magnetic behaviors of magnets with submicron size, the uniqueness of different sputtered magnetic thin films still makes the magnetic properties of an arbitrary micromagnet ambiguous. The submicron magnets show complex magnetization configuration, such as typical Landau patterns,[133] divided domains,[134] while the single-domain micromagnet magnetized in one direction is required to maximize the overall spin polarization of the injected carriers. Therefore, to confirm the magnetization of the two Co contacts constituting the spin valve structure and its relevance to these observed shifts in magnetoresistance of the spin valve, MFM measurements were performed as a function of externally applied magnetic field at ambient temperature on Co contact structures identical to those employed in the resistance measurements.

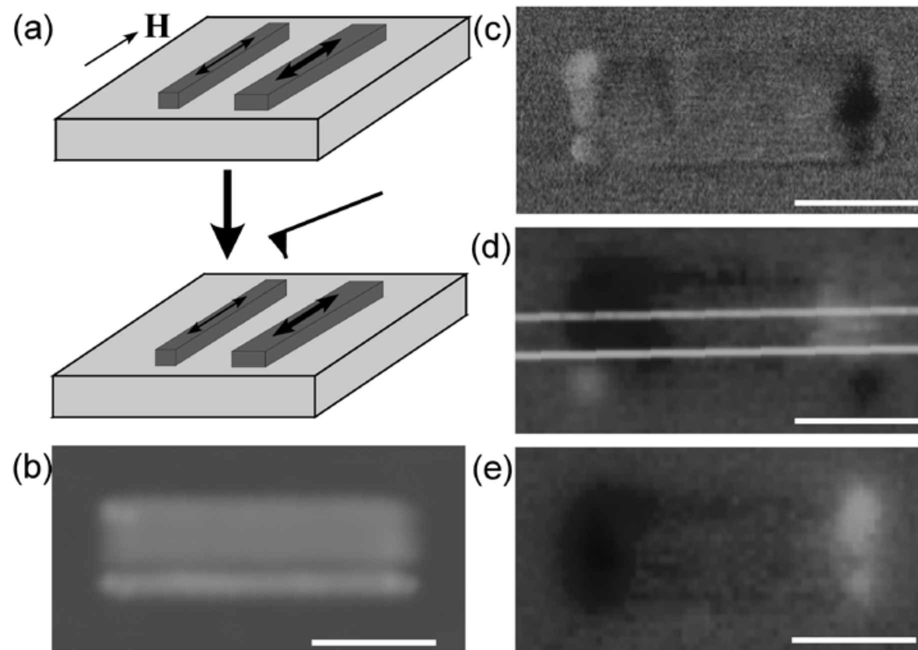

Figure 4.3: (a) Schematic diagram of measurement process for atomic and magnetic force microscopy of Co ferromagnetic contacts for spin-valve device. (b) Topographic image of Co contacts, and (c)-(e) magnetic force images of Co contacts after application of external magnetic fields of 300Oe, 600Oe, and 1200Oe, respectively. The magnetic force images show the transition from parallel magnetization, in (c), to antiparallel magnetization, in (d), and back to parallel magnetization, in (e), in the opposite direction to that in (c). All scale bars are 500nm. Grey scale corresponds to 300nm in topographic image.

The measurement scheme is indicated in Figure 4.3 (a), where MFM images are immediately scanned on Co contacts after they are configurated by varying external magnetization fields. Figure 4.3(b) shows an AFM topographic image of the Co contact structures, and Figure 4.3 (c)-(e) shows MFM images after application of external magnetic fields of 300Oe, 600Oe, and 1200Oe. The figure reveals a clear transition from parallel magnetization, in Figure 4.3 (c), to antiparallel magnetization, in Figure 4.3 (d), at 600Oe, and back to parallel magnetization, but in the opposite direction, in Figure 4.3 (e), at 1200Oe. The magnetic fields at which spin-dependent changes in resistance are observed in the low-temperature device measurements shown in Figure 4.5 are somewhat larger, which is as expected based on the known temperature dependence of the coercivity of Co thin films.[135]

4.4 Magnetoresistance measurements in the local spin-valve geometry

The electrical resistance of spin-valve structures fabricated with Al_2O_3 interface layers on p-type InAs was measured at 4.2K as a function of external magnetic field applied along the width of the Co contacts, as shown in Figure 4.4. The most delicate step in the device fabrication process is to introduce an abrupt and clean tunnel barrier between Co terminals and the InAs channel. As discussed in Section 4.2, an Al_2O_3 layer by rf sputtering on $(NH_4)S_x$ treated InAs surface satisfies this requirement. Section 4.3 demonstrates the uniformity of the nanoscale ferromagnetic

structures, which excludes the possibility of the local Hall effect due to fringe fields from ferromagnetic electrodes.

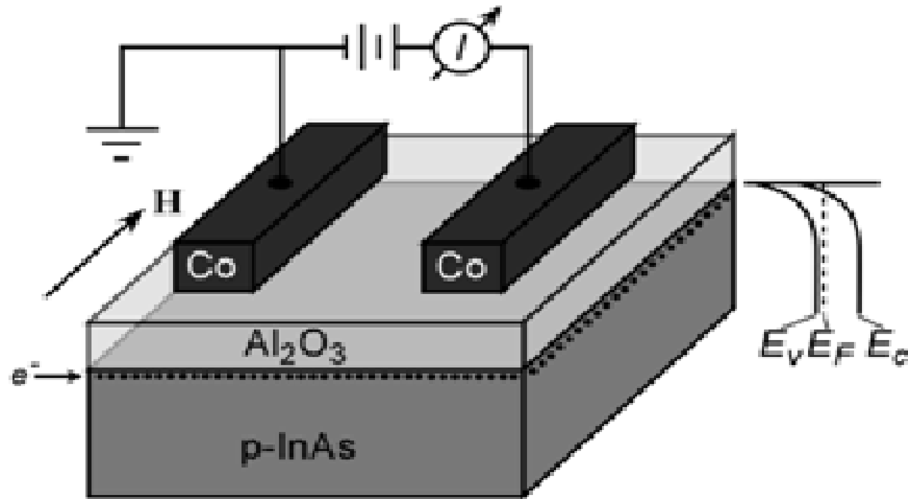

Figure 4.4: Schematic diagram of spin-valve device structure as fabricated on p-type InAs, magnetoresistance measurement configuration, and InAs electronic structure.

No measurable magnetoresistance was observed for spin valve devices fabricated with Co contacts deposited directly on as-cleaned or sulfur-passivated p-InAs surfaces. For spin valve devices fabricated with Al_2O_3 interfacial layers separating the Co contacts from the p-InAs surface, the magnetoresistance *MR* is defined as

$$MR \equiv \frac{\Delta R}{R^{\uparrow\uparrow}}, \tag{4.1}$$

where $R^{\uparrow\uparrow}$ is the average spin-valve resistance for contacts with parallel magnetization over the entire range of applied magnetic fields, and ΔR is the deviation of the resistance from $R^{\uparrow\uparrow}$. *MR* measured as a function of external applied magnetic field is plotted in Figure 4.5.

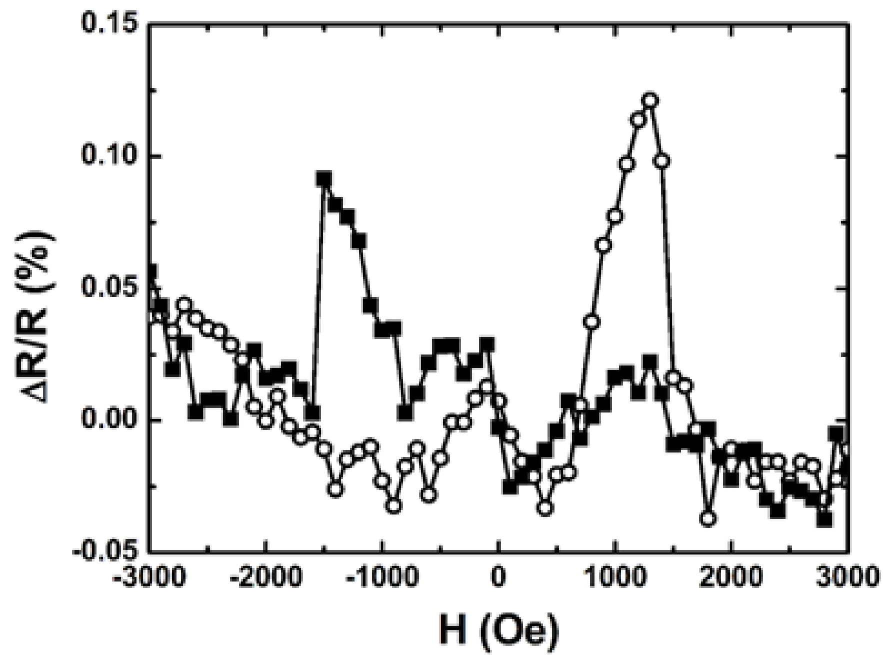

Figure 4.5: Magnetoresistance measured for spin-valve device structure shown in Figure 4.4, for field sweep directions from – to + (open circles) and + to – (solid squares).

The key features of interest are the sharp changes in resistance that occur for applied fields in the vicinity of ±1000Oe. These shifts correspond to changes in

resistance of 0.12% when the field is swept in the forward (– to +) direction, and 0.09% when the field is swept in the reverse (+ to –) direction. Figure 4.6 shows the measured resistance change, on a logarithmic scale, as a function of channel length, i.e., separation between the Co contacts in the direction of carrier transport, in several spin-valve structures. The magnetoresistance is seen to vary exponentially with channel length, as expected for spin-dependent electron transport within a semiconductor channel. Specifically, the magnetoresistance is expected to be given by[136]

$$MR \equiv \frac{\Delta R}{R^{\uparrow\uparrow}} = \frac{\gamma^2}{1-\gamma^2} e^{-l_c/l_{sf}}, \qquad (4.2)$$

where γ is the spin polarization of the current injected from the Co contact into the semiconductor, l_c is the spin valve channel length, and l_{sf} is the spin diffusion length in the semiconductor channel.Analysis of the data in Figure (b) using the functional dependence given in Eqn. (2) yields a spin diffusion length l_{sf} of 380nm±130nm, and a spin injection efficiency γ of ~1.4±0.2% at 4.2K.

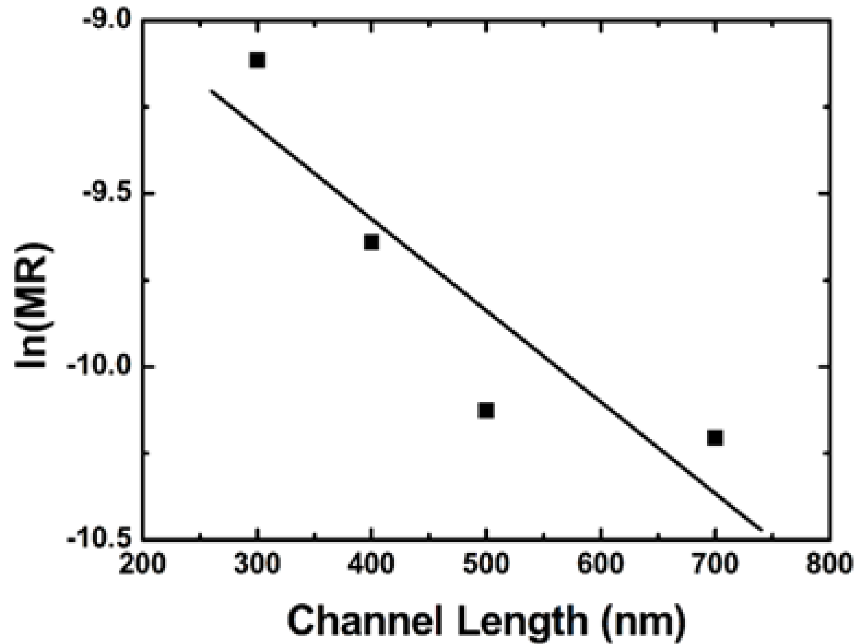

Figure 4.6: Maximum measured magnetoresistance as a function of spin-valve channel length (filled squares), along with line fitted according to Eqn. (4.2) from which the spin injection efficiency and spin diffusion length are determined.

4. 5 Conclusions

We have used spin-valve electrical measurements and analysis, and scanned probe microscopy to assess the influence of interfacial layers and surface treatments on spin-polarized current injection from Co contacts into p-type InAs, and spin-polarized electron transport within the two-dimensional electron layer at the InAs surface. The presence of an electrically insulating tunnel barrier at the interface between the Co contact and InAs surface was found to be essential to observation of

nonzero spin injection efficiency, with a 3nm Al_2O_3 interface barrier yielding a spin injection efficiency of ~1.4%. Spin-valve measurements at 4.2K yielded consistent spin scattering lengths in the range of ~380nm. These measurements provide better understanding of prerequisite for spin injection for the surface electron layer in InAs and the transport processes of spin-polarized current inside InAs.

Acknowledgments: This chapter, in full, has been submitted for publication of the material as it may appear in the Journal of Applied Physics, 2009. Zhu, Lei; Yu, Edward T., "Influence of surface treatment and interface layers on electrical spin injection efficiency and transport in InAs", AIP Publishing, 2009. The dissertation author was the primary investigator and author of this paper.

Reference

---

[125] I. Zutic, J. Fabian, and S. Das Sarma, *Rev. Mod. Phys.* **76**, 323 (2004).

[126] M. N. Baibich, J. M. Broto, A. Fert, F. Nguyen Van Dau, F. Petroff, P. Etienne, G. Creuzet, A. Friederich, and J. Chazelas, *Phys. Rev. Lett.* **61**, 2472 (1988)

[127] F. J. Jedema, H. B. Heersche, A. T. Filip, J. J. A. Baselmans, and B. J. van Wees, *Nature* **416**, 713 (2002).

[128] Y. Ji, A. Hoffmann, J. E. Pearson, and S. D. Bader, *Appl. Phys. Lett.* **88**, 052509 (2006).

[129] H. C. Koo, H. Yi, J.-B. Ko, J. Chang, S.-H. Han, D. Jung, S.-G. Huh, and J. Eom, *Appl. Phys. Lett.* **90**, 022101 (2007).

[130] G. Schmidt, D. Ferrand, L. W. Molenkamp, A. T. Filip, and B. J. van Wees, *Phys. Rev. B* **62**, R4790 (2000).

[131] B.T. Jonker, S.C. Erwin, A. Petrou and A.G. Petukhov, *MRS Bulletin*, **740**, October 2003.

[132] D. Y. Petrovykh, M. J. Yang and L. J. Whitman, *Surf. Sci.* **523**, 231 (2003).

[133] G. Meier and T. Matsuyama, *Appl. Phys. Lett.* **76**, 1315 (2000).

[134] D. A. Allwood, G. Xiong, C. C. Faulkner, D. Atkinson, D. Petit, and R. P. Cowburn, *Science* **309**, 1688 (2005).

[135] J. P. Lazzari, I. Melnicr and D. Randet , *IEEE Trans. Magn.* **3**, 705 (1967).

[136] A. Fert, J.-M. George, H. Jaffrès, and R. Mattana, *IEEE Trans. Elec. Dev.* **54**, 921 (2007).

Chapter 5

Ballistic transport and electrical spin signal amplification in a three-terminal spintronic device

Information processing based on manipulation of electron spin, rather than charge, transport in semiconductors offers the promise of dramatic advances in speed, power consumption, and functionality of solid-state electronic devices.[137] However, challenges abound in the attainment of highly efficient electrical injection of spin-polarized electrons into a semiconductor, robust manipulation and detection of electron spin, and realization of electrical device concepts readily scalable to nanoscale dimensions.[138, 139] Here we report demonstration and analysis of a three-terminal, all-electrical spintronic switching device in which a combination of charge current cancellation by appropriate device biasing and ballistic electron transport within the device yields a robust, electrically amplified spin-dependent current signal

despite modest efficiency in electrical injection of spin-polarized electrons. Detailed analyses provide insight into the advantages of ballistic, as opposed to diffusive, transport in device operation, as well as scalability to smaller dimensions, and allow us to eliminate the possibility of phenomena unrelated to spin transport contributing to the observed device functionality.

5.1 Amplification of a spin-polarized current

A transistor, as a fundamental unit of semiconductor circuits, offer the capability to modulate the large drain current flow by a small change of current or potential at the control terminal. Among fundamental spintronic devices, a device providing similar functions has been pursued consistently. In addition to the all-electrical operation in conventional semiconductor devices, the configuration of magnetic contacts in a spintronic device is eventually able to work as an extra terminal, and thus, employ supplementary functions. For instance, the spin field effect transistor (SpinFET), which makes use of the Rashba effect, provides gain of current carriers during the operation. Similar to the conventional junction field effect transistor (J-FET), however, the amplifier capability of a SpinFET still only applies to the charge amount instead of spin polarization.

Therefore, it would be highly desirable to develop the elusive 'spin polarization' amplifier, as a prerequisite for spintronic circuits. With such a circuit element, not only the injected spin polarization, but also the preservation of spin

polarization could be dramatically improved. A spin amplifier needs to sense the polarization of the input current I_s^{in}, where $I_s^{in} = I_\uparrow^{in} - I_\downarrow^{in} = P_s^{in} I_c^{in}$, P_s^{in} is the input spin polarization, and I_c^{in} is the total charge current. Thus, we can define 'spin current' gain as $g_s^{(1)} = I_s^{out}/I_s^{in}$ and 'spin polarization' gain as $g_s^{(2)} = P_s^{out}/P_s^{in}$. The amplifier, as shown as a black box in Figure 5.1, has been conceptually constructed and experimentally achieved with limited applications. For example, with novel design of electronic devices, a T-shaped current branching semiconductor device is used to decouple charge current and spin current, and thus, improve spin polarization,[140] and a multi-terminal device with quantum dots as functional parts is also utilized to exploit quantum calculation by Coulomb blockade effects.[141]

In another approach, micromagnet reconfiguration can also lead the way to spin amplification. An elliptical ferromagnetic layer,[142] as a spin detector at first, can be triggered by low spin polarized current, broken into the bifurcation point, and relax into static configuration with larger magnetization. In the new magnetic configuration, the elliptical ferromagnetic layer acts as a spin generator with higher spin polarization than the initial injected current. Another example with magnetic reconfiguration is a ferromagnet just above its Curie temperature.[143] Its moment may be induced to align into a certain magnetization direction with the charged Curie temperature by the incident current with lower spin polarization.

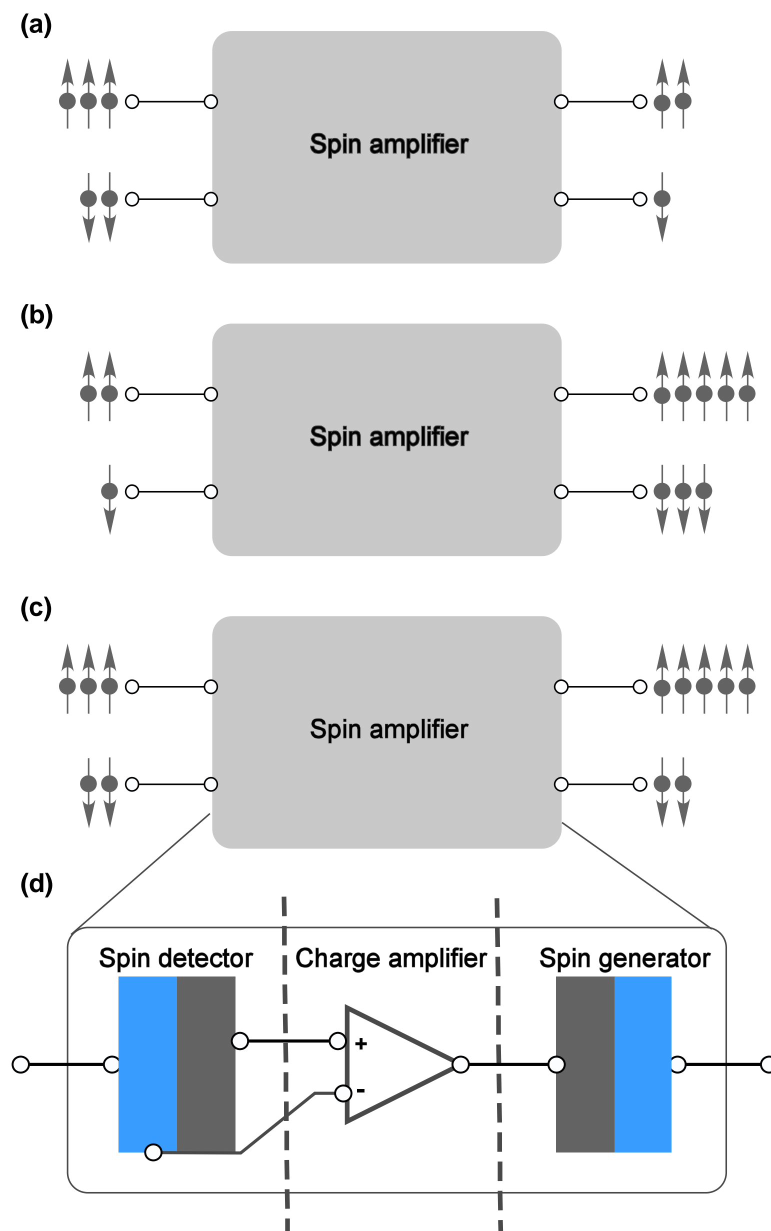

Figure 5.1: (a) spin amplifier with $g_s^{(1)} < 1$ and $g_s^{(2)} > 1$. (b) spin amplifier with $g_s^{(1)} > 1$ and $g_s^{(2)} < 1$. (c) spin amplifier with $g_s^{(1)} > 1$ and $g_s^{(2)} > 1$. (d) a conceptual spin amplifier with three components.

Combined with the device providing spin polarized input, such as a spin valve, the amplifier can be transformed into a multi-drain spin valve, with magnetoresistance amplification capability, as first introduced by Dery, Cywinski, and Sham[144] and realized by Saha, Holub, and Bhattacharya.[145] In the following sections, we will demonstrate an amplifier with a similar geometry, but different spin transport mechanism that enables improved performance and robust scalability to nanoscale dimension.

5.2 Multi-terminal spin transistor based on InAs

The basic device structure employed is shown in Figure 5.2. Three ferromagnetic contacts are fabricated on a p-type InAs semiconductor surface, enabling electrical injection of a partially spin-polarized electron current into the two-dimensional electron inversion layer formed at the InAs surface.[146] Current modulation via one terminal combined with ballistic transport at dimensions comparable to or smaller than the elastic scattering length is exploited to attain large magnetoresistance, and consequently a large on/off current switching ratio, in current flow between the remaining two device terminals. Devices based on spin-polarized injection of electrons into InAs have been explored previously,[147, 148] but with limited success in realization of spin-dependent current modulation. Indeed, numerous ferromagnet/semiconductor hybrid electrical devices have been designed and experimentally demonstrated,[149, 150, 151, 152] but generally with performance limitations

imposed by the low efficiency of spin injection and extraction and strict requirements for retention of spin polarization within the semiconductor.[138] Multi-terminal electrical device structures have also been proposed[142, 143, 144] and investigated experimentally,[145] based on operation in the diffusive regime of electron transport within the semiconductor. For the device shown in Figure 5.2, the physical dimensions are such that electron transport between adjacent contacts is ballistic rather than diffusive, leading to fundamental differences in device behavior, an increase in spin dependence of current flow, and improved scalability to smaller dimensions.

The basic operational concept for the device shown in Figure 5.2 is as follows. Bias voltages V_L, V_C, and V_R are applied to the three device terminals, and charge currents flowing at the left and right terminals, I_L and I_R, respectively, are monitored. These currents are dependent on the magnetization state of the contacts, due to the differing contact resistances for each electron spin channel and the presence of spin-dependent electron transport in the InAs channel between the contacts. By application of appropriate bias voltages, the charge current I_L can be made to vanish for a particular contact magnetization state, e.g., the left contact magnetization antiparallel to those of the center and right contacts. If the magnetization of the left contact is then reversed, yielding a configuration in which all contacts have parallel magnetization, I_L will then be nonzero and a large magnetoresistance, $MR = (I_L^P - I_L^{AP}) / I_L^{AP}$, and consequently a large on/off current switching ratio for the device, can be achieved.

Key to efficient operation of this device, and in particular to a robust spin-dependent switching signal even with limited efficiency in injection of spin-polarized

electrons into the semiconductor channel, is scaling of the device to dimensions at which electron transport between adjacent contacts is largely ballistic, rather than diffusive. Hall measurements on the p-InAs surface electron layer yield a mobility of ~6000 $cm^2/V \cdot s$ and an electron sheet concentration of ~1×10^{12} cm^{-2}, while results of weak localization/anti-localization measurements at 4.2 K yield a spin diffusion length for surface-layer electrons of ~300 nm and an elastic scattering length of ~60-90 nm. As shown in Figure 5.2 (b), the ferromagnetic Co contacts in the device shown have lengths (in the direction of current transport) of 120 nm, 230 nm, and 230 nm, and widths (in the direction perpendicular to transport) of 1000 nm each. The separation between the edges of adjacent contacts is ~70 nm, comparable to the elastic scattering length, and therefore enabling ballistic electron transport between these contacts.

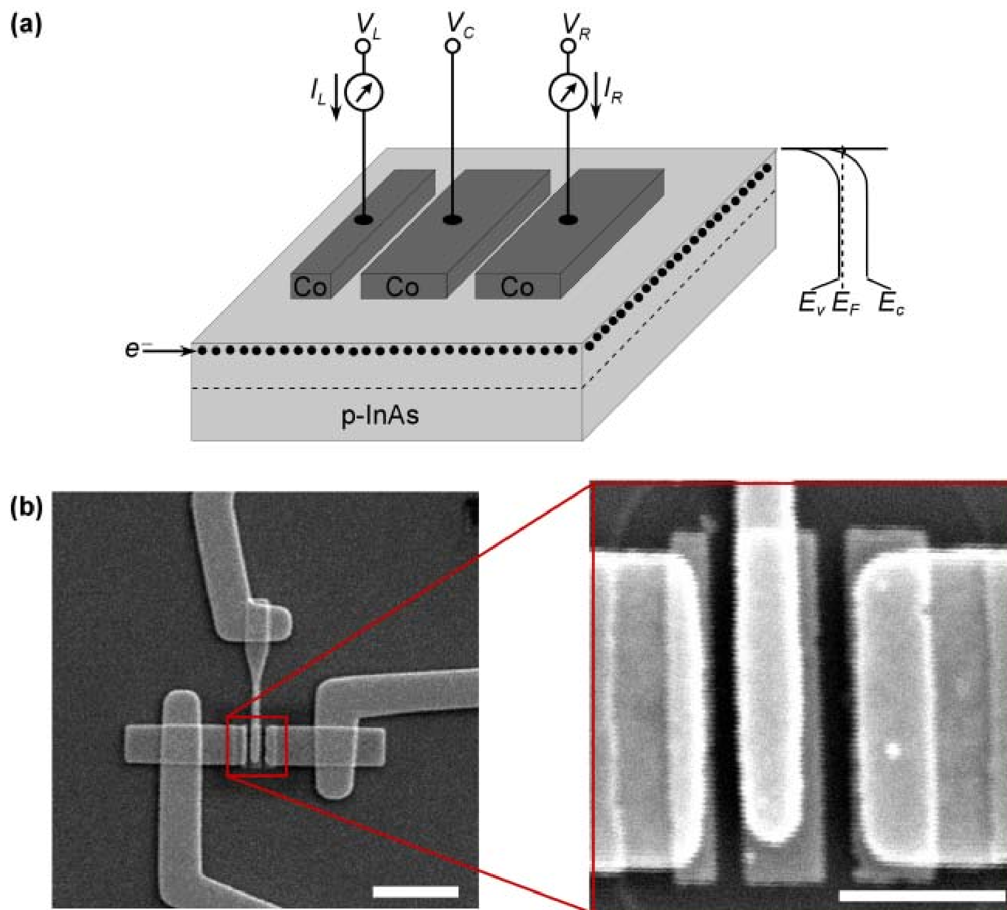

Figure 5.2: (a) Schematic diagram of three-terminal device geometry and measurement configuration. (b) SEM image of device with Co contacts and Au leads on p-InAs; magnified view shows geometry and dimensions of the three Co contacts. Scale bars are 2µm (left) and 500nm (right).

The devices are fabricated by standard e-beam lithography on p-type InAs wafers. An insulated surface electron layer is provided by lightly doped InAs at the temperatures below 77K. After passivating the InAs surface by ammonium sulfide, a layer of Al_2O_3 with ~3 nm thickness is sputtered deposited by a Denton Discover 18 sputter system, followed by deposition of Cobalt terminals using e-beam evaporation under a vacuum of ~ 2×10^{-7} Torr. External magnetic fields are applied during deposition to keep the easy axis of the magnetic thin film in plane and along the long axis of the rectangular terminals. The squareness of the hysteresis loop of a Cobalt thin film deposited by this method is revealed to be 95% when measured by alternating gradient magnetometer (AGM) at room temperature and remains similar at liquid helium temperature. The single domain configuration of each Cobalt terminal is confirmed by magnetic force microscopy (MFM), based on a Nanoscope III Multi Mode scanning probe microscope from Digital Instruments. Keithley 2400 SourceMeters and an HP 4156 Precision Semiconductor Parameter Analyzer were used for electrical measurements, which were performed with the sample mounted in a cryostat with flowing liquid helium.

5.3 Magnetic configuration of multi-stripe nanomagnet Structure

To confirm that each Co contact has single-domain magnetization along the long axis of the contact, and that the coercive fields for magnetization reversal are

different for contacts of different lengths, due to shape anisotropy effects, we have used magnetic force microscopy to measure the magnetization as a function of external applied magnetic field, as shown in Figure 5.3. As indicated in Figure 5.3 (a), an external magnetic field is applied to the sample along the long axes of the contacts, and then magnetic force microscope images are obtained at room temperature with no external field applied. Single-domain magnetization of each Co contact is evident in Figure 5.3 (c)-(f), with a transition in magnetization from an all-parallel configuration at external fields up to 400 Oe (Figure 5.3 (c)-(d)), to an antiparallel configuration at 600 Oe external field (Figure 5.3 (e)), and back to a parallel configuration, but with magnetization in the opposite direction, at 800 Oe (Figure 5.3 (f)). The magnetic fields at which spin-dependent transitions in device behavior induced by changes in contact magnetization are observed are somewhat larger, in the range of 1500 – 2000 Oe; this can be understood on the basis of the temperature dependence of the coercivity of Cobalt thin films.[153]

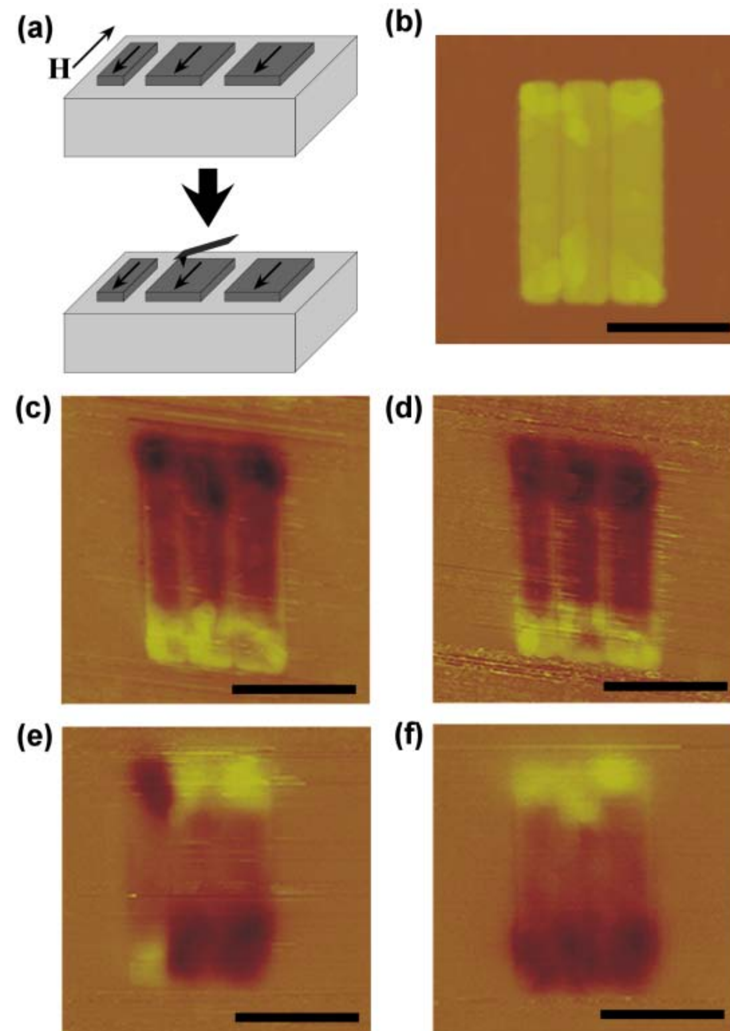

Figure 5.3: (a) Schematic diagram of MFM measurement process: an external magnetic field is applied to control the magnetization of the Co contacts, and subsequently MFM measurements are performed to assess directly the contact magnetization as a function of external field. (b) AFM topographic and (c)-(f) MFM images of the Co contacts following application of successively larger external fields, showing the transition from an all-parallel magnetization configuration (c)-(d) to an antiparallel configuration (e) and back to an all-parallel configuration (f). All scale bars are 1μm.

5.4 Magnetoresistance amplification in multi-terminal spin transistor

5.4.1 Measurement scheme of magnetoresistance in a spin transistor

In our measurements, the current I_L is monitored, with scanning bias voltages V_L and V_R. For a given magnetization configuration of three terminals, the curved surface of $I_L(V_L, V_R)$ function is determined by Kirchoff law, without involving spin dynamics. Once the magnetization configuration is changed, the spin-selective circuit networks would be reconnected. Therefore, a new curved surface of $I_L(V_L, V_R)$ function forms after the magnetization reconfiguration.

The current I_L, measured as a function of bias voltages V_L and V_R, with V_C=0, for a representative three-terminal device with parallel magnetization for all three Co contacts is shown in Figure 5.4 (a). As expected from the device geometry, there exists a locus of points (V_L,V_R) for which I_L=0. When an external magnetic field is applied to reverse the magnetization of the two larger contacts, the curve $I_L(V_L,V_R)$, and consequently the locus of points for which I_L=0, shifts, as shown in Figure 5.4 (b). Selection of an operating point at which I_L=0 for a specific magnetization configuration thus allows a large magnetoresistance to be realized when the contact magnetization is changed, as illustrated schematically in Figure 5.4 (b).

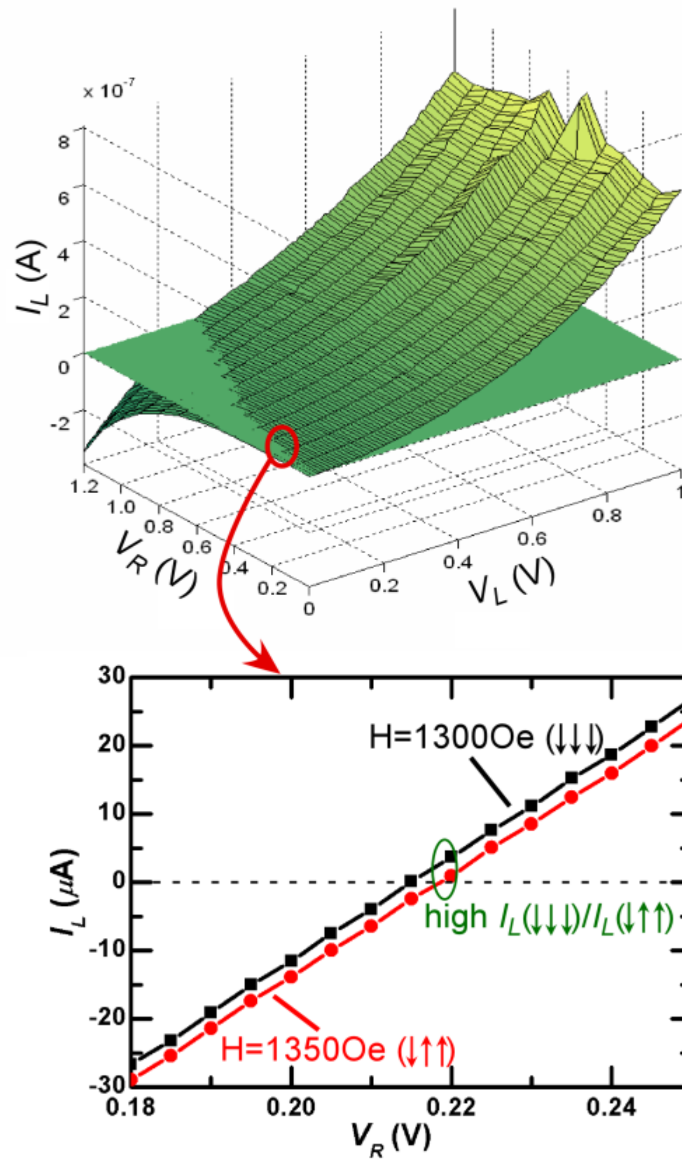

Figure 5.4: (a) Plot of current I_L as a function of voltages V_R and V_L, with $V_C = 0$. A locus of points in the (V_R,V_L)-plane corresponding to I_L=0 is clearly evident. (b) Shift in I_L due to alterations in spin injection and transport upon application of an external magnetic field that changes the magnetization configuration of the Co contacts. For operation near a point at which I_L(↓↑↑)=0, a large on/off current switching ratio can be attained.

Figure 5.5 demonstrates this concept. The measured charge current I_L is shown for V_L=0.220 V, V_C=0, and V_R=1.000 V as a function of externally applied magnetic field, for external fields swept from –3000 Oe to +3000 Oe (open circles) and +3000 Oe to –3000 Oe (filled squares). For each sweep, the Co contact magnetizations are initially parallel; at fields in the vicinity of +1500 Oe (– to + sweep) or –2000 Oe (+ to – sweep) the magnetizations of the two larger contacts are reversed, leading to a magnetization configuration in which the left contact is antiparallel to the center and right contacts, and the current I_L drops substantially. As the external field sweep is continued, the magnetization of the third contact is also reversed, leading to a parallel contact magnetization configuration and larger current I_L. In addition, I_L has an overall decreasing contour with increasing magnetic field perpendicular to electron transport. This gradual current change is due to the anisotropic magneto-resistance (AMR) effect, which is proportional to the initial current at zero magnetic field,[154] and implies the coexistence of substantial injection and extraction currents in the left terminal that largely cancel out to yield the final measured current I_L.

The magnetoresistance *MR*, defined as $MR \equiv \left(I_L^P - I_L^{AP}\right)/I_L^{AP}$ with $I_L^P \equiv I_L^{\downarrow\downarrow\downarrow}$, $I_L^{AP} \equiv I_L^{\downarrow\uparrow\uparrow}$ and the arrow superscripts for I_L indicating the magnetization state of the three contacts (left, center, right), directly measured in this manner is 212% for the – to + sweep and 328% for the + to – sweep. If the current-voltage characteristics are interpolated to estimate the minimum value of I_L as limited by noise and measurement

uncertainty in our system, the maximum magnetoresistance value is approximately 1,800%.

5.4.2 Magnetoreistance amplification mechanism: a spin-diffusion analysis

Following a procedure similar to that employed for spin valve devices, [155] a spin diffusion model can be applied to estimate the spin-dependent signal in our multi-terminal spin transistor structure. To simplify the calculation, we excludes the effects of device geometry by assuming that magnetic terminals and InAs channels form ideal dot contacts and channel lengths are estimated as center-to-center distances of adjacent terminals. Since such calculations without considering the geometry of spin valves will actually overestimate magnetoresistance,[156] this assumption doesn't influence our purpose of estimating the maximum of spin-dependent signal predicted by a spin diffusion model. We also assume that the left terminal is a floating gate since the charge current through the left terminal is zero in all circumstances and the spin currents from both up/down channels compensate each other for the antiparallel magnetization configuration. Therefore, the change in current at the left terminal that occurs upon changing the contact magnetization from the parallel to antiparallel configuration is the nonzero total current from both spin up/down channels at the left terminal for the parallel magnetization configuration.

For this parallel configuration, the center and right terminals form a local spin valve. The simplified 1D transport is governed by the spin diffusion equation,

$$\nabla^2 \mu_{\pm}(x) = \frac{\mu_{\pm}(x) - \mu_{\mp}(x)}{L_{sf}^{\;2}}. \tag{5.1}$$

The electrochemical potential of the spin up/down channel, $\mu_{\pm}(x)$,[161] is

$$\mu_{\pm}(x) = \mu_0 + \frac{j_0 e}{\sigma_n} \cdot x \pm (p \cdot \exp(-x/L_{sf}) + q \cdot \exp(x/L_{sf})). \tag{5.2}$$

Combined with boundary conditions at the center and right terminals,[157] the splitting of the electrochemical potential at the center terminal is

$$\delta\mu(C) = 2 j_0 e \gamma \rho_N^* L_{sf} \tanh(\frac{L_{RC}}{2L_{sf}}) \ , \tag{5.3}$$

where γ, ρ_N^*, and L_{sf} are the spin asymmetry at the contact interface, the resistivity of the semiconductor channel and the spin diffusion length inside the semiconductor channel, respectively.

This spin splitting of the electrochemical potential will decay exponentially from the center terminal to the left terminal without charge currents flowing through them. Thus, at the left terminal, the electrochemical potential splitting is

$$\delta\mu(L) = \delta\mu(C) = 2 j_0 e \gamma \rho_N^* L_{sf} \tanh(\frac{L_{RC}}{2L_{sf}}) \cdot e^{\left(-\frac{L_{LC}}{2L_{sf}}\right)}. \tag{5.4}$$

The spin up/down channels will be exchanged upon the magnetization reconfiguration, i.e., $\mu_{+}^{AP} = \mu_{-}^{P}$ and $\mu_{+}^{P} = \mu_{-}^{AP}$. When the magnetization is switched from antiparallel to parallel, the change of current at the spin-selective left contact is

$$\Delta I_{\mathbf{L}} = I_{L}^{P} - I_{L}^{AP} = \left(\mu_{+}^{AP} / er_{-} + \mu_{-}^{AP} / er_{+}\right) - \left(\mu_{+}^{P} / er_{+} + \mu_{-}^{P} / er_{-}\right) = \frac{\delta\mu(L)A}{r_c}\left(\frac{\gamma}{1-\gamma^{2}}\right), \quad (5.5)$$

where A is the contact area at the left terminal and the spin-selective contact resistance is given by $\mathbf{r}_{\pm} = 2(1 \pm \gamma) r_C$. Thus, the change on current detected at left terminal is

$$\Delta I_{\mathbf{L}} = \frac{I_0 \rho_N^{*} l_{sf}}{r_c} \tanh\left(\frac{L_{RC}}{2L_{sf}}\right) \cdot e^{\left(-\frac{L_{\mathbf{L}C}}{2L_{sf}}\right)} \cdot \left(\frac{\gamma^{2}}{1-\gamma^{2}}\right). \quad (5.6)$$

Prior measurements, described in Chapter 3 and Chapter 4, we have performed on spin-valve structures fabricated on p-type InAs yielded $L_{sf} = 380 \pm 130nm$ and $\gamma = 2 \pm 1\%$. Substituting $L_{sf} = 300nm$ and $\gamma = 3\%$ in the equations above, $\Delta I_{\mathbf{L}}$ is estimated to be $\sim 0.3\mu A$, which is almost one order of magnitude smaller than the observed value in our measurement. To match our measured results, the spin injection efficiency γ is required to be as high as 11%, which is several times larger than our best experimental value, implying that the spin diffusion model does not provide a good description of the behavior observed in our device structures.

5.4.3 Magnetoreistance amplification mechanism: a spin-polarized ballistic analysis

The observed electrical characteristics can also be understood quantitatively on the basis of an analysis of ballistic carrier transport within the device. A ballistic transport analysis is justified in this case as the distance between adjacent contacts is comparable to the elastic scattering length in the surface electron layer of p-type InAs, as determined from weak localization/antilocalization measurements. For this analysis, we apply the standard Landauer-Buttiker formula [158] for ballistic transport, modified to accommodate separate spin transport channels and reservoirs, to describe electron transport.[159] Including both spin up and spin down channels in all three terminals, the total charge current I_L is given by

$$I_L = \sum_{\alpha,\beta}(I_{LC}^{\alpha\beta} + I_{LR}^{\alpha\beta}) = \frac{e}{h}\sum_{\alpha,\beta}\int dE\{T_{LC}^{\alpha\beta}[f_L(E) - f_C(E)] + T_{LR}^{\alpha\beta}[f_L(E) - f_R(E)\} \quad , (5.7)$$

where $T_{LC}^{\alpha\beta}$ and $T_{LR}^{\alpha\beta}$ represent the transmission probabilities from spin channel α in the left terminal to spin channel β in the center terminal and the right terminal, respectively. $f_L(E)$, $f_C(E)$ and $f_R(E)$ refer to the Fermi distribution functions in the left, center, and right terminals.

Representing the transmission probabilities in Eqn. (5.7) by linear conductances $G_{LC}^{\alpha\beta}$ and $G_{LR}^{\alpha\beta}$, and assuming the low temperature limit for the Fermi distribution $f(E)$, we can simplify Eqn. (5.7) to the form

$$I_L = \sum_{\alpha,\beta} (G_{LC}^{\alpha\beta}(V_C - V_L) + G_{LR}^{\alpha\beta}(V_R - V_L)) \ , \qquad (5.8)$$

where $G_{LC}^{\alpha\beta} = \frac{e^2}{h} T_{LC}^{\alpha\beta}$, and $G_{LR}^{\alpha\beta} = \frac{e^2}{h} T_{LR}^{\alpha\beta}$. In $G_{LC}^{\alpha\beta}$ and $G_{LR}^{\alpha\beta}$, we also include all effects of device geometry on transmission and reflection between the spin selective terminals. This linear approximation is appropriate for our analysis, since within the small range of applied voltages of interest in operation of this device, the conductance can be treated as constant due to its very gradual variation with voltage.

The contact magnetization configuration (e.g. parallel or antiparallel, as described above) can be incorporated as a boundary condition in calculation of the transmission functions, yielding spin-dependent and magnetization-dependent conductance $G_{LC}^{\alpha\beta}$ and $G_{LR}^{\alpha\beta}$ in the model. The current then becomes a function only of the voltages applied to each terminal, with

$$I_L^{P(AP)} = G_{LC}^{P(AP)}(V_C - V_L) + G_{LR}^{P(AP)}(V_R - V_L) \, , \qquad (5.9)$$

where

$$G_{LC}^{P(AP)} = \sum_{\alpha,\beta} G_{LC}^{\alpha\beta} = G_{LC}^{\uparrow\uparrow} + G_{LC}^{\uparrow\downarrow} + G_{LC}^{\downarrow\uparrow} + G_{LC}^{\downarrow\downarrow}$$

and

$$G_{LR}^{P(AP)} = \sum_{\alpha,\beta} G_{LR}^{\alpha\beta} = G_{LR}^{\uparrow\uparrow} + G_{LR}^{\uparrow\downarrow} + G_{LR}^{\downarrow\uparrow} + G_{LR}^{\downarrow\downarrow}.$$

Without loss of generality, we can choose the voltage applied to the center terminal to be ground. The current extracted at the left terminal flowing from the central terminal and the current injected into the left terminal from the right terminal then become $G_{LC}^{P(AP)}V_L$ and $G_{LR}^{P(AP)}(V_R - V_L)$, respectively.

In a ballistic transport model, we may also assume that all transport channels are decoupled, i.e., $G_{ij}^{\alpha\beta}$ depends only on the electrical properties and magnetization configurations of terminal *i* and terminal *j*, and is independent of the third terminal. Thus, the three-terminal device reduces to two dual-terminal spin valves with one shared terminal. We also note that the left and right terminals may be separated by a distance beyond the quasi-ballistic regime because the distance between them is several times larger than the elastic scattering length, λ_e. However, it is still appropriate to describe the current between the left and right terminals by a simple linear expression, $G_{LR}^{P(AP)}(V_R - V_L)$, with a distance-dependent conductance $G_{LR}^{P(AP)}$ for the narrow voltage ranges of interest.[160]

Following the typical treatment for local spin valves, spin polarized electron transport from the left terminal to the central terminal can be represented by spin-dependent conductance $G_{LC}^{P(AP)}$ for the parallel or antiparallel magnetization configuration. The magnetoreistance is estimated as

$$MR = \frac{\Delta G_{LC}}{\overline{G}_{LC}} = \frac{2(G_{LC}^{P} - G_{LC}^{AP})}{G_{LC}^{P} + G_{LC}^{AP}} \approx \frac{\gamma^2/(1-\gamma^2)}{1+\tau_n/\tau_{sf}}, \tag{5.10}$$

where γ is the spin injection coefficient of the spin-selective contacts, τ_n and τ_{sf} are total 'transport time' through the spin valve and the spin scattering time, respectively. Further calculation[161] shows γ is

$$\gamma = \frac{J^+ - J^-}{J} = [\Delta r_c + r_F(\Delta\sigma/\sigma_F)]/[r_F + r_c + r_N^*], \tag{5.11}$$

where r_F, r_c and r_N are the characteristic resistances of the ferromagnetic, interface and semiconductor regions of the spin valve devices. The ratio of τ_n and τ_{sf} is given by

$$\tau_n/\tau_{sf} = t_N\lambda/\bar{t}_r L^2_{sf} \quad , \tag{5.12}$$

where $\bar{t}_r = h/2e^2(k_f W/\pi)r_C$.

In our devices, $r_F = \rho_F^* l_{sf}^F = 4.5\times10^{-15}\Omega\cdot m^2$, $r_N = \rho_N^* l_{sf}^N \approx 10^{-11}\Omega\cdot m^2$, $r_c \approx 10^{-11}\Omega\cdot m^2$. We note that r_c is of the same order as r_N^*, which indicates that current polarization within the InAs surface 2DEG channel will mainly depend on the spin asymmetry of the contact resistances, $\beta = \Delta r_c / r_c$. The spin asymmetry β lacks consistent theoretical description and reported experimental values vary substantially for different experiments.[137] Therefore, we use the values extracted from our own experiments to estimate γ while we follow the conventional conductance mismatch model and the ballistic transport model.

Employing a general treatment for spin polarized electron transport between the left and center terminals discussed above, the spin dependent magneto-resistance between adjacent terminals obeys the relation

$$\frac{\Delta G_{LC}}{\overline{G}_{LC}} = \frac{2(G_{LC}^{P} - G_{LC}^{AP})}{G_{LC}^{P} + G_{LC}^{AP}} \approx \gamma^2/(1-\gamma^2), \tag{5.13}$$

where γ is the interface spin-asymmetry coefficient and can be determined for our devices from two-terminal spin valve measurements.

For current transport between the left and right terminals, which we take to occur within the diffusive, rather than ballistic, transport regime, the spin polarization of current from the right terminal will decay exponentially, i.e., as $\exp(-l/L_{sf})$ for $l \geq L_{sf}$, where l is the path length for a specific electron trajectory from the right to left terminal and L_{sf} is the spin-flip scattering length. A reasonable estimate for this distance is the center-to-center distance between the left and right contacts, which for our devices is ~550nm. Thus, we see that the spin-dependent conductance between the left and right terminals obeys the relation[161]

$$\frac{\Delta G_{LR}}{\overline{G}_{LR}} \approx \gamma^2/(1-\gamma^2)\exp(-L_{LR}/L_{sf}). \tag{5.14}$$

To attain the maximum possible value of magnetoresistance, we assume in our analysis that the current at the left terminal in the antiparallel magnetization configuration is zero, i.e.,

$$I_L^{AP} = G_{LC}^{AP} V_L + G_{LR}^{AP} (V_L - V_R) = 0 \,. \tag{5.15}$$

The current at the left terminal in the parallel magnetization configuration is then

$$I_L^P = G_{LC}^P V_L + G_{LR}^P (V_L - V_R) \,, \tag{5.16}$$

from which we see that the change in current that occurs upon changing the contact magnetization from the parallel to antiparallel configuration is

$$\Delta I_L = \Delta G_{LC} V_L + \Delta G_{LR} (V_L - V_R) \,. \tag{5.17}$$

From Eqn. (5.14) we can easily deduce that

$$\Delta G_{LR} / \overline{G}_{LR} = (\Delta G_{LC} / \overline{G}_{LC}) \exp\{- L_{LR} / L_{sf}\} \,, \tag{5.18}$$

where we estimate L_{LR} to be the center-to-center distance between the left and right contacts. From Eqns. (5.14) to (5.18) we then see that

$$\Delta G_{LR} V_R = (\Delta G_{LR} / \overline{G}_{LR}) \overline{G}_{LR} V_R \approx (\Delta G_{LC} / \overline{G}_{LC}) \exp\{- L_{LR} / L_{sf}\} \cdot \overline{G}_{LC} V_C = \Delta G_{LC} V_C \exp\{- L_{LR} / L_{sf}\} \cdot \tag{5.19}$$

Therefore, the change in current at the left terminal that occurs upon changing the magnetization configuration from the parallel to the antiparallel configuration, $\Delta I_L \equiv I_L^P - I_L^{AP}$, is

$$\Delta I_L \approx \Delta G_{LC} V_{LC} (1 - \exp(-L_{LR} / L_{sf})) \tag{5.20a}$$

$$\approx \gamma^2 \overline{G}_{LC} V_{LC} (1 - \exp(-L_{LR} / L_{sf})) \,, \tag{5.20b}$$

where Eqn. (5.20b) holds for γ<<1.

5.4.4 Comparison of the spin diffusive analysis and the spin-polarized ballistic analysis

With the same values of L_{sf} and γ as Chapter 3 and Chapter 4, i.e., $L_{sf} = 380 \pm 130nm$ and $\gamma = 2 \pm 1\%$, substituting $L_{sf} = 300nm$ and $\gamma = 3\%$ in Eqn. (5.20) to estimate the expected change in current upon changing the contact magnetization state, we obtain $\Delta I_{\mathrm{L}} \approx 1\mu A$, in reasonable agreement with the observed value of $\sim 2\mu A$, as shown in Figure 4. This value of the interface spin-asymmetry coefficient γ is lower than the best reported spin injection coefficient for InAs[162, 163] and might be understood as a consequence of a dirty interface due to our ex-situ fabrication process. To match our measured results by the spin diffusive model in Section 5.4.2, the spin injection efficiency γ is required to be as high as 11%, which is much larger than our best experimental value, implying that the spin diffusion model does not provide a good description of the behavior observed in our device structures. This comparison between the ballistic and diffusive transport model shows the advantage of the ballistic model in predicting the change of current at the left terminal, ΔI_L, which is the key device performance parameter monitored in our experiments.

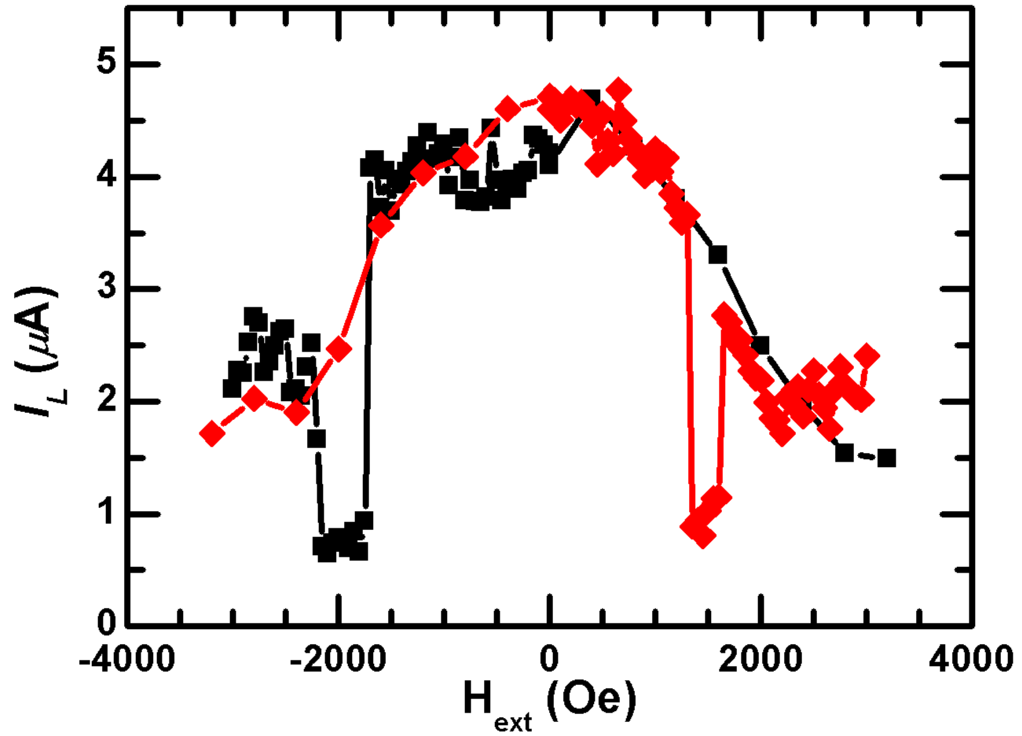

Figure 5.5: Current flow I_L as a function of external applied magnetic field, for field sweep directions – to + (red diamonds) and + to – (black squares). A clear shift in current for antiparallel magnetization configurations (↓↑↑ at ~+1500Oe and ↑↓↓ at ~-2000Oe) is evident. Adjustment of voltages V_L and V_R allows the current in the antiparallel configuration to approach zero (to within the noise floor of the device), leading to a large on/off current switching ratio.

In addition, the ballistic transport model also predicts correctly the relationship between the change of current at the left terminal, ΔI_L and the relative value of the applied voltage at the left terminal, V_{LC}. From Eqn. (5.20), based on the ballistic transport model, we see that ΔI_L is directly proportional to V_{LC}. In case that V_{LC} is increased by several percents, ΔI_L would also be increased only by several percents, while the current at the left terminal in the antiparallel configuration, I_L^{AP} might be increased from near zero to a finite value. Therefore, the magnetoresistance, defined as $\Delta I_L / I_L^{AP}$ would drop dramatically with the deviation of V_{LC} from its initial value, which balanced out the current at the left terminal orignially, as shown in Figure 5.6. In contrast, from Eqn. (5.6), based on the spin diffusion transport model, ΔI_L is directly proportional to the initial current and will be quenched to zero with the reduced initial current, which contradicts our observation. The agreement between the prediction from the ballistic transport model and the observed device performance and the contradiction between the prediction from the diffusion transport model and the observations confirm the ballistic nature of electron transport in our devices.

To exclude the possibility of local Hall effect (LHE)[164] in our devices, a set of hybrid Hall devices with Cobalt contacts on top of InAs surface electron layers were fabricated. MFM measurements show the stray field of a rectangular magnetic contact is normally intensified at the ends of the long axis, as shown in Figure 5.3. For this reason, we locate the edge of the magnetic contacts in the middle of the electron

transport channels to enlarge the local Hall effect signals due to the perpendicular components of the stray fields from the magnetic contacts. In our measurements, no magnetization-dependent signals were detected in this set of devices. We therefore conclude that in our multi-terminal spin transistors, the perpendicular components of the stray fields from the magnetic contacts will not contribute on the electron transport behaviors observed in our magnetoresistance measurements.

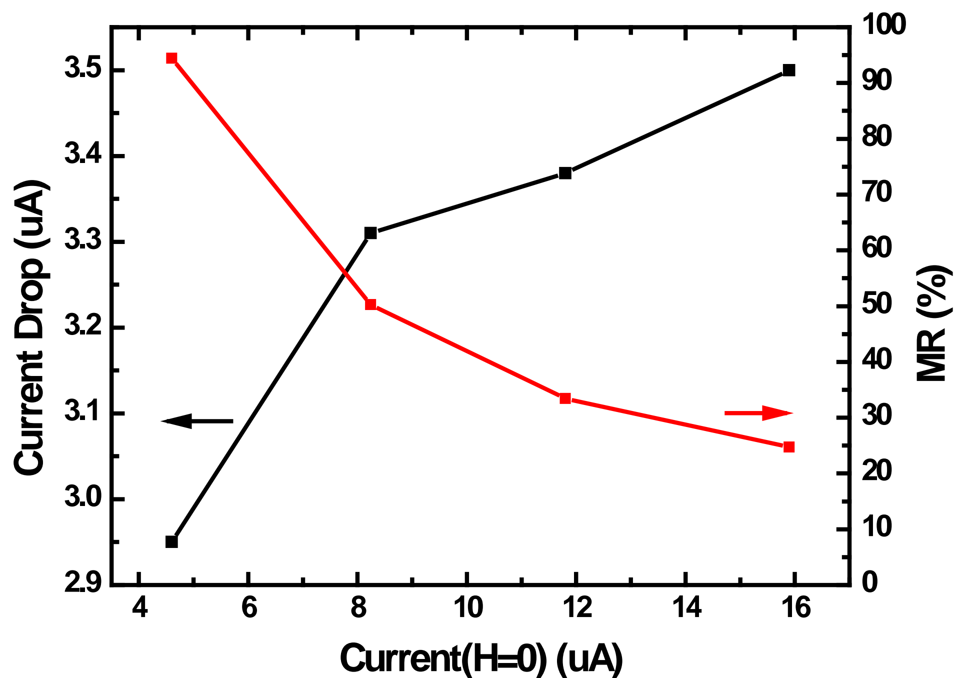

Figure 5.6: Abrupt current dip increased slowly with initial current without external magnetic field applied; correspondingly, MR will decrease dramatically.

In our measurements, spin precession is another possible source for parasitic signals. For the InAs surface electron layers, the dominant spin-orbit interaction mechanism is 'structure inversion asymmetry' (SIA), giving rise to the Rashba term in the Hamiltonian, $H_R = -\frac{i}{2}[\alpha\sigma \times \nabla] \cdot \hat{v}$.[165] As the spin polarization of surface electrons is defined along the magnetization direction of the magnetic contacts, and thus perpendicular to the electron transport direction, both spin up and spin down states are treated as the eigenstates of the modified Hamiltonian equation with the Rashba term.[166] The phase difference from spin procession is then suppressed to zero. During our measurements, the external magnetic fields are applied parallel to the spin polarization direction, obviating the electron spin precession along the polarized axis. Since the magnetic fields may not be perfectly aligned with the spin polarization direction, their off-plane components may cause in-plane spin precession at the Larmor frequency $\Omega = g\mu_B B/\hbar$, where g is the electron g-factor of InAs, μ_B is the Bohr magneton and $\hbar$ is the reduced Planck's constant. In the range of our applied magnetic fields, even for an extraordinarily misaligned case, for instance, a misalignment with 20 degree angle between the magnetic fields and the spin polarization, the off-plane components of the magnetic fields are only able to introduce a precession less than 10 degree. Therefore, the total spin precession from both the internal crystal structure of InAs and the external magnetic fields will be small in our devices. When the external magnetic fields are applied fully perpendicular to the InAs surface, the spin precession is still not observable in our spin transistor devices, due to the short channel lengths and fast spin decoherence inside these

devices. In our spin transistor devices, an out-of-plane magnetic field beyond 1 T would be required to induce spin precession through an angle π over a channel length of ~ 100 nm. Such a strong magnetic field would saturate the magnetization of the Cobalt contacts in the out-of-plane direction, [167] eliminating the in-plane spin polarization within the InAs channels upon with device operation is based. One should also note that the rapid spin decoherence will suppress spin precession.[168] Therefore, the magnetoresistance oscillation,[169] which is typically regarded as the most definitive of proof for spin precession and used to extract the information on spin diffusion inside semiconductor channels, is very unlikely to be observed in our devices even with strong magnetic fields.

5.5 Conclusions

We demonstrate a robust, electrically amplified spin-dependent current signal in a three-terminal, all-electrical spintronic switching device, despite modest efficiency in electrical injection of spin-polarized electrons. A spin-polarized ballistic analysis, rather than spin diffusive analysis is used to explain the magnetoresistance amplification in this device. The ballistic analysis combines charge current cancellation by appropriate device biasing as well as a ballistic picture of electron transport. The amplification scheme provides insight into the advantages of spin-dependent ballistic transport in device operation and scaling-down capability, which may inspire designs and demonstrations of novel ballistic spintronic devices.

Acknowledgments: This chapter, in full, will be submitted for publication of the material as it may appear in the Nature Physics, 2009. Zhu, Lei; Yu, Edward T., **"**Ballistic transport and electrical spin signal amplification in a three-terminal spintronic device**",** Nature Publishing Group, 2009. The dissertation author was the primary investigator and author of this paper.

Reference

[137] I. Zuitc, J. Fabian, and S. D. Sarma, *Rev. Mod. Phys.* **76**, 323 (2004).

[138] *Semiconductor Spintronics and Quantum Computation*, edited by D. D. Awschalom, D. Loss, and N. Samarth (Springer, Berlin, 2002).

[139] D. D. Awschalom and F. M. Flatté, *Nat. Phys.* **3**, 153 (2007).

[140] S.-W. Jung and H.-W. Lee, *Phys. Rev. B* **73**, 165302 (2006).

[141] J. Wang and H. Lee, *Phys, Rev. B* **73**, 165302 (2006).

[142] Y. Acremann, X. W. Yu, A. A. Tulapurkar, A. Scherz, V. Chembrolu, J. A. Katine, M. J. Carey, H. C. Siegmann, and J. Stöhr, *Appl. Phys. Lett.* **93**, 102513 (2008).

[143] A. Scherz, C. Sorg, M. Bernien, N. Ponpandian, K. Baberschke, H. Wende, and P. J. Jensen, *Phys. Rev. B* **72**, 054447 (2005).

[144] H. Dery, L. Cywinski, and L. J. Sham, *Phys. Rev. B* **73**, 161307 (2006).

[145] D. Saha, M. Holub, P. Bhattacharya, *Appl. Phys. Lett.* **91**, 072513 (2007).

[146] L. Ö. Olsson, C. B. M. Andersson, M. C. Håkansson, J. Kanski, L. Ilver, and U. O. Karlsson, *Phys. Rev. Lett.* **76**, 3626 (1996).

[147] G. Meier, T. Matsuyama, and U. Merkt, *Phys. Rev. B* **65**, 125327 (2002).

[148] T. Matsuyama, C.-M. Hu, D. Grundler, G. Meier, and U. Merkt, *Phys. Rev. B* **65**, 155322 (2002).

[149] P. R. Hammar, B. R. Bennett, M. J. Yang, and M. Johnson, *Phys. Rev. Lett.* **83**, 203 (1999).

[150] X. Lou, C. Adelmann, M. Furis, S. A. Crooker, C. J. Palmstrøm, and P. A. Crowell, *Phys. Rev. Lett.* **96**, 176603 (2006).

[151] C. Ciuti, J. P. McGuire, and L. J. Sham, *Phys. Rev. Lett.* **89**, 156601 (2002).

[152] H. Dery, P. Dalal, L. Cywinski, and L. J. Sham, *Nature* **447**, 573 (2007).

[153] J. P. Lazzari, I. Melnick, and D. Randet, *IEEE Trans. Magn.* **3**, 205 (1967).

[154] Y. Kawaguchi, I. Takayanagi, and S. Kawaji, *J. Phys. Soc. Jpn.* **56**, 1293 (1987).

[155] F. J. Jedema, M. S. Nijboer, A. T. Filip, B. J. van Wees, *Phys. Rev. B* **67**, 085319 (2003).

[156] H. Dery, L. Cywinski and L. J. Sham, *Phys. Rev. B* **73**, 041306 (2006).

[157] T. Valet and A. Fert, Phys. Rev. B 48, 7099 (1993).

[158] S. Datta, *Electronic Transport in Mesoscopic Systems* (Cambridge University Press, Cambridge, 1995).

[159] H. X. Tang, F. G. Monzon, R. Lifshitz, M. C. Cross, and M. L. Roukes, *Phys. Rev. B* **61**, 4437 (2000).

[160] A. S. Sedra and K. C. Smith, *Microelectronic Circuits* (Oxford University Press, Oxford, 1998)

[161] A. Fert, J.-M. George, H. Jaffres, R. Mattana, *IEEE trans. Electron Device* **54**, 921 (2007).

[162] Ohno H. K. Yoh, K. Sueoka, K. Mukasa, A. Kawaharazuka, and M. E. Ramsteiner, *Jpn. J. Appl. Phys.* **42**, 87-89 (2003).

[163] A. V. Stier, C. J. Meining, B. D. McCombe, I. Chado, P. Grabs, G. Schmidt, and L. W. Molenkamp, *Appl. Phys. Lett* **93**, 081112 (2008).

[164] F. G. Monzon, M. Johnson and M. L. Roukes, *Appl. Phys. Lett.* **71**, 3087 (1997).

[165] S. Lamari, *Phys. Rev. B* **64**, 245340 (2001).

[166] T. Matsuyama, R. Kürsten, C. Meißner, and U. Merkt, *Phys. Rev. B* **61**, 15588 (2000).

[167] J. M. Alameda, M. C. Contreras, F. Carmona and, F. Lopez, *phys. Stat. sol. (a)* **107**, 329 (1988).

[168] X. Lou, C. Adelmann, S. A. Crooker, E. S. Garlid, J. Zhang, K. S. M. Reddy, S. D. Flexner, C. J. Palmstrøm, and P. A. Crowell, *Nature Physics* **3**, 197 (2007).

[169] I. Appelbaum, B. Huang, and D. J. Monsma, Nature 447 (2007).

Chapter 6

Geometry influence on spin diffusion and reexamination of spin injection model in a metallic spin valve

6.1 Spin injection and diffusion in mesoscopic spintronic devices

Spin-dependent transport in ferromagnet/semiconductor and ferromagnet/ paramagnet hybrid nanostructures has attracted great attention due to their potentials to create new functionality in electronic devices.[170] Efficient spin injection and long spin relaxation length are essential to realize spin-dependent electronic devices.[171] In addition to these two technological prerequisites, the geometry of spin-dependent

devices also plays an important role to in optimization and understanding of device performance.[172]

We choose the all-metallic spin valve as the candidate to examine the influence of the device geometry on device performance and address fundamental issues in spin diffusion in the nonmagnetic channel. Although a variety of successful experiments focused on semiconductor-based spintronic devices have been reported,[173,174,175] consistently efficient spin injection from magnetic materials into semiconductors is still a challenge. Therefore, it is of considerable interest in spin injection and transport to distinguish the geometry effects from other effects. Spin injection in all-metallic devices is predicted to be achieved easily due to the much smaller conductance mismatch between the magnetic terminals and nonmagnetic channel compared with between the ferromagnetic contact and semiconductor channel.[176] The sophisticated fabrication technologies, such as well-developed metal deposition, and controllable interface resistance also contribute to the successful demonstrations of all-metallic spintronic devices with consistently spin injection efficiency and spin diffusion length. We also note that, unlike semiconductor channels, paramagnetic channels hold the same spin relaxation times for both the transverse and longitudinal spin diffusions, which accentuate the geometry effects from device design instead of spin relaxation mechanisms.

In the last decade, lateral spin valves based on ferromagnetic/nonmagnetic metallic wires were emerging as tools for the study of intrinsic properties of paramagnets. Both local and nonlocal spin valve geometries have been extensively

studied and used to extract information on spin injection efficiency across the interface and spin diffusion length in the nonmagnetic metal.[177,178] Recently, Kimura, Otani and Hamrle have experimentally demonstrated that the reduction of the junction size in a Py/Cu lateral spin valve drastically improved the spin injection efficiency into the Cu channel.[179] Godfrey and Johnson[180] have reported an abnormally large spin polarization of current injected from a Permalloy electrode into an Ag nanowire measured in nonlocal spin valve geometry. These measurements reveal the limitation of the one dimensional spin diffusion model for a realistic nonlocal spin valve,[181] which oversimplifies the three dimensional geometry of a spin valve, and thus, ignores the possibility of the performance enhancement by modifying the conventional geometry.

6.2 Numerical simulation of spin injection and diffusion in mesoscopic spintronic devices by finite element method

For the irregular boundary condition characteristic of realistic device geometries, the coupled spin-splitting chemical potential equations, which use Valet-Fert theory[182] to describe steady-state spin diffusion, lack analytical solutions and numerical simulations are needed. Therefore, to facilitate numerical calculation, we adopt the finite element method solver in the commercial Comsol FEMlab software package to solve the partial differential equation system describing intermixing diffusion of spin up and spin down channels. The simulation uses dimensions and

material properties relevant to Godfrey and Johnson's experiment.[180] For efficient simulations, we assume the uniformity of devices along the direction of the magnetic contacts and solve the spin diffusion equations in the two dimensional cross section, to which the interface of the magnetic electrodes and nonmagnetic channel is perpendicular. This simplification will not influence the relation between the spin valve transresistance and the thickness of the nonmagnetic channels, as summarized in the following subsections.

6.2.1 Numerical simulation of spin injection and diffusion in a metallic spin valve by finite element method

The basic device geometry simulated is shown in Figure 6.1, the widths of the Py contacts are 100 nm and 200 nm, with a 200 nm edge-to-edge separation. The resistivity of the Ag nanowires ρ_{Ag} and Py contacts ρ_{Py} are 3.8 μΩ cm and 23.6 μΩ cm, respectively.[180] The spin diffusion length δ_{sf} and spin polarization p_f of Py contacts are chosen from commonly accepted values, i.e., δ_{sf} = 4.3 nm[183] and p_f = 0.37.[184] The overall area of the two-dimensional simulation is 5 μm × 5 μm, much larger than the device geometry, which excludes the possible influence from the limited simulation area. The thickness of Ag nanowires varies from 65 nm to beyond the 200 nm spin diffusion length of the deposited Ag film.[180] The simulation is based on the local spin valve geometry, i.e., the charge current is injected at the left Py/Ag interface and withdrawn at the right Py/Ag interface. The boundary conditions are continuity of the

chemical potentials and spin polarization through the interface, obeying Valet-Fert theory. The details of boundary conditions and device dimensions are summarized in Table 6.1, where x_{f1}, x_{f2} are the central positions of the left ferromagnetic terminal and the right ferromagnetic terminal, respectively, and d_{f1}, d_{f2}, d_n and the widths of the left ferromagnetic terminal, the right ferromagnetic, and the nonmagnetic channel, respectively.

Table 6.1: Boundary conditions for the numerical simulations presented in Figure 6.1

Boundary condition	Interface range
$\mu_s(y=0+) = \mu_s(y=0-)$	$x_{f1}-d_{f1}/2 \le x \le x_{f1}+d_{f1}/2$; $x_{f2}-d_{f2}/2 \le x \le x_{f2}+d_{f2}/2$
$\partial_y \mu_s(y=0+) = \partial_y \mu_s(y=0-)$	$x_{f1}-d_{f1}/2 \le x \le x_{f1}+d_{f1}/2$; $x_{f2}-d_{f2}/2 \le x \le x_{f2}+d_{f2}/2$
$\partial_y \mu_s(y=-y_n) = 0$	$-d_n/2 \le x \le +d_n/2$
$\partial_x \mu_s(x=-d_n/2) = \partial_x \mu_s(x=+d_n/2) = 0$	$-y_n \le x \le 0$

The difference of spin splitting chemical potentials ($\mu_+ - \mu_-$) in a lateral spin valve is shown in Figure 6.1. The spin accumulation appears in the antiparallel magnetization configuration of two Py contacts, as shown in Figure 6.1(a), and the chemical potential splitting ($\mu_+ - \mu_-$) changes its sign in the parallel magnetization configuration, as shown in Figure 6.1(b). Figure 6.2 compares the simulation results of the Py/Ag/Py spin valve with 500 nm thick Ag channel and the spin valve with 65 nm thick Ag channel in the parallel magnetization configuration. Both spin splitting plots follow the same material properties and device geometry, except for the different

thickness of the Ag channels. Figure 6.2 shows that the confinement of spin polarization decay in the vertical direction can prolong the spin polarization decay length along the lateral direction. The results for the anti-parallel magnetization configuration are summarized in Figure 6.3, in which the thickness of the Ag channels is 500 nm and 65 nm. The reduced thickness of the Ag channels will also prolong the lateral spin decay in the antiparallel magnetization configuration.

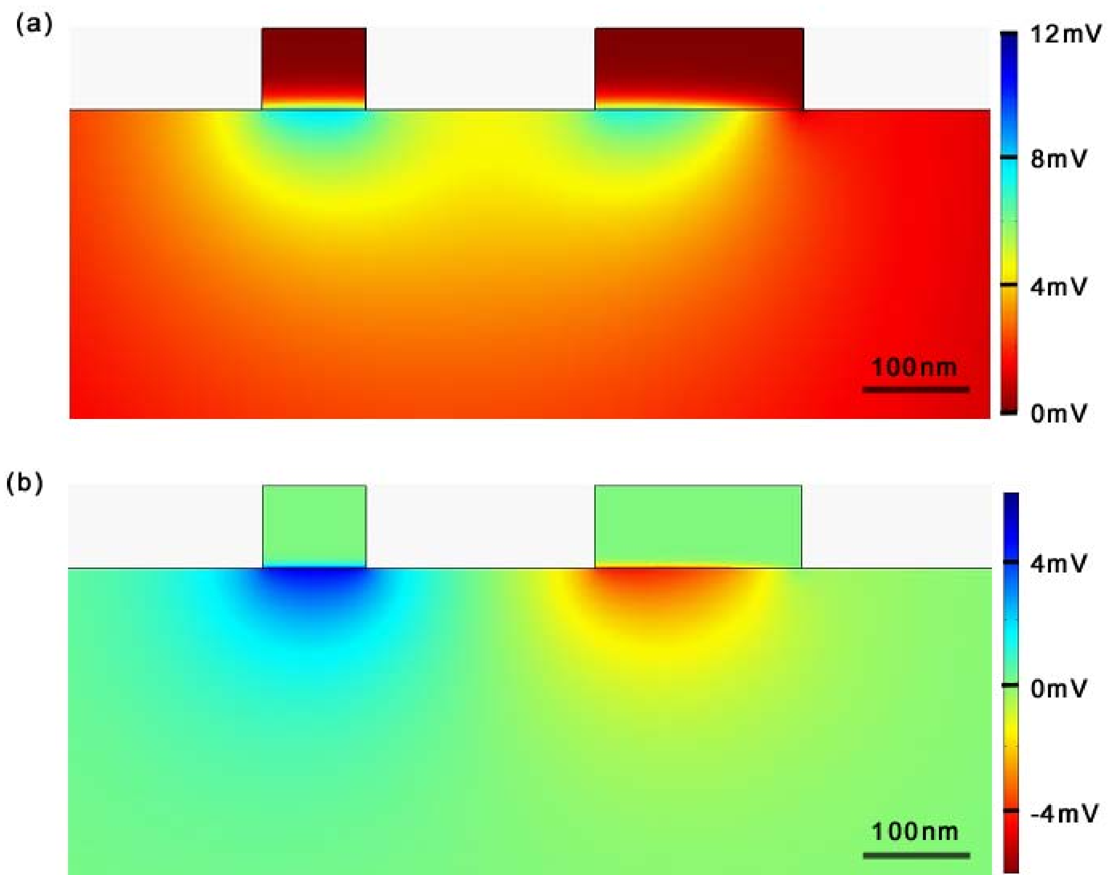

Figure 6.1: Chemical potential splitting ($\mu_+ - \mu_-$) in local spin valve geometry (a) in the antiparallel magnetization configuration (b) in the parallel magnetization configuration.

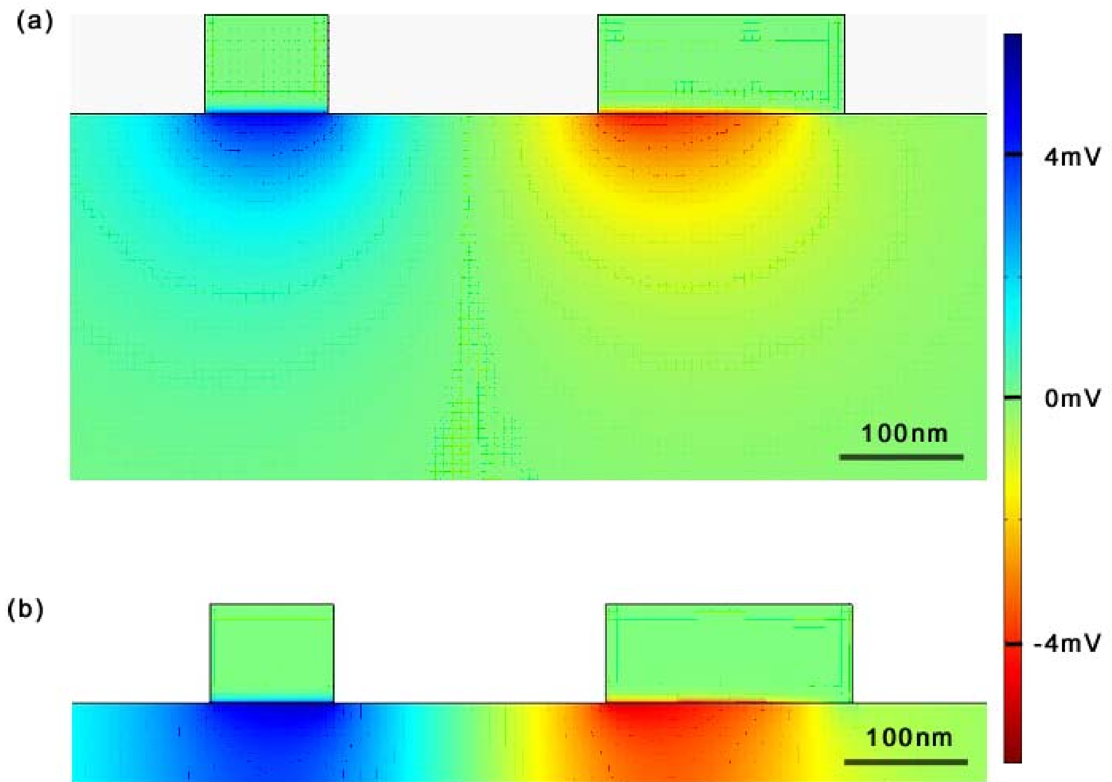

Figure 6.2: Chemical potential splitting (μ_+ - μ_-) in the parallel magnetization configuration (a) in a 500-nm-thick channel spin valve, and (b) in a 65-nm-thick channel spin valve.

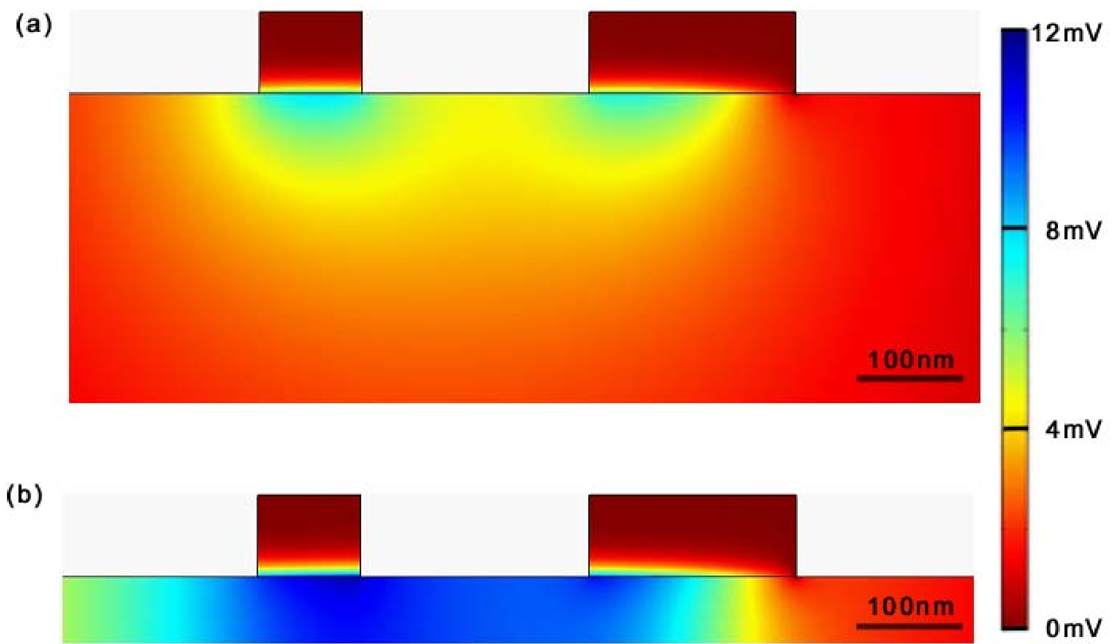

Figure 6.3: Chemical potential splitting (μ_+ - μ_-) in the antiparallel magnetization configuration (a) in a 500-nm-thick channel spin valve, and (b) in a 65-nm-thick channel spin valve.

6.2.2 Comparison of numerical simulation results of spin splitting in a thin-channel spin valve and cross section images of spin polarization in an n-GaAs spin valve

Similar effects were observed in the n-GaAs channels for which the spin diffusion length was much smaller than the device extent in the vertical direction.[185] In this Kerr microscope measurement, where the signal is directly proportional to asymmetry of concentration of spin up/down channels, the objective lens are scanned across the x-y plan, which is a (110) surface produced by cleaving the wafer across the metallic contacts. The color scale of cross-sectional imaging of the injected spin polarization in the lateral-current geometry gradually changes along the charge current transport direction, as shown in Figure 6.4(a). Comparing a simulation based on metallic lateral spin valves with the cross-sectional imaging of spin diffusion in GaAs channels, it stands to reason that the similar lateral spin polarization decay behaviors in both images are due to the small channel thickness in comparison with the spin diffusion lengths in both nonmagnetic channels.

This result shows the complexity of spin diffusion in semiconductor spintronic devices. A typical ferromagnet/semiconductor hybrid device normally uses multi-player semiconductor heterostructures grown by molecular beam epitaxy. The thickness of the nonmagnetic channel plays an important role on modulating the decay of spin polarization. The comparison above may also help us to understand the

inconsistency between the spin injection efficiency through optical stimulation and the efficiency by all electrical injection.

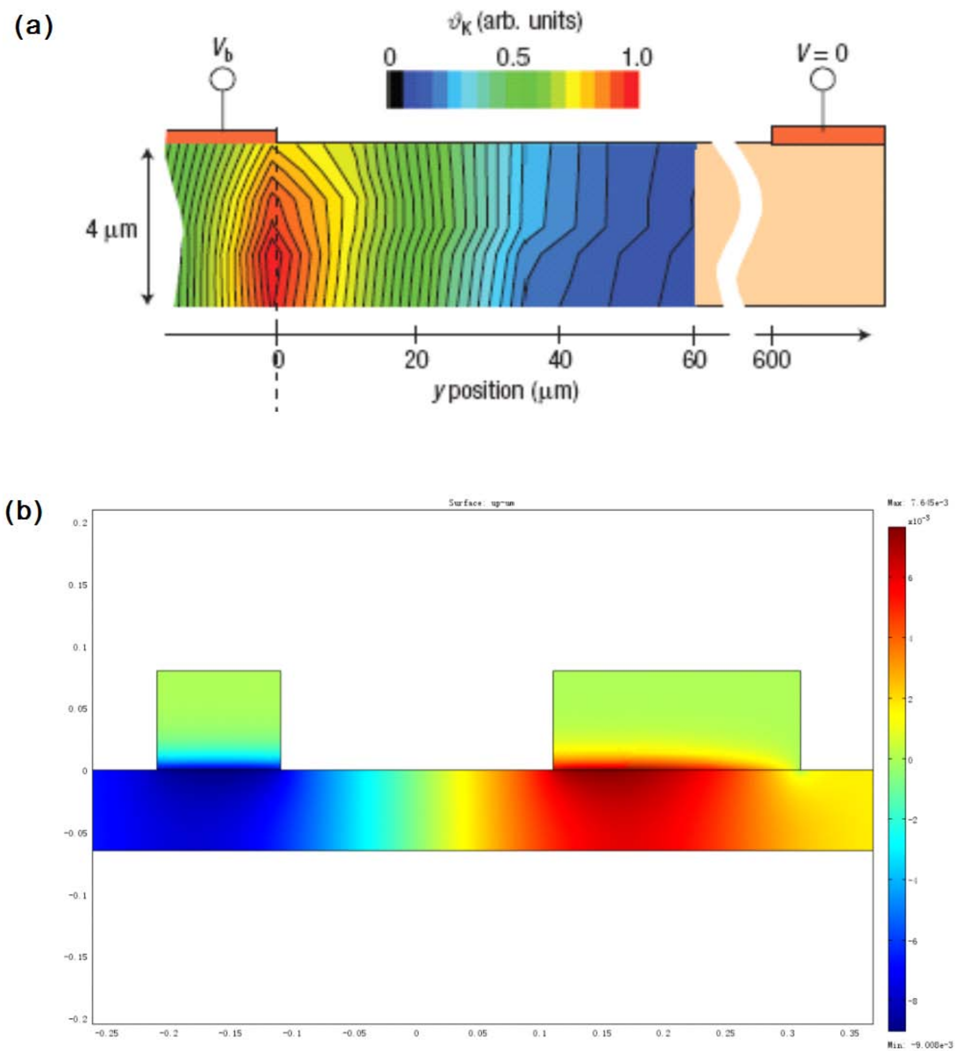

Figure 6.4: (a) Kerr microscope image of spin polarization in n-GaAs channel (after P. Kotissek, et al, *Nat. Phys.* **3**, 872 (2007).). (b) Simulation results of chemical potential splitting ($\mu_+ - \mu_-$) in a shallow-channel metallic spin valve.

6.2.3 Reexamination of one dimensional spin valve model

Applying the conductance mismatch model for the Py/Ag interface in Py/Ag/Py spin valves, the injection efficiency is expected to be 5%. In our two dimensional finite element method simulation, the magnetoresistance is calculated by comparing the chemical potential splitting between the injection terminal and the extraction terminal with an enforced current in the parallel magnetization configuration and the splitting in the antiparallel magnetization configuration. The resistance difference between the parallel and antiparallel configurations, based on one dimensional spin diffusion analytical model for a local spin valve geometry,[186, 187] can be expressed as

$$\Delta R_s = \frac{P_1 P_2 \rho L_N}{A} e^{-L/L_N} \quad . \tag{6.1}$$

Fitting the simulated results to Eqn. (6.1), the nominal spin injection efficiency increases from 5% to 12.5% with decreasing thickness of the Ag channel, as shown in Figure 6.5 This explains the contradiction between the fitted spin injection efficiency from the measured magnetoresistance in Godfrey and Johnson's experiments[180] and the expected spin injection efficiency based on conductance mismatch models.

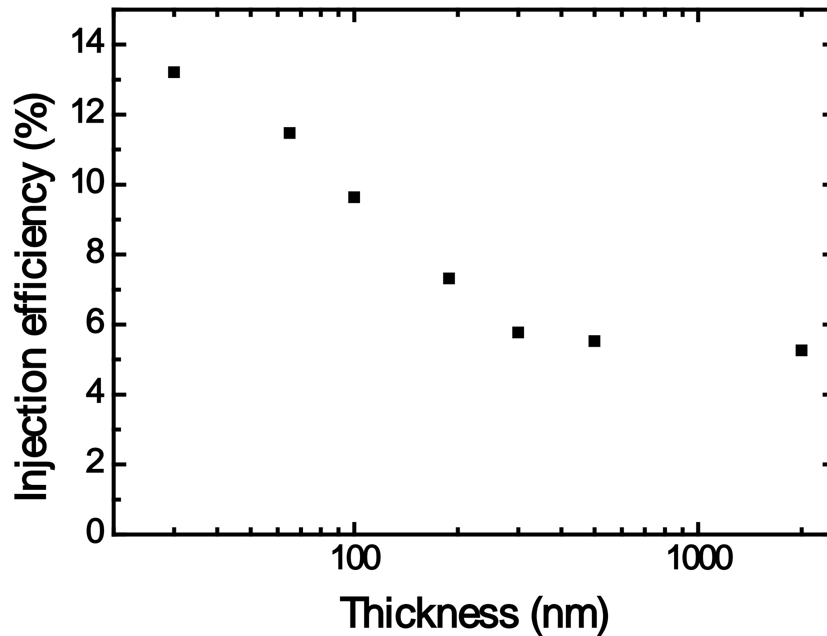

Figure 6.5: Fitted spin injection efficiency as a function of Ag channel thickness, based on one dimensional spin diffusion model.

6.3 Semi-analytical method for evaluation of spin diffusion in mesoscopic spintronic devices

In two-dimensional spin valve geometry, it fails to achieve analytical solutions due to the complexity of irregular boundary conditions. This problem can be circumvented by decomposing the two-dimensional geometry into a coupled multi-layer stack, with each layer obeying a one-dimensional analytical solution, as proposed by Dery, Cywiński, and Sham.[188] In the metallic spin valve explored, the

paramagnetic channel is sliced into several thinner layers with the same thickness with the same continuity boundary conditions at the magnetic/nonmagnetic interfaces used in the former finite element method simulation.

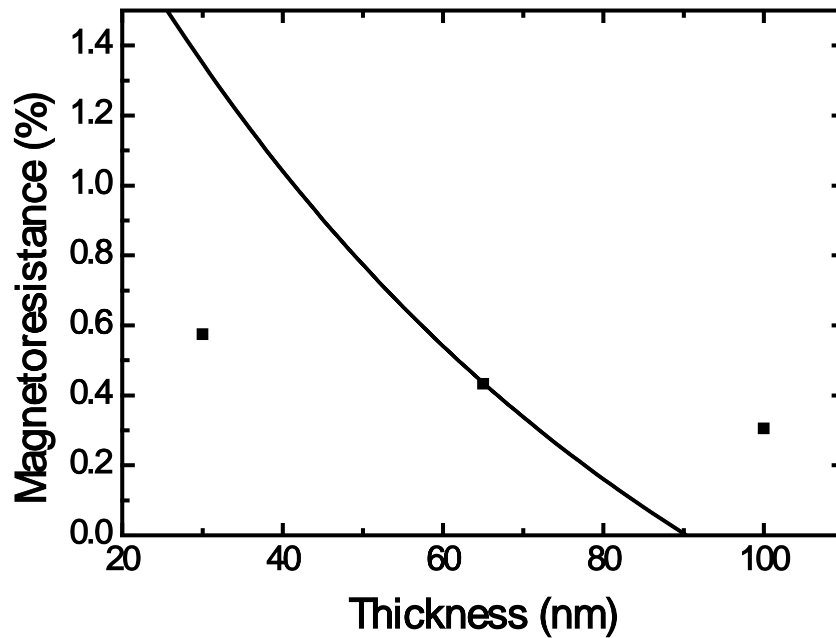

Figure 6.6: Magnetoresistance as a function of channel thickness in a lateral spin valve. The square dots and the solid curve represent the estimate from the 2D numerical simulation and the calculation by the multi-layer semi-analytical model, respectively.

A general solution for each layer is

$$\mu_{\pm}(x) = (e/\sigma_N)Jx + \mu \pm (p_c e^{x/L_N} + q_c e^{-x/L_N}) . \tag{6.2}$$

In the most simplified case, in which the channel is sliced into two identical layers, the solution for each layer contains mixed modes, implying the existence of both a leakage current into the nearby layer and a spin relaxation current into the opposite spin channel. The analytical solution contains more modes for a multi-layer case. The estimate by this model reveals the reduced magnetoresistance with the increasing channel thickness in a certain range, as shown in Figure 6.6.

6.4 Experimental examination of spin injection and diffusion in metallic mesoscopic spin valves

To confirm this physical picture and our simulation results, we fabricated several sets of Py/Al/Py lateral spin valves by standard e-beam lithography. For each set of spin valves, the spin diffusion length and spin polarization of the injected current are determined by measuring devices with the varying separation between two Py electrodes. Large electric contact pads, made of 16 nm Ti and 100 nm Au, are first deposited on top of silicon dioxide substrates. Two 35-nm-thick Py contacts with different widths are placed with the separation ranging from 100 nm to 300 nm. Finally, the quasi-one-dimensional Al nanowires are patterned perpendicular to the Py contacts, with a base vacuum $< 1 \times 10^{-7}$ Torr inside the deposition chamber during

process. For a different set of spin valves, the lateral geometry of the spin valves is kept the same, while the thickness of the Al nanowires varies.

To exclude spurious effects, such as tunneling magnetoresistance effects, the interface between the Py electrodes and Al nanowires is cleaned by low voltage Ar-ion milling prior to the Al deposition to guarantee an Ohmic contact. Spin valves based on Al nanowires are chosen in our experiments since the large spin-dependent signals and appropriate spin diffusion lengths compared with the deposition thickness of Al film in practical devices have been reported in Al-based spin valves in prior works.[187, 189, 190] Permalloy is chosen as the contact material due to its low contact resistance with most paramagnetic materials after simple RF surface cleaning and its easy magnetization, which help avoid spurious effects associated with high magnetic field measurements. Figure 6.7 show the typical devices with an Al nanowire and Py contacts in our experiments.

To investigate the low resistance metallic spin valves, the magnetoresistance measurements are taken at 77 K by means of standard lock-in techniques. The difference of magnetoresistance for spin valves with the different channel thickness is measured and summarized in Table 6.2. Overall, the nominal 'spin injection efficiency' from measurements show similar thickness dependent behavior as we expected in Section 6.2 and 6.3, i.e., it increases with decreasing thickness of the Ag channel. A large background noise, which causes ±2-3% absolute error, is observed. Therefore, the spin injection efficiency for a 90 nm-thick spin valve fails to be extracted due to the poor signal error rate. The difference between the experiments and the simulation

estimate may be caused by the nonideal interface, which introduces contact resistance in realistic devices.

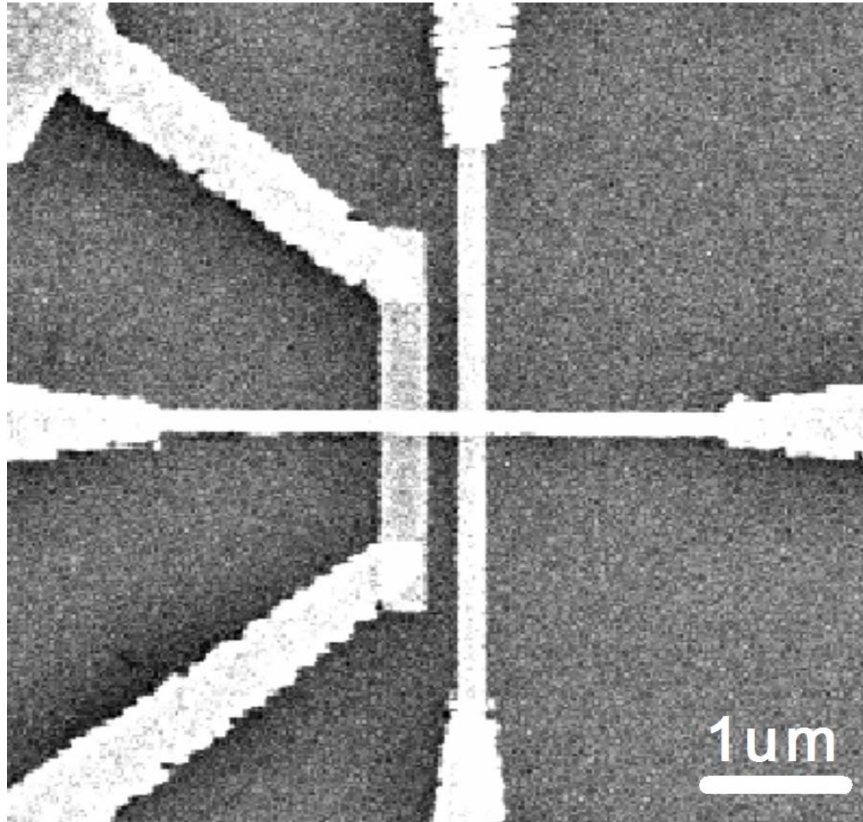

Figure 6.7: Scanning electron microscope (SEM) image of a spin valve composed of two Py contacts and Al channel.

Table 6.2: Estimated spin injection efficiency in Py/Al/Py spin valves with different channel thickness

Deposition thickness (nm)	Spin injection efficiency (%)
35	10±3
65	6±2
90	<2

6.5 Conclusions

In this chapter, we demonstrate and analyze the influence of the device geometry on magnetoresistance of nanoscale spin valve structures. Shortcomings of the simplified one-dimensional spin diffusion model for spin valve are elucidated, with comparison of the thickness and the spin diffusion length in the nonmagnetic channel as the criterion for validity of the 1D model. This dependence of spin transport and injection efficiency on channel depth offers a new opportunity to engineer the behavior of spintronic device at the nanoscale.

Acknowledgments: This chapter, in full, will be submitted for publication of the material as it may appear in the Applied Physics Letter, 2009. Zhu, Lei; Yu, Edward T., “Geometry influence on spin diffusion and reexamination of spin injection

model in a metallic spin valve", AIP Publishing, 2009. The dissertation author was the primary investigator and author of this paper.

Reference

[170] Magnetoelectronics, edited by M. Johnson (Elsevier, Oxford, 2004).

[171] S. A. Wolf, D. D. Awschalom, R. A. Buhrman, J. M. Daughton, S. von Molnár, M. L. Roukes, A. Y. Chtchelkanova, D. M. Treger, Science 294, 1488 (2001).

[172] H. Dery, L. Cywinski and L. J. Sham, *Phys. Rev. B* **73**, 041306 (2006).

[173] X. Lou . C. Adelmann, M. Furis, S. A. Crooker, C. J. Palmstrøm, and P. A. Crowell, *Phys. Rev. Lett.* **96**, 176603 (2006).

[174] B. C. Min, J. C. Lodder, R. Jansen, and K. Motohashi, *J. Appl. Phys.* **99**, 08S701 (2006).

[175] B. T. Jonker, G. Kioseoglou, A. T. Hanbicki, C. H. Li and P. E. Thompson, *Nat. Phys.* **3**, 542 (2007).

[176] G. Schmidt, D. Ferrand, L. W. Molenkamp, A. T. Filip and B. J. van Wees, *Phys. Rev. B* **62**, R4790 (2000).

[177] F. J. Jedema, A. T. Filip, and B. J. van Wees, *Nature* **410**, 345 (2001).

[178] Y. Ji, A. Hoffmann, J. E. Pearson, and S. D. Bader, *Appl. Phys. Lett.* **88**, 052509 (2006).

[179] T. Kimura, Y. Otani, and J. Hamrle, *Phys. Rev. B* **73**, 132405 (2006).

[180] R. Godfrey and M. Johnson, *Phys. Rev. Lett.* **96**, 136601 (2006).

[181] M. Johnson, *J. Appl. Phys.* **75**, 6714 (1994).

[182] T. Valet and A. Fert, *Phys. Rev. B* **48**, 7099 (1993).

[183] S. Dubois, L. Piraux, J. M. George, K. Ounadjela, J. L.Duvail, and A. Fert, *Phys. Rev. B* **60**, 477 (1999).

[184] R. J. Soulen Jr., J. M. Byers, M. S. Osofsky, B. Nadgorny, T. Ambrose, S. F. Cheng, P. R. Broussard, C. T. Tanaka, J. Nowak, J. S. Moodera, A. Barry, and J. M. D. Coey, *Science* **282**, 85 (1998).

[185] P. Kotissek, M. Bailleul, M. Sperl1, A. Spitzer, D. Schuh, W. Wegscheider, C. H. Back and G. Bayreuther, *Nat. Phys.* **3**, 872 (2007).

---

[186] M. Johnson, and J. Byers, *Phys. Rev. B* **67**,125112 (2003).

[187] F. J. Jedema, H. B. Heersche, A. T. Filip, J. J. A. Baselmans, and B. J. van Wees, *Nature* **416**, 713 (2002).

[188] H. Dery, Ł. Cywiński, and L. J. Sham, *Phys. Rev. B* **73**, 041306(R) (2006).

[189] N. Poli, M. Urech, V. Korenivski, and D. B. Haviland, *J. Appl. Phys.* **99**, 08H701 (2006).

[190] M. V. Costache, M. Zaffalon, and B. J. van Wees, *Phys. Rev. B* **74**, 012412 (2006).